Scuola Internazionale Superiore di Studi Avanzati

PhD course in Theory and Numerical Simulation
of Condensed Matter

Cluster mean-field dynamics of the long-range interacting Ising chain

A thesis submitted for the degree of *Doctor Philosophiæ*

Candidate
Giulia Piccitto

Supervisor
Prof. Alessandro Silva

September 2020

“Piccitto, lo spin è importante”

Marco Ruggieri

Contents

1

Introduction

The problem of nonequilibrium dynamics in classical systems has been widely addressed since the seminal work by Boltzmann that in 1872 proved the H-theorem [1–3]. The theorem claims that nonequilibrium classical gases, under the assumption of "molecular chaos", thermalize, i.e. equilibrate to the maximum entropy configuration ensuring the energy conservation. It was not clear how to reconcile the macroscopic irreversibility and the reversibility of the microscopic dynamics. In fact, empirically it had always been observed an evolution from some "atypical" nonequilibrium configurations to "typical" ones described by the statistical ensembles. In agreement with the second law of thermodynamics, the world, regardless of to the microscopic reversibility, follows a well defined time direction that privileges entropy-increasing processes, although entropy-decreasing ones are allowed by the Newton's law. This is because thermalization has to be understood as a typical behavior: the equilibrium state is simply the most probable. Observing a nonequilibrium system for a time T, the probability of a state is defined as $\lim_{T\to\infty} \tau/T$, with τ the time the system spends in that state. The probability is strictly connected to the volume occupied by the macrostate in the phase space, the bigger the volume, the more probable the configuration. This connection leads to the well established (in classical physics) relations between ergodicity and thermalization: in a thermal system the long-time and the phase space average of the physical observables coincide.

Classical thermalization is the result of the non-linearity of the equations of motion; quantum dynamics is instead governed by the Schrödinger equation that is linear, and this introduces difficulties in the definition of quantum thermalization for isolated quantum many body systems. A generic quantum many-body state is described by a density matrix ρ: for pure states $\mathrm{Tr}(\rho^2) = 1$ while for mixed ones $\mathrm{Tr}(\rho^2) < 1$. The linearity of the Schrödinger equation ensures that a system prepared in a pure state remains in a pure state for the whole dynamics ruling out the possibility of becoming thermal, i.e. mixed. Despite this, thermalization in closed many body quantum systems is observed. One of the first attempts of extension of these concepts to the quantum world is due to Von Neumann who in a work of 1929 [4] proved the H-theorem for quantum systems. This work does not say anything about the thermalization of microscopic quantities [3, 5] that can relax to equilibrium at the level of expectation values because of the canonical typicality: a pure state that has small energy fluctuations is locally indistinguishable from the microcanonical ensemble if the density of states is large [6, 7]. The paradox is solved by giving a definition of quantum thermalization in terms of expectation values of certain observables whose long-time limit tends to statistical predictions, i.e.

macroscopic variables tipically thermalize because energy eigenstates already share an essential character of thermal equilibrium, the so-called eigenstate thermalization hypotesis (ETH) [3, 5, 8–12].

The eigenstate thermalization hypothesis is widely discussed in Chapter 2, where we brefly review the principal results in the field of nonequilibrium quantum dynamics, starting from the dynamics of thermally isolated quantum many-body systems following a sudden quench, i.e. an instantaneous change in an Hamiltonian control parameter. The relation between quantum thermalization and quantum ergodicity is not simply established by imposing a correspondence between the classical statistical ensembles and the asymptotic quantum states, because thermalization occurs at the level of expectation values of macroscopic observables. An open question is to determine the conditions for the existence of the stationary state, defined as the density matrix describing the long-time behavior of the observables. For non integrable models, in which the energy is the only conserved quantity, the stationary state is a Gibbs ensemble at an effective temperature fixed by the quench. In integrable models, because of the presence of conservation laws, the thermal behavior is precluded and the stationary state is a Gibbs-like ensemble, the Generalized Gibbs ensemble (GGE), that maximizes the information entropy under the constraint of the conserved quantities. Once integrability is weakly broken the quantum system usually displays a two-stage dynamics: first it attains a prethermal nonequilibrium quasi-stationary state [13–21] (that can be thought of as a GGE constructed with the approximate constant of motion of the nearly-integrable Hamiltonian) and then, eventually, relaxes to a thermal one.

One of the most interesting features observed in nonequilibrium quantum many-body systems is the possibility of undergoing a dynamical quantum phase transitions, i.e. a relevant change in the dynamical behavior depending on the quench parameters. Two different kinds of dynamical phase transitions have been identified, one related to the geometric properties of the evolved quantum state, the other related to the long-time behavior of some physical observables [22–29]. Let us consider an equilibrium critical system prepared in a state of broken symmetry and let us assume to perform a quench. In analogy with the Landau paradigm for the second order quantum phase transition, a dynamical critical point is defined as the value of the quench parameter at which the dynamical order parameter, i.e. the long-time average of the evolved order parameter, exhibits a qualitative change in its behavior. These dynamical phase transitions are a consequence of the possibility of sustaining long-range order at finite density energy and, thus, cannot be observed in one dimensional short-ranged systems. Increasing the range of the interactions, because of the correspondence between the universality class of long-range interacting systems and short range ones with increased dimensionality, dynamical phase transitions can take place.

In this thesis we will focus on systems with long-range interactions. There are still open questions on the dynamics of long-range interacting systems due to technical difficulties in describing them because their non integrability. Moreover, the exponential growth of the Hilbert space rules out the possibility of exact numerical solutions. Approximate numerical techniques as the density matrix renormalization group (DMRG) have been adapted for long-range interacting models but the simulation of large system sizes still remains challenging. Despite this, experimental development in the ultracold gases field has given the access to a variety of quantum many-body long-range interacting systems renewing the interest in the understanding of their dynamics.

A special case of analytically solvable systems with long-range interactions is that of complete connected models, characterized by the permutational symmetry that allows a classical (and affordable) description both of the equilibrium and of the nonequilibrium physics. In Sec. 3.2 we present two examples: the Lipkin-Meshkov-Glick (LMG) model, describing a collection of N spin-1/2 particles with all-to-all interactions, and the Dicke models, describing a two level system coupled with an optical cavity. Both models exhibit an equilibrium quantum phase transition from a symmetry broken to a symmetric phase and the related nonequilibrium dynamical phase transition. Then we discuss three different experimental realizations with ultracold gases of the Ising chain with power-law decaying interactions described by the Hamiltonian

$$H = -\frac{J}{\mathcal{N}(\alpha)} \sum_{ij} |i-j|^{-\alpha} \; \sigma_i^z \sigma_j^z - h \sum_i \sigma_i^x , \tag{1.1}$$

with i, j, site index and $N(\alpha)$ the normalization constant. The main work in this thesis, presented in Chapter 4, contributes to the understanding of its dynamics by means of the cluster mean-field theory. The basic idea is to divide the chain in N_{cl} clusters of ℓ spins and to solve the dynamics of a cluster in the mean-field generated by the others. Mean-field models are exactly solved with $\ell = 1$ while, increasing the cluster dimension, short-range correlations are taken into account up to the limit $\ell \to \infty$ in which the exact dynamics is recovered.

We investigate the dynamics of the thermally isolated system following an instantaneous change in the transverse field. The system is prepared in the polarized state with all the spins aligned in the z direction, i.e. the ground state of the Hamiltonian in Eq. (1.1) with $h = 0$. At time $t = 0$ the transverse field is quenched to a finite value $h = 0 \to h > 0$. It turns out that the mean-field $\ell = 1$ predicts a sharp phase transition from a dynamical ferromagnet to a dynamical paramagnet at a dynamical critical point $h = 1$. While this is exact in the truly long-range regime $\alpha < 1$, for $\alpha \geq 1$ the dynamics is expected to deviate from the mean-field one by including the short range correlations. Increasing the cluster size, in fact, the critical point spreads in a critical region exhibiting hypersensitivity to the initial conditions, revealed by the alternation of positive and negative values of the dynamical order parameter. By virtue of a fine details analysis of the dynamical phase diagram we show the analogy with the dynamics of the tossed coin that can be predictable or truly random depending on the number of bounces the coin does. This is encoded in the geometry of the phase diagram: in the predictable case the transition from the phases, head and tail, is sharp while in the random regimes the edge between the two disrupts and the two phases intermingle. The robustness of the chaotic region can be investigated by quenching the transverse field with a finite velocity. Depending on the velocity of the quench three regimes can be identified. If the quench is fast enough the dynamical phase diagram displays the same chaotic features of the abrupt quench. In the adiabatic limit of vanishing velocities the system follows the ground state and the chaotic region disappears. In the intermediate regime the crossover between these two regimes occurs.

In the second part of the thesis we discuss the dissipative dynamics of open quantum systems. In the last years a lot of effort has been devoted to derive a formalism to describe the dynamics of a system in contact with an external bath, since this is the more realistic modeling of the experimental setups. As explained in Chapter 2.2, the dynamics of open quantum systems is obtained integrating a master equation, usually in a Lindblad form, for the density matrix ρ. Decoherence processes due to the presence of the bath allow the proper thermalization of the quantum systems but, at the same time, increase the computational effort. An exception is that of fully connected models whose mean-field nature reduces the complexity of the equations giving access to the dissipative dynamics. The dynamics of open quantum systems can be highly non-trivial. Recently it has been discussed the possibility of the existence of a spontaneous breaking of the continuous time-translational symmetry. A no-go theorem [30] ruled out the chance of observe it in equilibrium closed quantum systems but recent results have shown that such symmetry breaking is possible in open ones. In particular, experiments and theoretical works [31–38] have shown that in presence of periodic driving the system can respond sub-harmonically breaking the discrete time-translational symmetry. Recently, Russomanno and collaborators[39] have found that collective models, in presence of global dissipation processes[40] conserving the total angular momentum, can spontaneous break the continuous time-translational symmetry as a surface phenomenon, known as boundary time-crystal. We decided to investigate the stability of the boundary time crystal using the cluster mean-field theory. In Chapter 5 we derive the cluster mean-field equation for the fully connected Ising chain in presence of dissipative processes generated by string of Glauber operators. We show that for finite string operators the oscillations of the time-crystal are damped and the system eventually reaches a paramagnetic stationary state. We also investigate the effects of the finite range of the interaction solving the cluster mean-field dynamics increasing the power-law exponent α. The preliminary results suggest that for $\alpha > 1$ time-crystalline behavior cannot be sustained and the system settles in a stationary state that can be either ferromagnetic or paramagnetic.

This thesis is organized as follows. In Chapter 2 we present a brief review of quantum nonequilibrium dynamics. First we investigate the thermalization problem for thermally isolated quantum systems and then we describe the dynamics in the presence of an external environments. In Chapter 3 we introduce the general properties of the long range interacting quantum systems that are the focus of this thesis. First we introduce the physics of fully connected systems exploiting permutational invariance, then we discuss the consequences of breaking this symmetry and finally we propose three experimental realization of the power-law decaying interacting Ising chain. In Chapter 4 we first introduce the cluster mean-field theory that is used to investigate the dynamics of the long-range interacting Ising chain and then we discuss the results we have presented above. This chapter is largely taken from our published works [41, 42]. In Chapter 5 we derive the cluster mean-field Lindblad equations in presence of dissipation processes generated by string of Glauber operators. Then we present the mean-field dynamics of the Lipkin-Meshkov-Glick model in the two limiting cases of local and global Glauber operators and we apply the cluster mean-field to study the effects of the short correlations on this dynamics. Finally we study the stability of the time-crystal in case of string operators with a finite length N_s and in presence of finite range interactions $\alpha > 0$.

2

Non-equilibrium quantum systems

CONTENTS

In what follows we briefly introduce the general problem and the principal results of the nonequilibrium quantum dynamics. First we discuss the case of isolated quantum many-body systems with a particular focus on the thermalization problem and on the definition of dynamical phase transition. Then we move to the dynamics of the open quantum systems focusing on the technical details of its formulation and on the concept of time crystal.

2.1 Quantum quenches and dynamical phase transitions

The simplest nonequilibrium problem that can be considered is that of a thermally isolated quantum many-body system. The interest in these systems has been stimulated by the recent progresses in cold atoms that have allowed the simulation of quantum many-body systems that remain isolated for times longer than the relevant time scales of the dynamics.

The general nonequilibrium protocol we consider is the quantum quench, i.e. the abrupt change of one the Hamiltonian parameters. Let us consider a thermally isolated system described by a Hamiltonian $H(\lambda)$, with λ a tunable parameter, prepared in the ground state $|\psi_0\rangle$ of the fixed $\lambda \equiv \lambda_0$. At time $t = 0$ the parameter is abruptly changed to a different value $\lambda_0 \to \lambda$. The energy provided to the system by the quench can not be dissipated in the environment and, for thermalizing systems, it plays the role of an effective temperature T_{eff} fixed by the initial energy through the equation $\langle H\rangle_{T_{\text{eff}}} = \langle\psi_0|H|\psi_0\rangle$, where $\langle:\rangle_T$ is a thermal average [43]. The state at time t is unitarily evolved with the final Hamiltonian $|\psi(t)\rangle = e^{-iH(\lambda)t/\hbar}\,|\psi(t=0)\rangle$.

If the quench is performed with a finite velocity $\lambda(t) = \lambda_0 - vt$ and the velocity v is small enough compared to the gap of the spectrum Δ[1] the system follows adiabatically the ground state. In case of quench across the quantum critical point the closure of the gap does not allow adiabaticity and the state at time t differs from the ground state for the creation of some defects. This goes under the name of *Kibble-Zurek mechanism*, firstly stated for classical systems [44–47] and then extended to the quantum case [48–50].

2.1.1 Thermalization and quantum ergodicity

Classically the relation between thermalization and ergodicity refers to the equivalence between microcanonical and long-time averages of the physical quantities. In analogy to the classical case an intuitive generalization [11, 51, 52] to the quantum case could be to require the equivalence of the long-time density matrix $\overline{\rho(t)}$ and the microcanonical one

$$\overline{\rho(t)} \xrightarrow[t\to\infty]{} \rho_{\mathrm{mc}}. \tag{2.1}$$

Given an Hamiltonian H such that $H\left|\psi_\alpha\right\rangle = E_\alpha \left|\psi_\alpha\right\rangle$, the microcanonical density matrix is constructed by means of the eigenstates $\psi_\alpha \in \mathcal{H}(E)$, with $\mathcal{H}(E)$ the Hilbert subspace with a energy fixed between E and $E + \delta E$

$$\rho_{\mathrm{mc}} = \frac{1}{\mathcal{N}} \sum_{\psi_\alpha \in \mathcal{H}(E)} \left|\psi_\alpha\right\rangle \left\langle\psi_\alpha\right|, \tag{2.2}$$

where $\mathcal{N}$ is the number of eigenstates in the shell $\mathcal{H}(E)$. Given a generic initial condition in the microcanonical shell $\left|\psi\right\rangle = \sum_{\alpha\in\mathcal{H}(E)} c_\alpha \left|\psi_\alpha\right\rangle$, with $c_\alpha = \left\langle\psi|\psi_\alpha\right\rangle$, the density matrix at time t is

$$\rho(t) = \sum_{\alpha,\beta\in\mathcal{H}(E)} c_\alpha c_\beta^* e^{i(E_\alpha - E_\beta)t/\hbar} \left|\psi_\alpha\right\rangle \left\langle\psi_\beta\right|. \tag{2.3}$$

Assuming a non-degenerate spectrum, in the long time limit all the oscillating terms average out and the long-time averaged density matrix reduces to the so-called diagonal ensemble

$$\overline{\rho(t)} \to \rho_{\mathrm{diag}} = \sum_\alpha |c_\alpha|^2 \left|\psi_\alpha\right\rangle \left\langle\psi_\alpha\right|. \tag{2.4}$$

According to Eq. (2.1) ergodicity would require $|c_\alpha|^2 = \frac{1}{\mathcal{N}}$, $\forall\alpha$ and thermalization should be observed for a very restricted class of physical systems, contrary to what happens in the reality. The key to understand ergodicity is to focus on the long-time average[2] of the time evolution of a set of macroscopic quantum observables $\{M_\beta\}$ [5, 11, 12]: the system is ergodic whenever

$$\overline{\left\langle\psi(t)|M_\beta|\psi(t)\right\rangle} = \mathrm{Tr}\left(M_\beta \rho_{\mathrm{diag}}\right) = \left\langle M_\beta\right\rangle_{\mathrm{mc}}. \tag{2.5}$$

---

[1] Δ can be both a gap or an energy scale at which the spectrum qualitatively changes

[2] The definition is given in terms of long time average instead of asymptotic values since the long time limit in finite systems is not well defined because of quantum revivals. Despite this, if the expectation value of M_β relaxes to a well defined state this problem does not exist.

In general, the observable M_β thermalizes if (i) after some relaxation time the average expectation value coincides with the microcanonical one (quantum ergodicity) and (ii) temporal fluctuations of the expectation value about the microcanonical prediction are small at later times [9]. All those requirements can be encoded in the eigenstate thermalization hypothesis (ETH) that claims that all the energy eigenstates belong to the set of typical states and implicitly contain thermal states. As illustrated in the figure Fig. 2.1 [12], classical thermalization is due to the non-linearity of the equations of motion that makes a well localized initial condition to spread in the phase space, while quantum thermalization is due to the dephasing induced by the dynamics that, destroying the coherence between the eigenstates, brings out the thermal behavior. From an operative point of view, ETH is an ansatz for the matrix elements of local[3] observables O in the basis of the eigenstates of the Hamiltonian

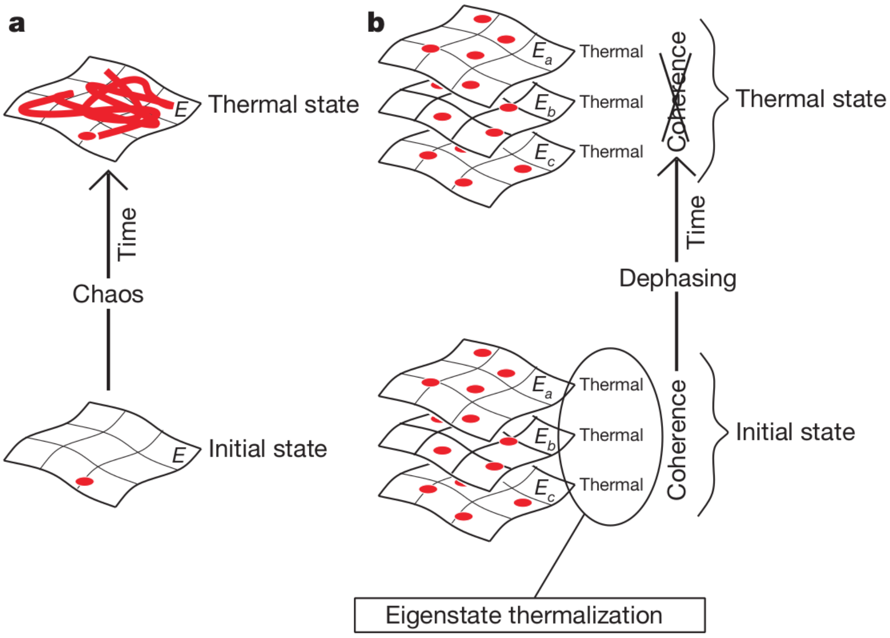

Figure 2.1: Schematic description (original in [12]) of the thermalization mechanism in classical and quantum systems. On the left it is represented the classical thermalization mechanism for which a well localized initial condition spreads on the phase space because of the non-linearity of the dynamics. On the right, pictorial description of the eigenstates thermalization hypothesis: energy eigenstates belong to the set of typical states and the dephasing induced by the dynamics destroys the coherence between the eigenstates bringing out the thermal behavior.

$$O_{mn} = O(\bar{E})\delta_{mn} + e^{-\frac{S(\bar{E})}{2}} f_O(\bar{E},\omega) R_{mn}, \tag{2.6}$$

with $\bar{E} = (E_m + E_n)/2$ and $\omega = E_n - E_m$. $S(\bar{E})$ is the thermodynamic entropy at the energy E, i.e. the logarithm of the number of eigenstates at that energy density,

---

[3] The validity of ETH has been proved for operators with support in up to 1/2 of the system size [10]

and R_{mn} is a random number with zero mean and unitary variance. The heart of the hypothesis is that $O(\bar{E})$ (that is identical to the expectation value of the microcanonical ensemble at energy $\bar{E}$) and $f_O(\bar{E},\omega)$ are two smooth functions in their arguments. Once assumed the ETH ansatz, thermalization follows automatically. There is not a rigorous proof of the validity of the ETH hypothesis, but many numerical and experimental evidences have shown that it holds, for instance, in the case of integrable Hamiltonians weakly perturbed or in the semi-classical limit of quantum systems whose classical counterpart is chaotic [12].

2.1.2 Thermalization and integrability

Given a set of macroscopic observables $\{M_\beta\}$, the stationary state ρ_{ss} is the density matrix that describes the long-time behavior of the observables

$$\rho_{ss} \iff \overline{\langle\psi(t)|M_\beta|\psi(t)\rangle} = \text{Tr}\left(M_\beta \rho_{\text{ss}}\right). \tag{2.7}$$

It is not obvious what guarantees the existence of the stationary states and this is still being debated in the scientific community. In a non integrable system, in which the energy is the only conserved quantity, the stationary state is thermal [3, 5, 11, 12, 43, 51, 52]. A local observable $O(t)$ approaches a thermal value at an effective temperature T_{eff} fixed by the initial energy

$$\overline{O(t)} = \text{Tr}\left(O\rho_{\text{ss}}\right) = \frac{\text{Tr}\left(e^{-\beta_{\text{eff}}H}O(t)\right)}{\text{Tr}\left(e^{-\beta_{\text{eff}}H}\right)}, \tag{2.8}$$

with $1/\beta_{\text{eff}} = T_{\text{eff}}$. In this case, the stationary state exists and is the Gibbs ensemble at T_{eff}

$$\rho_{\text{ss}} \equiv \rho_{\text{Gibbs}} = \frac{e^{-\beta_{\text{eff}}H}}{\text{Tr}\left(e^{-\beta_{\text{eff}}H}\right)}. \tag{2.9}$$

The locality of the operators can pictorially be thought as if the whole system acts as reservoir for any finite subsystem. Locality is the key requirement to observe thermalization. As a simple argument, let us consider the asymptotic behavior of a non local operator $O_{\alpha,\beta} = |\psi_\alpha\rangle\langle\psi_\beta| + |\psi_\beta\rangle\langle\psi_\alpha|$, its expectation value $\langle O_{\alpha,\beta}(t)\rangle = e^{i(E_\alpha - E_\beta)t/\hbar}c_\alpha^* c_\beta + h.c.$ exhibits persistent oscillations in time ruling out the possibility of a stationary value.

Integrable systems are an exception to the case discussed above. This was observed in an experiment in 2006 by Kinoshita *et al.* [53], who simulated the dynamics of trapped Bose gases both in the one-dimensional and the two-dimensional cases. They found that, whereas the 2D case shows thermal behavior, the 1D case, that is known to be integrable, does not approach thermal equilibrium. In fact, thermalization is not expected for integrable systems, i.e. systems with an extensive number of conserved quantities in which ergodic behavior is inhibited. In this case, analogously to the classical counterpart, the presence of the constants of motion precludes the possibility to attain a stationary state losing memory of initial conditions. Inspired by Jaynes works [54, 55], it has been understood [53, 56–64] that the asymptotic state attained will instead be the one that maximizes the information entropy subject to all constraints set by the constant of motion. It can be thought of as a generalization of the canonical ensemble that keeps trace of all conservation laws, thus is has been named generalized Gibbs ensemble (GGE) ρ_{GGE}. Given an extensive set of local[4] conserved quantities $\{I_n\}$ such that $[I_n, H] = 0$, the GGE reads

$$\rho_{\mathrm{GGE}} = \frac{e^{-\sum_n \mu_n I_n}}{\mathrm{Tr}\left(e^{-\sum_n \mu_n I_n}\right)}, \tag{2.10}$$

with μ_n the Lagrange multiplier associated to the operator I_n.

When integrability is explicitly broken ergodic behavior is expected to emerge. It has been shown that quantum thermalization is strongly linked to the emergence of quantum chaos [65, 66]. In the case of finite size many-body quantum system this link emerges in the crossover between the Poisson spectral statistics (integrable system) to the Wigner-Dyson one (chaotic system) [67–75]. The general hypothesis for the emergence of thermal behavior is the eigenstate thermalization hypothesis we discussed in Chapter 2.1.1. Once integrability is broken, the thermal state is attained in a time set by the energy scales in the systems, but it has been observed that sometimes the system stabilizes in an intermediate prethermal state. This problem has been first addressed in the high energy context [17] and later on in the condensed matter one [13–16, 18–21]. The prethermal state can be thought of as a GGE[5] constructed with the approximate constants of motion of the nearly integrable model; then it will eventually reach the thermal state [76]. Prethermalization could be interpreted in terms of fixed points of a renormalization-group flow. In this framework (depicted in Fig. 2.2) a prethermal state is a non-thermal (unstable) fixed point that is approached in early times and then left in favor of the thermal one. From this perspective, non thermal steady states attained by integrable models can be thought as non thermal fixed points with an infinite lifetime [77].

2.1.3 Dynamical quantum phase transitions

Recently it has been asked whether the concept of quantum phase transition can be extended to the nonequilibrium case. Two possible definitions of dynamical quantum phase transitions have been proposed. The first kind (DQPTs-I) is identified by a qualitative change in a dynamical order parameter [24–29, 41, 42], the second one (DQPTs-II) is signaled by the singularities in the Loschmidt amplitude [22, 23, 78–82].

Let us consider a quantum many body system prepared in the ground state $|\psi_0\rangle$ of an Hamiltonian H_0. At $t = 0$ the Hamiltonian is suddenly quenched to a different one $H_0 \to H$ and the state at time t $|\psi(t)\rangle = e^{-iHt}|\psi_0\rangle$ is evolved with the final Hamiltonian. The intuition of DQPTs-II is that the Loschmidt amplitude $\mathcal{G}(t) = \langle\psi(t)| e^{-iHt} |\psi(t)\rangle$, following a Wick rotation, i.e. $z = -it$, can be thought as a boundary partition function, i.e. $\mathcal{Z}(z) = \langle\psi(t)| e^{-zH} |\psi(t)\rangle$ with $z \in \mathbb{C}$. Defining

---

[4] If non-local constant of motion were allowed (e.g. choosing the projectors on the Hamiltonian eigenstates) we would obtain some tautological asymptotic state.

[5] The expectation values of the observables can be constructed by means of the perturbation theory [76]

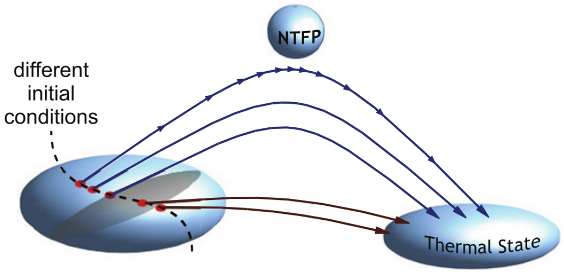

Figure 2.2: Schematic description of the prethermalization mechanism from the renormalization-group flow perspective (original figure in [16]). Whenever the dynamics is thermal (for instance, in case of non-integrable systems), the flow goes directly toward the stable thermal fixed points. Conversely, a near-integrable system quickly approaches a prethermalized state that retains memory of the initials conditions. This is a non-thermal unstable fixed points from which, after a certain time, the system escapes to eventually reach the thermal state. In this perspective, non-thermal steady states can be though as non-thermal fixed point with an infinite life-time.

the dynamical free energy density $f(z) = -\lim_{L\to\infty} \frac{1}{L} \ln Z(z)$, in direct analogy with standard statistical mechanics, the dynamical phase transition is signalled by the Fisher zeros in this boundary partition function, i.e. singularities in $f(z)$. In the temporal domain this leads to the emergence of critical times t_n^* where the rate function $l(t) = -\frac{1}{V} |\langle \psi(t)|\psi_0\rangle|^2$ displays non-analyticities. Despite have been experimentally observed [83, 84], their nature is essentially geometric and not connected to physical observables.

A different fate is reserved to the Landau-type dynamical phase transition that are, instead, connected to the existence of long-range order. Let us consider a quantum many body system exhibiting a $T = 0$ phase transition. Let us assume to prepare it in the ordered ground state $|\psi_0\rangle$ of the Hamiltonian H_0 and to quench to a different Hamiltonian $H_0 \to H$. If the system is thermalizing, the order parameter will behave consistently with the equilibrium finite temperature phase diagram. In absence of thermalization the quantum quench from a broken-symmetry phase can give rise to a dynamical phase transition. DQPTs-I, that are the focus of this thesis, are characterized by the value of the dynamical order parameter, that is defined as the long-time average $\bar{O} = \lim_{T\to\infty} \frac{1}{T} \int_0^T dt\, \langle O(t)\rangle$, with $O(t)$ the evolved equilibrium order parameter. The dynamical critical point separates a dynamical ordered phase, exhibiting a finite value of the dynamical order parameter, from a dynamical disordered one in which the order parameter vanishes. Since short-ranged system in small dimensions cannot sustain long-range order at a finite energy density, a key ingredient for its survival in nonequilibrium systems is the presence of long-range interactions, as we will discuss in Chapter 3. Although it is still under investigation the behavior of DQPTs-I is expected to be universal and its properties are expected to be different from the equilibrium counterpart [85]. These dynamical phase transitions have been observed in recent experiments [86, 87] with ultracold atoms.

2.2 Open quantum systems

Despite the technological progresses in the experimental implementations, closed quantum system are rather an idealization and, in general, it is impossible to engineer setups neglecting dissipation effects due to the external environment. To have a more lifelike description it is necessary to imagine the quantum system connected to an environment [88]. The environment, also named *bath*, is assumed to be very large with respect to the quantum system and acts as a reservoir in the canonical description of statistical mechanics. In what follows we present the general formalism to solve the dynamics of open quantum systems.

2.2.1 The general problem

Let us consider a many-body quantum system surrounded by an environment. The Hamiltonian describing this universe contains three terms

$$H = H_{\text{sys}} + H_{\text{bath}} + H_{\text{int}}, \tag{2.11}$$

that, respectively, refer to the coherent dynamics of the isolated quantum systems, to the dynamics of the reservoir degrees of freedom and to the interaction between these two. Despite this formalism being rather general, both in quantum optics and in condensed matter, usually the system is a collection of two level systems (e.g. Ising-like spin chains) whose physics can be expressed in terms of Pauli operators. The bath is usually modeled as a collection of harmonic oscillators

$$H_{\text{bath}} = \sum_l \int_0^\infty d\omega \hbar\omega b_l^\dagger(\omega) b_l(\omega), \tag{2.12}$$

where $b_l(\omega)$ are bosonic annihilation operators for ω frequency mode. l indicates multiple discrete modes at a given frequency, for instance a polarization index. The operators obey the commutation relation $[b_l(\omega), b_{l'}^\dagger(\omega')] = \delta(\omega - \omega')\delta_{ll'}$. Notice that in general the reservoir can have a frequency-dependent density of modes $g(\omega)$. The interaction Hamiltonian usually reads

$$H_{\text{int}} = -i\hbar \sum_l \int_0^\infty d\omega k_l(\omega) \left(x_l^+ + x_l^-\right) \left(b_l(\omega) - b_l^\dagger(\omega)\right), \tag{2.13}$$

where $x_l^\pm$ are system operators that couple to the mode ω $l-$boson with a strength $k_l(\omega)$. The operators $x_l^\pm$ depend on the system, e.g. for spin systems they are Pauli matrices $x_l^\pm = \sigma^\pm$, for harmonic oscillators they are bosonic operators $x^+ = a^\dagger$, but, usually, obey $[H_{\rm sys}, x_l^{\pm}] \approx \hbar\omega_l x^{\pm}$, being ω_l a frequency comparable to the system resonance frequency $\omega_{\rm sys}$. In general, all the processes present in the system are dominated by these frequencies that are also much larger than the frequencies scale of the dynamics due to the coupling with the environment. This allows to do the following three needful approximations.

- The *rotating wave approximation* (RWA): the energy non-conserving terms in the interaction Hamiltonian are neglected

  $$H_{\rm int} \approx -i\hbar \sum_l \int_0^{\infty} d\omega k_l(\omega) \left(x_l^+ b_l(\omega) - x_l^- b_l^{\dagger}(\omega) \right) . \tag{2.14}$$

  This approximation is justified by the fact that in the interaction picture the non-conserving terms acquire a time dependence rotating at twice the system frequency, effectively averaging to zero on the dynamical timescales relevant for the system.

- The *Born approximation*: the system-environment dynamical timescale is assumed to be much larger than the system one. This approximation holds whenever $\omega_{\rm sys} \ll \Gamma$, with Γ the frequency scale corresponding to the system dynamics induced by the environment.

- The *Markov approximation*: the system-environment coupling is assumed to be frequency/time independent on short timescales. Moreover, the bath relaxation times are assumed to be short (with respect to the system dynamical one) enough that the environment can be considered almost unchanged during the system dynamics and the back-action can be neglected. In few words, the evolution of the system does not depend on the history of the system.

The dynamics of the system is given by the evolution of the density matrix of the system obtained from the total density matrix simply tracing away the environment degrees of freedom $\rho = {\rm Tr}_{\rm env}\left(\rho_{\rm total}\right)$. Because of the presence of the external environment the dynamics is not unitary anymore and a pure state initial condition can equilibrate to a mixed state (for which ${\rm Tr}(\rho^2) < 1$). If on one hand this allows the system to properly thermalize, on the other one it complicates a lot the formal description of the equation of motion.

2.2.2 Dynamics: Lindblad master equations

Let us assume to have a quantum system living in the Hilbert space $\mathcal{H}$ whose dimension is $d_{\mathcal{H}}$. We define $\rho \in {\rm S}(\mathcal{H})$ the states of the system and $A \in {\rm Op}(\mathcal{H})$ the operators acting on it. We define the superoperators $\mathcal{A} \in {\rm SOp}(\mathcal{H})$ as a linear map between operators. Under the three approximations presented in Sec. 2.2.1 the Markovian evolution of the reduced system is generated by the Lindblad equation

$$\dot{\rho} = \mathcal{L}(\rho) = -\frac{i}{\hbar}[H_{\rm sys}, \rho] + \sum_m \gamma_m \left(L_m \rho L_m^{\dagger} - \frac{1}{2}\{L_m^{\dagger} L_m, \rho\} \right) . \tag{2.15}$$

$\mathcal{L}$ is a superoperator (the so-called *Lindbladian*) acting on the state ρ. The operators L_m are called Lindblad or jump operators describing the dissipative dynamics (including losses or decoherence processes) occurring at characteristic rate γ_m. The master equation can be re-arranged as follows

$$\dot{\rho} = -\frac{i}{\hbar}[H_{\text{eff}}, \rho] + \sum_m \gamma_m L_m \rho L_m^\dagger, \tag{2.16}$$

with $H_{\text{eff}} = H - \frac{i}{2}\sum_m L_m^\dagger L_m$ an effective Hamiltonian for the dissipative system. Because its non-hermitian structure, the effective Hamiltonian produces losses in the systems that are replaced in other states by the remaining term that is, for this reason, often called *recycling term* [88]. For example, in the case of a two level system with decay from the excited to the ground state, the dissipative part contributes to reduce the excited state amplitude while the recycling part reinstates this in the ground state.

Eq. (2.15) is a hermiticity-preserving equation, i.e. $\mathcal{L}(\rho^\dagger) = (\mathcal{L}(\rho))^\dagger$ that generates a family of completely-positive trace-preserving (CPTP) maps of the form $\mathcal{E}(t) = \exp(\mathcal{L}t)$. The latter is known as *evolution map* and is such that $\mathcal{E}(t + t') = \mathcal{E}(t) \cdot \mathcal{E}(t')$ and $\mathcal{E}(0) = \mathbb{I}$. The usual way to handle the master equation in Eq. (2.15) is by virtue of a *vectorization* process that is described in Subsec. 2.2.3.

2.2.3 Vectorization of the Lindblad master equations

The idea (more details can be found in [40]) is that linear operators form a vector space, hence can be represented as vectors of an enlarged Hilbert space. Given a basis $\{|i\rangle\} \in \mathcal{H}$ any operator can be written in this basis $A = \sum_{ij} a_{ij} |i\rangle \langle j| \in \text{Op}(\mathcal{H})$. The vectorization process replaces this operator with a vector

$$A \mapsto |A\rangle\rangle = \sum_{ij} a_{ij} |i\rangle \otimes |j\rangle \in \mathcal{H} \otimes \mathcal{H} \tag{2.17}$$

and superoperators $\mathcal{A} \in \text{SOp}(\mathcal{H})$ with operators in the enlarged Hilbert space

$$\mathcal{A}(A) \mapsto \mathcal{A}\,|A\rangle\rangle. \tag{2.18}$$

The inner product is given by the Hilbert-Schmidt product $\langle\langle A|B\rangle\rangle = \text{Tr}\left(A^\dagger B\right)$. The adjoint $\mathcal{A}^\ddagger$ of a superoperator $\mathcal{A}$ is defined as follows

$$\langle\langle A|\mathcal{A}(B)\rangle\rangle = \text{Tr}(A^\dagger \mathcal{A}(B)) \doteq \text{Tr}(\mathcal{A}^\ddagger(B)A) = \langle\langle \mathcal{A}^\ddagger(B)|A\rangle \tag{2.19}$$

with $A, B \in \text{Op}(\mathcal{H})$.

The major benefit of this formalism is that the Lindbladian $\mathcal{L}$ is treated as a matrix that can be diagonalized. Since it is not hermitian, we have to define both the left $|l_m\rangle$ and the right eigenvectors $|r_m\rangle$

$$\begin{cases} \mathcal{L}\,|r_m\rangle = \lambda_m\,|r_m\rangle\,, \\ \mathcal{L}^\ddagger\,|l_m\rangle = \lambda_m^*\,|l_m\rangle\,. \end{cases} \tag{2.20}$$

The spectrum of the Lindbladian contains much information on the dynamics of the system:

1. Eigenvalues are real or come by conjugate pairs. Because of the positivity it always is $\mathrm{Re}(\lambda_m) < 0$;
2. Ordinary eigenvectors corresponding to different eigenvalues are linearly independent;
3. Ordinary eigenvectors are bi-orthogonal $\langle\langle l_m | r_n \rangle\rangle = \delta_{mn}$, with δ_{mn} the Kroneker delta;
4. The evolution maps $\mathcal{E}(t)$ shares the same left and right eigenvectors of $\mathcal{L}$;
5. If $\mathcal{L}$ is time-dependent there is always $\lambda_0 = \lambda_0^* = 0$ with right eigenvector $|r_0\rangle\rangle$ such that $\mathcal{E}(t)\,|r_0\rangle\rangle = |r_0\rangle\rangle$. This state is the *steady state* of the system and it can be non-unique.

In general it is convenient to introduce the *asymptotic subspace* $\mathrm{As}(\mathcal{H}) = \mathrm{span}\{r_m : \mathrm{Re}(\lambda_m) = 0\}$. The states $|\psi\rangle_m \in \mathrm{As}(\mathcal{H})$ are more properly non-decaying states, in fact, whenever $\mathrm{Im}(\mathcal{H}) \neq 0$ they gain a time-dependent phase. The orthogonal subspace is the *dissipative subspace* $\mathrm{D}(\mathcal{H})$. The enlarged Hilbert space is the direct sum of the asymptotic and dissipative subaspaces $\mathcal{H} \otimes \mathcal{H} = \mathrm{As}(\mathcal{H}) \oplus \mathrm{D}(\mathcal{H})$. The last important concept is that of *dissipative gap* Δ

$$\Delta := \mathrm{min}_m |\mathrm{Re}(\lambda_m)| : \mathrm{Re}(\lambda_m) \neq 0. \tag{2.21}$$

This gap fixes the convergence to the asymptotic state time scale.

In order to implement the vectorized Lindblad equations it is necessary to generalize the left and right multiplication rules.

$$\begin{aligned} [H,\rho] &\mapsto \left(I \otimes H - H^T \otimes I\right) |\rho\rangle\rangle. \\ L_m^{\pm} \rho L_m^{\pm\dagger} &\mapsto \left(L_m^{\pm\dagger^T} \otimes L_m^{\pm}\right) |\rho\rangle\rangle, \\ L_m^{\pm\dagger} L_m^{\pm} \rho &\mapsto \left(I \otimes L_m^{\pm\dagger} L_m^{\pm}\right) |\rho\rangle\rangle, \\ \rho L_i^{\pm\dagger} L_i^{\pm} &\mapsto \left((L_i^{\pm\dagger} L_i^{\pm})^T \otimes I\right) |\rho\rangle\rangle. \end{aligned} \tag{2.22}$$

This way the Lindblad operators reduces to

$$\mathcal{L}^v = -i\left(I \otimes H - H^T \otimes I\right) + \sum_{\beta=\pm} \sum_m \gamma_m \left[L_m^{\beta\dagger^T} \otimes L_m^{\beta} - \frac{1}{2}\left(I \otimes L_m^{\beta\dagger} L_m^{\beta} + (L_m^{\beta\dagger} L_m^{\beta} \otimes I\right)\right] \tag{2.23}$$

2.2.4 Time crystals

One of the information contained in the Liouvillian spectrum is whether the system is in a time crystal phase. Time-crystallinity is a concept that has been introduced by Wilczek in the 2012 [89] in analogy with the concept of crystals, a phase of matter emerging by the spontaneous breaking of the translational symmetry. A time crystals, therefore, is a phase a matter that spontaneously breaks the time-translational symmetry is spontaneously broken. This breaking is revealed by a non trivial time dependence of physical observables. A no-go theorem [30] ruled out the existence of this state of matter in equilibrium systems in which the energy is conserved, although time crystals are still allowed in non-equilibrium quantum systems. In general, their existence is foretold by the Liouvillian spectrum that is expected to have a vanishing gap in the real part (a degenerate nonequilibrium steady-state with coherence decaying over an infinite time scale) and some non-zero imaginary eigenvalues inducing the oscillations. A particular case of time crystals are that emerging in Floquet (i.e. periodically driven) systems [37, 38], in which the discrete time-translational symmetry imposed by the external driving is spontaneously broken[31–35, 40]. These time crystals, named Floquet time crystals, are revealed by the dynamics of the physical observables that oscillate at a frequency multiple of the driving one.

Time crystals are usually destroyed by the presence of dissipative processes. In some cases [35], e.g. mean-field models with collective interactions [40], the dissipation concurs to stabilize the time-crystallinity. In presence of dissipation a continuous time-translational symmetry breaking can be observed as surface phenomenon, the so-called boundary time-crystals (BTCs) [39]. Basically, the system self-organizes in a time-periodic pattern only in a macroscopic fraction of itself (the surface) on a period that depends only on the coupling with the rest of the system (the bulk). Being $\hat{O}_\mathrm{s}$ an operator acting on the surface, the boundary time crystal is observed if its expectation value $\langle \hat{O}_\mathrm{s}(t) \rangle$, in the thermodynamic limit, is a time-periodic function $f(t)$

$$\langle O_\mathrm{s}(t) \rangle \equiv \lim_{\substack{N_\mathrm{s}, N_\mathrm{b} \to \infty \\ N_\mathrm{s}/N_\mathrm{b} \to 0}} \mathrm{Tr}\left(O_\mathrm{s} \rho_\mathrm{s}(t) \right) = f(t), \tag{2.24}$$

with $N_\mathrm{s}, N_\mathrm{b}$ the degrees of freedom of the surface and of the bulk respectively. The correspondence between the dissipative dynamics and the unitary dynamics of an enlarged system suggests that the existence of a BTC is correlated with the existence, in the thermodynamic limit, of a time-periodic steady state in an open quantum many-body system. Some reminiscence of this behaviour could be observed even in finite systems with some early time oscillations of the boundary order parameter.

Further details can be found in the reviews [40, 90, 91].

3

Long-range interacting systems

CONTENTS

In this chapter we describe the physics of long-range interacting quantum systems with a particular focus on the experimentally relevant case of algebraic decaying potentials $V(r) \propto Jr^{-\alpha}$. First we describe the general properties of this kind of potentials, then we discuss the particular case of the completely connected models. Finally we introduce the long-range interacting Ising model and present some experimental realizations.

3.1 Algebraic decaying potentials

Algebraic decaying potentials are long-ranged whenever the power law exponent α is smaller than the dimensionality d. Long-range interactions lead to non-extensive ground state energies and thermodynamics. This intuitively emerges calculating the interaction energy of a particle placed at the center of a d-dimensional sphere of radius R. In case of a power law decaying potential it goes as $\varepsilon \propto R^{d-\alpha}$ and is finite provided $\alpha > d$, while diverges otherwise implying a superlinear growth of the total energy [92] . Extensivity can be formally recovered renormalizing[1] the coupling constant $J \mapsto JV^{\alpha/d-1}$ [93].

Long-range interactions are non-additive. As a simple argument let us consider the Curie-Weiss model $H_{CW} = -\frac{J}{N}\sum_{ij}^{N} s_i s_j$, with $s_i = \pm 1$ spin variables acting on the site i. The total energy of a bipartite configuration of L spins with $s_{i\leq L/2} = 1, s_{i>L/2} = -1$ is $E = 0$ although the energy of a single partition is

---

[1] It is not obvious that the interaction depends on the numbers of the interacting particles, but the normalization is necessary to obtain meaningful mathematical and statistical properties.

$E_1 = E_2 = -JN/2$. The principal consequence of non additivity in case of classical long-range interacting systems is the lack of convexity in the thermodynamic potential affecting the construction of the statistical ensembles and yielding peculiar dynamical behavior. Long-range interactions imply also non trivial quantum dynamics as a consequence of the ultrafast spreading of correlations violating the Lieb-Robinson bound [94–102] or the counterintuitive slowdown of the growth of the entanglement entropy becoming more pronounced as one increases the range of the interactions [103, 104].

The most intriguing features exploited by long-range interacting systems is the equivalence between the universality class of long-range interacting systems and short-range ones with an increased dimensionality [105, 106] that implies the possibility of sustaining long-range order at finite energy density in low-dimensions. In the case of a 1D spin chain this can be understood by considering the Peierls argument that the long-range order at finite temperature is destroyed by the creation of domain-wall excitations. Considering a long-range ordered state, the energy to create a domain-wall separating two long-range ordered regions is $\Delta E_{\mathrm{dw}} \sim \sum_{r>0} r^{1-\alpha}$. Thus, the formation of domain-walls is energetically accessible only for $\alpha \geq 2$ and is prevented for $\alpha \leq 2$ allowing long-range ordering at finite temperature. As a consequence, long-range interacting systems can display a dynamical quantum phase transition as the ones described in Sec. 2.1.3.

3.2 Fully connected quantum many body systems

A particular case of long-range interactions is that of fully connected quantum many-body systems, i.e. power law potentials with exponent $\alpha = 0$. These systems are symmetric under permutations of any site and the dynamics is constrained to the so-called totally-symmetric-subspace (TSS) [103, 107–109]. This introduces huge simplifications because the dimension of the TSS, instead of growing exponentially, grows just polinomially with the system size N. Moreover the Schrödinger equation involves an effective Planck constant $\hbar_{\mathrm{eff}} \sim 1/\sqrt{N}$ and, in the thermodynamic limit, reduces to the Hamilton equation of few macroscopic variables [103, 107–110]. The classical description is obtained by mapping quantum operators on their semi-classical counterpart [110], e.g. by virtue of the phase space formulation of quantum machanics presented in Appendix A. The semi-classical approximation is valid only for the early stage of the dynamics and breaks down at the Ehrenfest time t_E [110–112], i.e. the time at which the wave packet spreads on scales at which the quadratic approximation of the Hamiltonian fails.

In what follows we describe two prototypical, experimentally relevant, examples of completely connected systems exhibiting collective behavior: the Lipkin-Meshkow-Glick model (Sec. 3.2.1) describing the physics of a collection of N spin 1/2 with a all-to-all interaction and collections of two-level or three-level systems coupled to a radiation field (Subsec. 3.2.2). The derivation of the effective Hamiltonian both for the radiation field and for the two-level systems can be found in [113].

3.2.1 Lipkin-Meskov-Glick model

The Lipkin-Meshkov-Glick (LMG) model was proposed in the 1965 [114] to describe a system of N interacting bosons. By means of a Schwinger mapping, the bosonic operators can be replaced by spin ones with total angular momentum $S = N/2$. Alternatively [115–117], it can be thought of as chain of N spin-$\frac{1}{2}$ particles mutually interacting through an anisotropic XY-like Hamiltonian coupled to an external magnetic field h:

$$H = -\frac{2}{N}\left(\gamma_x S_x^2 + \gamma_y S_y^2\right) - hS_z, \tag{3.1}$$

with $S_\alpha = \sum_{i=1}^N S_\alpha^i$ and S_α^i spin operators acting on the site i. Without loss of generality we assume $h \geq 0$ and $|\gamma_y| \leq \gamma_x$. The spin operators obey the SU(2) commutation relations $[S_j^\alpha, S_l^\beta] = i\hbar\delta_{jl}\varepsilon_{\alpha,\beta,\gamma}S_j^\gamma$. The algebra of the collective spin operators $s^\alpha = S^\alpha/N$

$$[s^\alpha, s^\beta] = i\frac{\hbar}{N}\delta_{jl}\varepsilon_{\alpha,\beta,\gamma}s^\gamma, \tag{3.2}$$

reduces to a SU(2) algebra with an effective Planck constant $\hbar_{\text{eff}} = \hbar/N$. The Hamiltonian in Eq. (3.1) is invariant under permutations, hence the system is constrained in the total symmetric subspace. For the SU(2) algebra the TSS is spanned by the so-called Dicke states $\{|s, m\rangle\}$, i.e. the standard basis of S^2 and S_z, with $S^2 |s, m\rangle = s(s+1)|s, m\rangle$ and $S_z |s, m\rangle = m |s, m\rangle$. The Hamiltonian in Eq. (3.1) conserves the number of excitations and the odd-m and even-m sectors are decoupled, making the model $\mathcal{Z}_2$ symmetric. The total angular momentum is conserved constraining the dynamics to the maximum angular momentum sector[2] $s = N/2$. The system is equivalent to a classical $(N+1)$-level system whose dynamics is that of the Bloch vector precessing on the Bloch sphere. It exhibits a quantum phase transition explicitly breaking the $\mathcal{Z}_2$ symmetry at the critical values $h_c = \gamma_x$ and $h_c = \gamma_y$. The phase transition is recovered by the classical description obtained posing

$$S^x = \sin\theta\cos\varphi, \quad S^y = \sin\theta\sin\varphi, \quad S^z = \cos\theta, \tag{3.3}$$

and minimizing the Hamiltonian H_{cl}

$$H_{\text{cl}} = -(1+\gamma)\sin^2\theta\cos^2\varphi - (1-\gamma)\sin^2\theta\sin^2\varphi - 2h\cos\theta, \tag{3.4}$$

with $\gamma_x = 1+\gamma$ and $\gamma_y = 1-\gamma$. The minimization yields two ground state solutions

$$\begin{cases} S^x = \sqrt{1 - \frac{h}{1+\gamma}} \iff \gamma > 0, \\ S^x = 0 \iff \gamma < 0. \end{cases} \tag{3.5}$$

---

[2] This choice is due to the fact that the ground state of Eq. (3.1) belonging to the maximum angular momentum sector.

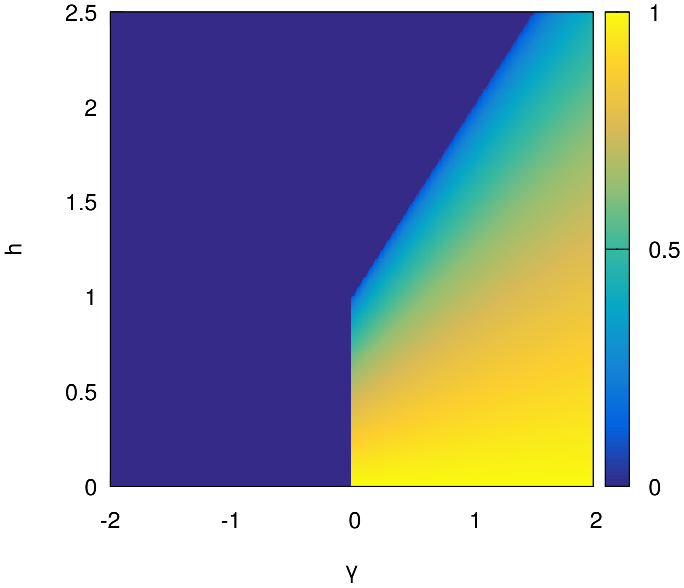

Figure 3.1: Equilibrium phase diagram of the infinite XY-model. The order parameter $\langle S^x \rangle$ (color map) is plotted as a function of the interaction constant γ and the transverse field h. The system undergoes a quantum phase transition from a ferromagnetic (broken) to a paramagnetic (symmetric) one at a critical value $h_c(\gamma)$.

corresponding to the normal and the broken phase. The equilibrium phase diagram is shown in Fig. 3.1 where the order parameter S^x (color map) is plotted as a function of the coupling γ and the transverse field h.

The dynamics of the LMG is obtained integrating the Hamilton equations for the conjugate variables $\varphi, \cos\theta$ [115]

$$\begin{aligned} \partial_t \varphi(t) &= -\gamma \sin^2\theta \sin(2\varphi), \\ \partial_t \cos\theta(t) &= 2p(1+\gamma\cos(2q)) - 2h. \end{aligned} \tag{3.6}$$

In the case of a quench from $(\gamma_i = 1, h_i = 0)$ to (γ, h) the solution is analytical [115]

$$\begin{aligned} \varphi(t) &= \arctan\left(-\frac{K^- sn\left(2tK^+ | (K^-/K^+)^2\right)}{\sqrt{2(\gamma-1)\gamma + h^2}} \right), \\ \cos(\theta(t)) &= \frac{h - \sqrt{h^2 - 2\gamma \sin^2\varphi(\gamma\cos(2\varphi)+1)}}{\gamma\cos(2\varphi)+1}, \end{aligned} \tag{3.7}$$

with $K^\pm = \sqrt{-h^2 + \gamma^2 + \gamma \pm |\gamma| \sqrt{(\gamma+1)^2 - 4h^2}}$ and $sn(u|m)$ one of the Jacobi elliptic function. The collective dynamics is that of a macroscopic degree of freedom preceding on the Bloch sphere. In Fig. 3.2 we show the phase space trajectories for $\gamma = 1$ and for the three final transverse fields $h = 0.5$ (left panel), $h = 1.0$ (right panel) and $h = 1.5$ (middle panel) for the initial condition $\varphi = 0, \cos\theta = 1$.

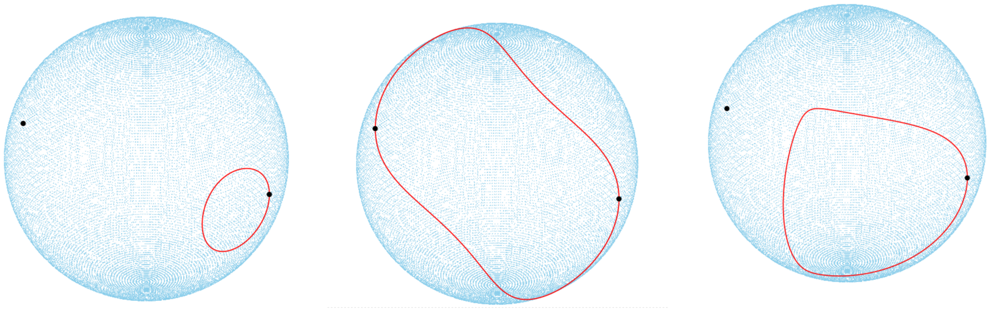

Figure 3.2: Trajectories of the order parameter S^x on the Bloch sphere for $\gamma = 1$. The system, prepared in the ground state of the Hamiltonian with $h = 0$ (black dots), is quenched toward three different values of the transverse field (from left to right) $h = 0.5$ (dynamical ferromagnet), $h = 1.5$ (dynamical paramagnet) and $h = 1.0$ (dynamical critical point). In the dynamical ferromagnetic phase the spin precedes around the initial condition and the long-time averaged magnetization has a finite value. In the dynamical paramagnetic phase the spin precedes around the two ferromagnetic ground states and the order parameter vanishes. In the right panel we plot the critical trajectory for $h = 1$: the spin slowly approaches the paramagnetic point to eventually escape after a time increasing with the system size. This trajectory is unstable under any perturbation.

When the transverse field is small the vector precedes close the initial condition and is characterized by a finite long-time average magnetization, conversely when the transverse field is large the precession follows the equator of the sphere implying a vanishing long-time average magnetization. The crossover between these two regimes occurs at a critical value $h_c = 1$. The associated phase space trajectory, that approaches exponentially slowly the equilibrium paramagnetic point, is extremely unstable under perturbations. The system undergoes a dynamical phase transition from a dynamical ferromagnetic phase characterized by a finite value of the dynamical paramagnetic order parameter $\overline{S^x} = \lim_{T\to\infty} \frac{1}{T}\int_0^T dtS^x(t)$, to a dynamical paramagnetic one with $\overline{S^x} = 0$. The dynamical phase diagram is shown in Fig. 3.3 where the dynamical order parameter $\overline{S^x}$ (color map) is plotted as a function of the post-quench coupling γ and the post-quench transverse field h.

The failure of the semi-classical approximation emerges by looking at the stability of the quadratic bosonic approximation obtained by means of the Holstein-Primakoff transformation:

$$S^+ = \sqrt{2N - b^\dagger b}\, b, \qquad S^z = 2N - b^\dagger b, \tag{3.8}$$

with $S^+ = S^x + iS^y$. Expanding the roots we obtain:

$$\begin{cases} S^x \sim \sqrt{2N}(b^\dagger + b) + O(1/\sqrt{N}), \\ S^y \sim i\sqrt{2N}(b^\dagger - b) + O(1/\sqrt{N}), \\ S^z = 2N - b^\dagger b. \end{cases} \tag{3.9}$$

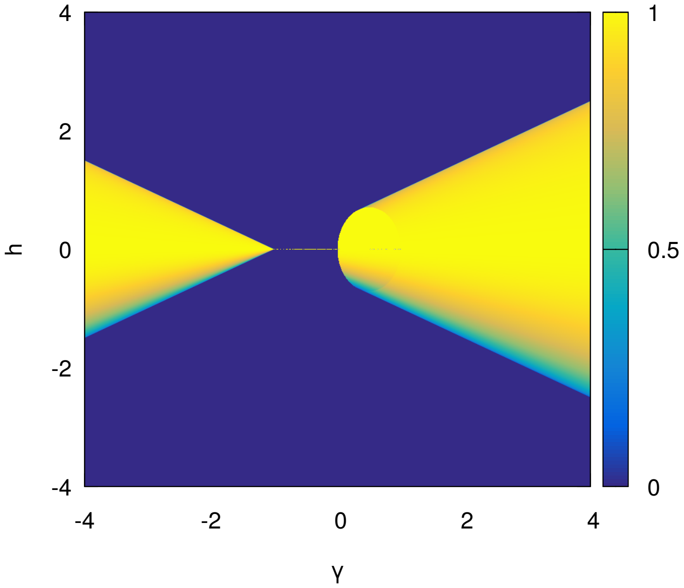

Figure 3.3: Dynamical phase diagram for the infinite range XY-model, derived by integrating the equations of motion in Eq. (3.6). The system, prepared in the ground state of the Hamiltonian with $h_i = 0$, is quenched toward a final value of the transverse field h. It shows the dynamical order parameter $\overline{S^x}$ (color map) as a function of the interaction constant γ and the final transverse field h.

Substituting, the Hamiltonian becomes

$$H = -N(h+J) + 2\varepsilon b^\dagger b + \lambda\left(b^{\dagger^2} + b^2\right), \tag{3.10}$$

with $\varepsilon = \gamma - J$, and $\lambda = -\gamma$. Neglecting the constant, it can be diagonalized

$$H = \sqrt{J(J-\gamma)}a^\dagger a, \tag{3.11}$$

performing a Bogoliubov rotation $b = \cosh\alpha \; a - \sinh\alpha \; a^\dagger$, with $\cosh 2\alpha = \frac{\varepsilon}{\sqrt{\varepsilon^2-\lambda^2}}$ and $\sinh\alpha = -\frac{\lambda}{\sqrt{\varepsilon^2-\lambda^2}}$, The stability condition $E^2 > 0$ locates the critical point at $h_c = \gamma$ for $\gamma > 0$ and confirms the absence of phase transitions for $\gamma < 0$. The quadratic approximation in Eq. (3.10) holds as long as $b^\dagger b \ll N$, namely up to the Eherenfest time t_E given by the relation $\langle (b^\dagger b)(t_E)\rangle \sim N$. For collective spin systems the Ehrenfest time grows as $t_E \propto \sqrt{N}$ away from the critical point, while at the dynamical critical point goes as $t_E \propto \log N$ [118]. We evaluate the evolution of the density of fluctuations by integrating of the equations of motion of the correlators $\Delta_b = 2b^\dagger b$, $\Delta_r = \left(b^\dagger + b\right)^2$, $\Delta_i = -\left(b^\dagger - b\right)^2$

$$\begin{cases} \dot{\Delta}_b = 4\lambda\Delta_i, \\ \dot{\Delta}_r = -4\epsilon\Delta_i, \\ \dot{\Delta}_i = 4\epsilon\Delta_r + 4\lambda\Delta_b. \end{cases} \tag{3.12}$$

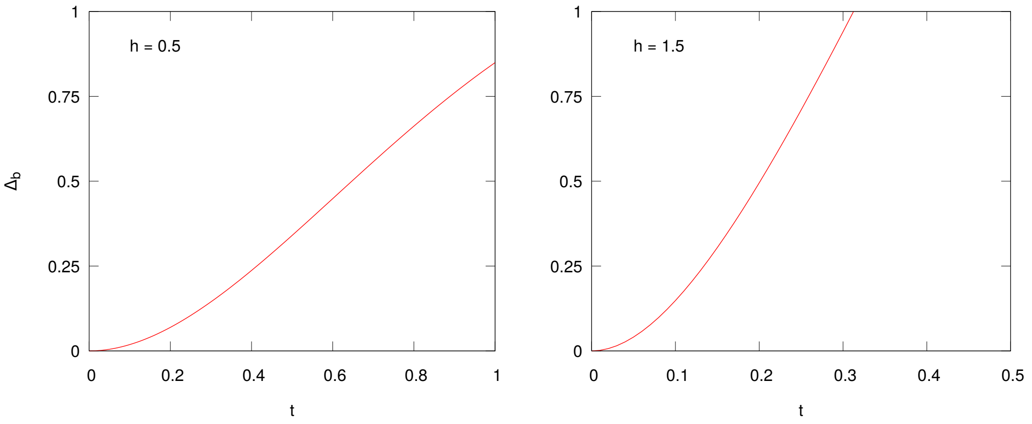

Figure 3.4: Trajectories of Δ_b as a function of time for two different transverse fields $h = 0.5$ (left panel) and $h = 1.5$ (right panel). The growth of the fluctuations in time is responsible of the failure of the semi-classical approximations of the dynamics.

In Fig. 3.4 we plot the trajectories of Δ_b as a function of time in the ferromagnetic (left panel) and in the paramagnetic phase (right panel). We observe a growth of the fluctuations in time that is responsible of the failure of the semi-classical description of this model. As explained in Appendix B, this growth is related to the spin squeezing.

3.2.2 Atoms in cavities

The simplest example of collective phenomena in quantum optics is the Dicke's superradiance (also referred as superfluorescence), i.e. the coherent emission of light by a set of N two-level systems coupled to a radiation field. A single two-level system prepared in the excited state $|\uparrow\rangle$ if coupled to an electromagnetic environment could relax to the ground state $|\downarrow\rangle$ emitting a photon with a rate γ_s. A collection of N two level systems prepared in the excited state $|\uparrow\dots\uparrow\rangle$ could relax to the ground state $|\downarrow\dots\downarrow\rangle$ spontaneously emitting photons with a rate $N\gamma_s$. In the 1954 Dicke [119] showed that this model undergoes a phase transition (first described by Hepp and Lieb [120] and then mathematically stated by Wang and Hioe [121]) from a normal phase, in which the spontaneous emission is incoherent and occurs with an intensity N, to a superradiant phase in which the measured radiation field is proportional to N^2. The system shows both a classical and a quantum (at $T = 0$) phase transition from a normal to a superradiant phase that in the last years has been the focus of many studies both at equilibrium [122–128] and out of equilibrium [126, 129–131]. In particular, a strongly debated issue is the actual possibility of observing a superradiant quantum phase transition.

The associated model is a collection of N two-level systems interacting via dipole interaction with M bosonic modes within an ideal optical cavity, isolated from the

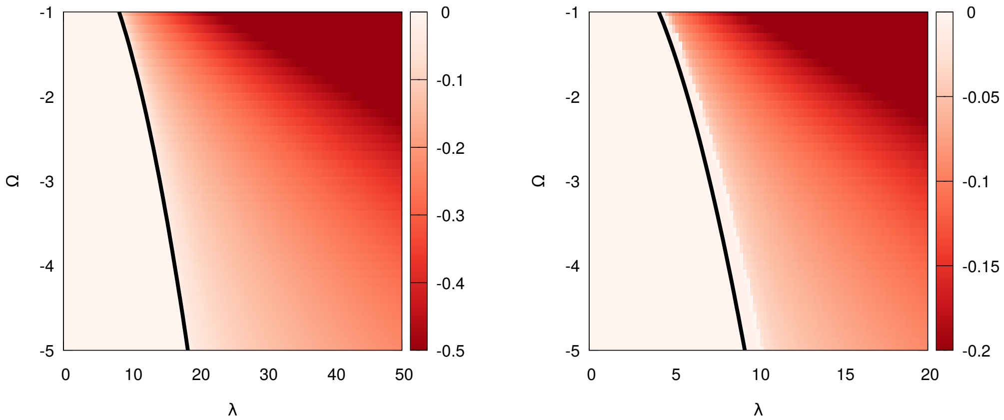

Figure 3.5: Left panel: equilibrium phase diagram of the Dicke model. The ground state value of φ (color map) is plotted as a function of the coupling constant λ and the cavity frequency Ω fixed $\omega = 1$. The black line is the critical value $\lambda_c = \sqrt{\Omega}/2$. Right panel: dynamical phase diagram of the Dicke model. The long-time average $\overline{\varphi}$ (color map) is plotted as a function of the post-quench coupling constant λ and the cavity frequency Ω fixed $\omega = 1$. The black line is the empirical critical value $\lambda_c^d = \lambda_c/2$.

external environment. The relative quantum Hamiltonian reads

$$H = \sum_{\ell}^{M} \Omega_\alpha \; a_\ell^\dagger a_\ell + \omega \; \sigma^z + \sum_{\alpha}^{M} \frac{\lambda_\ell}{\sqrt{N}} \left(a_\ell^\dagger + a_\ell \right) (\sigma^+ + \sigma^-), \tag{3.13}$$

with $a_\ell(a_\ell^\dagger)$ annihilation (creation) operators for the mode ℓ and $\sigma^\alpha = \sum_i \sigma_i^\alpha$ collective spin operators with σ_i^α Pauli matrices acting on the site i-th and $\sigma^\pm = (\sigma^x \pm i\sigma^y)/2$. The coupling constant normalization is due to the fact that the dipole strength is proportional to $1/\sqrt{V}$, with $V = N/\rho$ the volume of the cavity. In the 1975 Rzażewski and collaborators [132] observed that the Hamiltonian in the Eq. (3.13) is not invariant under gauge transformation of the electromagnetic field. To recover the gauge invariance one needs a term proportional to the square of vector potential whose strength, fixed by the Thomas-Reiche-Kuhm sum rule, is such to inhibit the quantum phase transition, leading to a no-go theorem [132, 133]. Successive works have shown that the superradiant quantum phase transition can be observed in the nonequilibrium steady state (NESS[3]) of the driven dissipative version of the model [126, 134–136]. Physically, one can realize this transition by looking at a Bose-Einstein condensate (BEC) posed in an ideal quantum optical cavity, dressed by an external pump. Depending on the cavity and pumping parameters (see Appendix C) the BEC can arrange on a periodic structure of two-level systems that, in a reference frame moving at the pump frequency, is described by the

---

[3] NESS superradiant quantum phase transitions are qualitatively similar to the equilibrium quantum ones, but their universality class (that is the same of the classical superradiant phase transition) differs from the quantum one [130]

Hamiltonian in Eq. (3.13) [130, 135–137]. The spin Hilbert space (see Subsec. 3.2.1) is the TSS spanned by the Dicke states $\{|j,m\rangle\}$, with $\sigma^2\,|j,m\rangle = j(j+1)\,|j,m\rangle$ and $\sigma^z\,|j,m\rangle = m\,|j,m\rangle$, while the bosonic Hilbert space is spanned by the Fock states $|n\rangle$ of the radiation field. The total Hilbert space, spanned by the product basis $\{|n\rangle\otimes|j,m\rangle\}$, is split into two subspaces reflecting the parity symmetry associated to the operator $\Pi = \exp\left(i\pi\hat{N}\right)$, with $\hat{N} = \sum_l a_l^\dagger a_l + \sigma^z + j$. The underlying symmetry group, spontaneously broken by the superradiant quantum phase transition, is $\mathcal{Z}_2$. In what follows we fix $j = N$.

Let us now focus on the Dicke model, i.e. the case with a single cavity mode. By virtue of the Holstein-Primakoff in Eq. (3.9) the Hamiltonian can be written as

$$H = \Omega\; a^\dagger a + \omega\; b^\dagger b + \frac{\lambda}{\sqrt{N}}\left(a^\dagger + a\right)\left(b^\dagger\;\sqrt{N-2b^\dagger b} + \sqrt{N-2b^\dagger b}\;b\right). \tag{3.14}$$

The system undergoes a quantum phase transition from a symmetric phase, characterized by $\langle a^\dagger a\rangle, \langle b^\dagger b\rangle = 0$, to a broken superradiant one with $\langle a^\dagger a\rangle, \langle b^\dagger b\rangle \sim N$. The associated classical Hamiltonian

$$H/N = \Omega|\varphi|^2 + \omega|\psi|^2 + 4\lambda\varphi^r\psi^r\psi_0, \tag{3.15}$$

is given[4] by the substitution $a \mapsto \sqrt{N}\varphi$ and $b \mapsto \sqrt{N}\psi$ fixed $\psi_0 = \sqrt{1-|\psi|^2}$, with $\varphi,\psi \in \mathbb{C}$ [108]. The ground state, obtained by minimizing the Hamiltonian with respect to the fields, is in the normal $\varphi,\psi = 0$ or in the superradiant phase $\varphi,\psi > 0$ if the coupling is smaller o bigger than the critical value $\lambda_c = \sqrt{\omega\Omega}/2$. The equilibrium phase diagram is shown in the left panel of Fig. 3.5 where the ground state value of φ^2 (color map) is plotted as a function of the coupling constant λ and the cavity frequency Ω (fixed $\omega = 1$). The black line is the critical coupling $\lambda_c = \sqrt{\Omega}/2$. Let us assume to prepare the system in the superradiant ground state of some parameter λ_i, Ω_i and to quench the parameters to some final values λ, Ω. The dynamical phase diagram, displayed in the right panel of Fig. 3.5, shows the dynamical order parameter $\overline{\varphi(t)} = \lim_{T\to\infty}\int_0^T dt\varphi(t)$ (color map) as a function of the post-quench coupling λ and the post-quench cavity frequency Ω. The system undergoes a superradiant dynamical phase transition at a critical coupling that is empirically located at $\lambda_c^d = \lambda_c/2$ (black line).

Including the fluctuations means to map $a \mapsto \varphi + a$ and $b \mapsto b + \psi$, with $\varphi = \varphi_r + i\varphi_i$ and $\psi = \psi_r + \psi_i$. The total Hamiltonian contains a quadratic term h_2

$$\begin{aligned} h_2 = \Omega a^\dagger a + \left(\omega - \frac{4\varphi_r\psi_r}{\psi_0}\right) b^\dagger b - \frac{\lambda\varphi_r\psi_r\left(\psi_r\Delta_b^r + \psi_i\Delta_b^i\right)^2}{2\psi_0^2} \\ - \frac{\lambda\Delta_a^r\left((\psi_r^2 - \psi_0^2)\Delta_b^r + \psi_r\psi_i\Delta_b^i\right)}{\psi_0}, \end{aligned} \tag{3.16}$$

with $\Delta_x = 2x^\dagger x$, $\Delta_x^r = x^\dagger + x$ and $\Delta_x^i = i(x^\dagger - x)$. The equation of motions for the

---

[4] Another possibility is to derive the classical Hamiltonian in terms of the conjugate variables x and p as done in [127, 128]

correlators

$$\begin{cases} \dot{\Delta}_a = \frac{2\lambda\Delta_a^i((\psi_r^2-\psi_0^2)\Delta_b^r+\psi_r\psi_i\Delta_b^i)}{\psi_0} \\ \dot{\Delta}_a^r = 2\Omega\Delta_a^i, \\ \dot{\Delta}_a^i = -2\Omega\Delta_a^r + \frac{2\lambda((\psi_r^2-\psi_0^2)\Delta_b^r+\psi_r\psi_i\Delta_b^i)}{\psi_0}, \\ \dot{\Delta}_b = 2\left(\frac{\lambda\varphi_r\psi_r(\psi_r-\psi_i)}{\psi_0^2}\right)\Delta_b^r\Delta_b^i - \frac{2\lambda\psi_r\psi_i\Delta_a^r\Delta_b^r}{\psi_0} + \frac{2\lambda(\psi_r^2-\psi_0^2)\Delta_a^r\Delta_b^i}{\psi_0}, \\ \dot{\Delta}_b^r = 2\left(\omega - \frac{\lambda\varphi_r\psi_r\psi_i}{\psi_0^2}\right)\Delta_b^i - \frac{2\lambda\psi_r\psi_i\Delta_a^r}{\psi_0}, \\ \dot{\Delta}_b^i = -2\left(\omega - \frac{\lambda\varphi_r\psi_r^2}{\psi_0^2}\right)\Delta_b^r + \frac{2\lambda(\psi_r^2-\psi_0^2)\Delta_a^r}{\psi_0} \end{cases} \tag{3.17}$$

have a structure similar to those derived for the LMG model in Subsec. 3.2.1 and actually the number of fluctuations Δ_a, Δ_b grows in time causing the failure of the semiclassical approximation at the Ehrenfest time.

Emary and collaborators [127, 128] have shown the correspondence between the classical chaotic behavior of the Dicke model and the quantum chaotic behavior at finite system size. More details on this are given in Appendix D.

3.3 Long-range interacting Ising chain - Theory

Let us now consider a chain of N spin-$\frac{1}{2}$ described by the following Hamiltonian

$$H = \sum_{j=1}^{N}\sum_{r=1}^{N-j} J(r)\tau_j^x\tau_{j+r}^x + h\sum_j^N \tau_j^z, \tag{3.18}$$

with $\tau^\alpha = 2S^\alpha$ the Pauli matrices. $J(r)$ is a generic coupling depending on the relative distance r that can be short or long-ranged. The system undergoes a quantum phase transition from a ferromagnetic to a paramagnetic phase at a critical value of the transverse field that depends on the shape of the coupling $J(r)$. The non-homogeneity of the interactions breaks the permutational invariance making this class of models (unless some exceptions) non-integrable.

Fourier-transforming the spin operators $\tau_j^a = \frac{1}{N}\sum_k e^{ikj}\tau_k^a$, the Hamiltonian in Eq. (3.18) becomes

$$H = -J_0\tau_0^{x^2} - h\tau_0^z - \sum_{k\neq 0} J_k\tau_k^x\tau_{-k}^x, \tag{3.19}$$

with $J_k = \frac{1}{N}\sum_{r=1}^{N} J(r)e^{ikr}$. The zero-momentum part of the Hamiltonian in Eq. (3.19) is that of the fully connected Ising model discussed in Subsec. 3.2.1. As long as $J_k \neq 0$ the total angular momentum is not conserved. This is evident in the bosonic representation obtained by means of the Holstein-Primakoff mapping:

$$\begin{cases} \tau_k^x = \sqrt{N}\left(b_{-k}^\dagger + b_k\right) + O(1/\sqrt{N}), \\ \tau_k^y = i\sqrt{N}\left(b_k^\dagger - b_{-k}\right) + O(1/\sqrt{N}), \\ \tau_k^z = N\delta_{k,0} - 2\sum_q b_q^\dagger b_{q+k}. \end{cases} \tag{3.20}$$

Up to the quadratic order the total angular operator reads

$$\tau^2 \approx \left(N - 2\sum_{k\neq 0} b_k^\dagger b_k\right)\left(N - 2\sum_{k\neq 0} b_k^\dagger b_k + 1\right), \tag{3.21}$$

i.e. the finiteness of the interactions contribute to decrease the total angular momentum generating spin waves.

In this thesis we focus on the case of power law decaying interactions $J(r) \propto J/r^\alpha$, that are experimentally accessible in ultracold gases platforms. In what follows we describe three possible experimental setups to realize the Hamiltonian in Eq. (3.18).

3.4 Long-range interacting Ising chain – Experiments

The recent progresses in the cold atoms techniques has given the access to many different platform to simulate the dynamics of quantum spin models. In what follows we present three of the most promising platforms that have been used in the last years.

3.4.1 Rydberg atoms

Arrays of Rydberg atoms [87, 138, 139] are one of the most promising solution to simulate quantum spin chains. Rydberg atoms have a very large principal quantum number n. The basic idea is to trap these atoms with of optical microtraps with arbitrary geometry and to dress them with tunable laser that couples the ground state $|g\rangle$ to a selected Rydberg state $|r\rangle$. The dynamics is governed by the Ising-like Hamiltonian

$$H = \sum_i \frac{\hbar\Omega}{2}\sigma_i^x + \sum_{ij} V_{ij} n_i n_j, \tag{3.22}$$

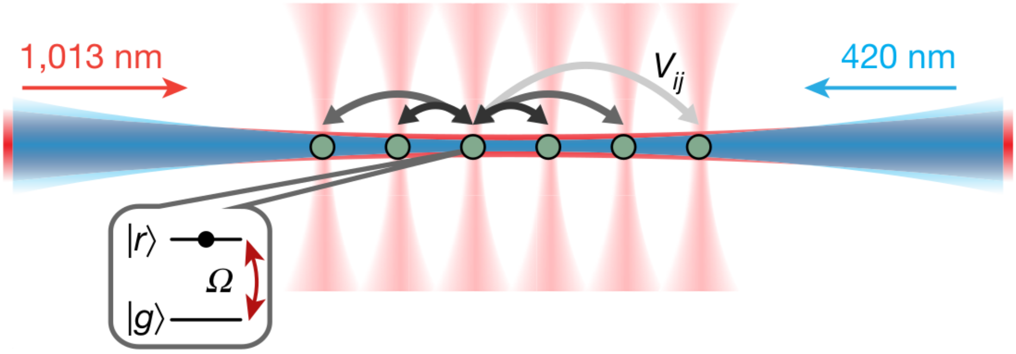

Figure 3.6: Schematic representation of the experimental setup with interacting Rydberg atom arrays from Ref. [**rydberg:1**]

with Ω Rabi frequency of the laser coupling, σ_i^α the Pauli matrices acting on the i-th site and $n_i = (1+\sigma_i^z)/2$. The term V_{ij} arises from the van der Waals interaction between the atom i and the atom j when they are both in the Rydberg states and scales as $V_{ij} \sim |i-j|^{-6}$. For some specific Rydberg states the coefficient of V_{ij} can be anisotropic [139]. When the interaction V_{ij} exceeds the Rabi frequency Ω, multiple Rydberg excitation are suppressed leading to the so-called Rydberg blockade. This setup allows to simulate a chain of $L \sim 50$ spins.

3.4.2 Trapped ions

Another possible setup to simulate spin Hamiltonians is that of confined ions coupled to laser beams [83, 86, 140–149]. Because of the Earnshaw's theorem[5], to trap the ions is necessary to use an electric field combined with a magnetic one or to use a time-dependent electric field. The first solution is that of the Penning traps in which a strong homogeneous axial magnetic field confines particles radially while a quadrupole electric one confines them axially. The second possibility is that of the Pauli (or radio-frequency or quadrupole ion) traps, in which the charged particles experience an average confining force generated by a time-dependent electric field. In particular, in the quadrupole geometry, the particles are surrounded by four electrodes producing alternately a confining and an anti-confining force. The switching rate between the two forces should be faster than the particle escape rate and usually is at a radio frequency giving the name to trap.

Spin states are usually encoded in two hyperfine "clock" states of $^{171}Yb^+$ ions. The ions are globally dressed along the principal axis of the transverse motion by two off-resonant laser beams with a wavevector difference δk that stimulate Raman transitions. The spin-spin interaction [86, 143] is generated by the pair of beatnote frequencies in the beam that are symmetrically detuned by a frequency μ from the resonance frequency. In the Lamb-Dicke regime this results in a coupling of the form

$$J_{ij} \sim \frac{J_0}{|i-j|^\alpha}, \tag{3.23}$$

and J_0 depends on $\mu, \delta k$ and on the Rabi frequency of the laser Ω. The power law exponent is generally varying in a wide range $0 \leq \alpha \leq 3$. By asymmetrically adjusting the laser beatnote detuning μ it is possible to generate and effective transverse field h to obtain an Ising-like Hamiltonian.

Depending on the geometry of the apparatus it is possible to store up to $L = 100$ ions [141]. Experiments with trapped ions have allowed the observation of dynamical quantum phase transitions in spin systems [83, 86]. Another important result is the observation of the prethermal state attained by a long-range interacting Ising chain after a sudden quench [143]. This kind of setups can also be used to follow the dynamics of the correlations varying the range of the interactions to investigate the validity of the Lieb-Robinson bound. An example of this can be observed in Fig. 3.7

---

[5] It is not possible to maintain a collection of point charges in a stable stationary equilibrium configuration solely by the electrostatic interaction of the charges

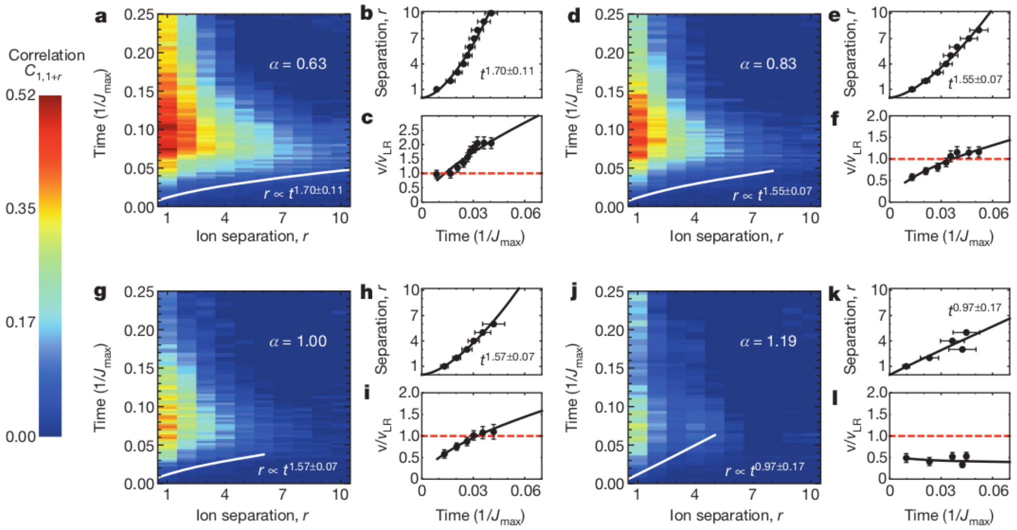

Figure 3.7: Evolution in time of the correlations between distant sites (from [142]) for different values of the power law exponent α obtained with trapped ions experiments.

(taken from Ref. [142]) that shows the evolution in time of the correlations between distant sites for different values of the power law exponent α.

3.4.3 Polar molecules

Finally, an interesting possibility to simulate more complex quantum many-body systems is to use polar molecules, molecules with a long-range anisotropic electric dipole-dipole interaction [150, 151]. The first step is to create a quantum degenerate gas of polar molecules, which is not easy to obtain because of ultralow temperatures and high phase-space densities required. A solution is that of creating heteronuclear molecules, for instance the KRb[36], starting from the quantum degenerate atomic gases and creating the ultracold molecules in the absolute rotovibrational ground state via a coherent process in two steps. First pairs of free atoms are weakly bounded via Fleshbach [152–155] resonance, then these molecules are transferred coherently to the rotovibrational ground state via STimulated Raman Adiabatic Passage (STIRAP) [156]. In the simplest cases STIRAP involves two lasers and three levels. The first laser couples the Flashbach molecule state $|f\rangle$ to a (usually lossy) excited state $|e\rangle$, the second couples this excited state to a deeply bounded state $|g\rangle$. This way the entire population is transferred from the Flashbach state to the bounded one without populating the lossy one. The molecules inherit from the nuclei the hyperfine structure and angular momentum selection rules allow to populate just one of the two creating a spin-polarized sample. The dipole-dipole interaction could be generated by dressing the molecules with electric fields. By trapping the molecules in deep optical lattices in which both tunneling and collision processes are suppressed is possible to simulate spin-1/2 Hamiltonian of the form

$$H = \frac{1}{2} \sum_{i \neq j} V_{dd}(\vec{r}_i - \vec{r}_j) \frac{J_\perp}{2} \left(S_i^+ S_j^- + S_i^- S_j^+ \right) , \tag{3.24}$$

where $V_{dd}(\vec{r}_i - \vec{r}_j) = (1 - 3\cos^2 \theta_{ij})/|\vec{r}_i - \vec{r}_j|^3$, $\vec{r}_i$ is the position of the molecule i and θ_{ij} the angle between $\vec{r}_i - \vec{r}_j$. $S_i^{+(-)}$ is the rising (lowering) spin-1/2 operator acting on the i-th site.

4

Long-range interacting Ising model – Cluster mean-field dynamics

CONTENTS

In this chapter we introduce the cluster mean-field theory (CMFT) and its application to the dynamics of the long-range interacting Ising chain. In particular, we show that the dynamics following a sudden quench can exhibit hypersensitivity to the initial conditions leading to a non trivial chaotic dynamics. Reducing the velocity of the quench the chaotic dynamics disappears and the equilibrium phase diagram is recovered. The results in this section have been derived using the open sources C++ library Armadillo [157, 158] for the linear algebra part and the Gnu Scientific Library routines for the integration of the differential equations.

4.1 Cluster mean-field theory

The cluster mean-field theory is a generalization of the mean-field theory that accounts for short-range correlations. The standard mean-field solves the exact dynamics of a single particle in the mean-field generated by the other particles, the cluster mean-field generalization, instead, solves the exact dynamics of a cluster of ℓ particles in the mean-field generated by the other identical clusters. In what follows we derive the cluster mean-field equations for spin models. Let us consider a chain of N spins with power law decaying interactions described by the Hamiltonian[1]

$$H = -\frac{J}{\mathcal{N}(\alpha)} \sum_{i\ j}^{N} \frac{\sigma_i^z \sigma_j^z}{|i-j|^\alpha} - h \sum_i \sigma_i^x, \tag{4.1}$$

with N the length of the chain and $\mathcal{N}(\alpha) = \sum_{r=1}^{N} r^{-\alpha}$ the normalization constant. The chain is divided in $N_{\mathrm{cl}} = N/\ell$ clusters of length ℓ (as shown in Fig. 4.1).

---

[1] Contrarily to what done in the previous section, we assume the coupling to be along the z direction.

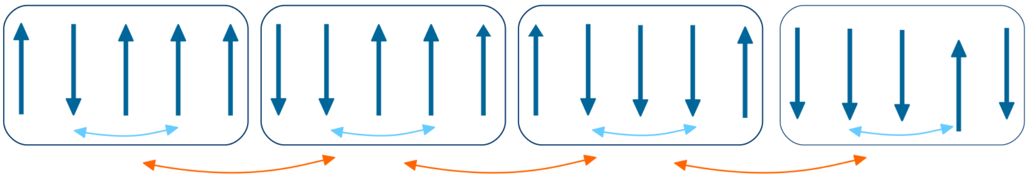

Figure 4.1: Schematic description of the cluster mean-field theory. The chain of N spins is divided into $N_{\text{cl}} = N/\ell$ clusters of length ℓ. Each cluster evolves according to the exact Hamiltonian (light-blue arrows) in the mean-field generated by the other clusters (orange arrows).

Rearranging the terms, the Hamiltonian reads

$$H = -\sum_{\beta}^{N_{\text{cl}}} \left(\sum_{i \neq j \in \beta}^{\ell} J_{ij} \sigma_i^z \sigma_j^z + h \sum_{i \in \beta}^{\ell} \sigma_i^x + \sum_{\beta' \neq \beta}^{N_{\text{cl}}} \sum_{\substack{i \in \beta \\ j \in \beta'}}^{\ell} J_{ij} \sigma_i^z \sigma_j^z \right) \tag{4.2}$$

with β and β' two cluster indices and $J_{ij} = \frac{J}{\mathcal{N}(\alpha)} \frac{1}{|i-j|^\alpha}$. The first term

$$H_{\text{cl}} = -\sum_{i \neq j \in \beta}^{\ell} J_{ij} \sigma_i^z \sigma_j^z - h \sum_{i \in \beta}^{\ell} \sigma_i^x \tag{4.3}$$

describes the dynamics inside the clusters, while the second term

$$H_{\text{out}} = -\sum_{\beta' \neq \beta}^{N_{\text{cl}}} \sum_{\substack{i \in \beta \\ j \in \beta'}}^{\ell} J_{ij} \sigma_i^z \sigma_j^z . \tag{4.4}$$

describes the dynamics among the cluster. In the cluster mean-field approach the first one is exactly solved, while the second one is rewritten posing $\sigma_i^z = m_\beta^z + \delta_i$, with $m_\beta^z = \frac{1}{\ell} \sum_{i \in \beta}^{\ell} \langle \sigma_i^z \rangle$ the mean value of the magnetization inside the cluster β and $\delta_i = \sigma_i^z - m_\beta^z$ the fluctuations around it. Substituting in H_{out} we obtain

$$\begin{aligned} H_{\text{out}} &= -\sum_{\beta' \neq \beta}^{N_{\text{cl}}} \sum_{\substack{i \in \beta \\ j \in \beta'}}^{\ell} J_{ij} \left(m_\beta^z + \delta_i \right) \left(m_{\beta'}^z + \delta_j \right) \\ &= -\sum_{\beta' \neq \beta}^{N_{\text{cl}}} \sum_{\substack{i \in \beta \\ j \in \beta'}}^{\ell} J_{ij} \left(m_\beta^z \sigma_j^z + m_{\beta'}^z \sigma_i^z - m_\beta^z m_{\beta'}^z \right) + o(\delta^2). \end{aligned} \tag{4.5}$$

Up to the first order in the fluctuations, neglecting the constant and assuming all the clusters to be equivalent (mean-field hypothesis: $m_\beta^z = m_{\beta'}^z \equiv m^z$) the Hamiltonian reduces to

$$H_{\text{out}} \sim -\frac{2m^z}{\ell} \sum_{i \in \beta} J(i) \sigma_i^z . \tag{4.6}$$

with

$$J(i) = \frac{J}{\mathcal{N}(\alpha)} \sum_{\beta' \neq \beta}^{N_{\rm cl}} \sum_{j \in \beta'}^{\ell} \frac{1}{|i-j|^\alpha} = \frac{J}{\mathcal{N}(\alpha)} \sum_{n=1}^{N_{\rm cl}-1} \sum_{j=1}^{\ell} \frac{1}{|i-(n\ell+j)|^\alpha}. \tag{4.7}$$

The cluster equivalence also implies that the mean-field coupling is independent of the site index, i.e. $j = i = \frac{\ell}{2}$, thus

$$J(i) \approx J_{\rm eff} = \frac{\ell}{\mathcal{N}(\alpha)\ \ell^\alpha} \sum_{n=1}^{N_{cl}-1} \frac{J}{n^\alpha}. \tag{4.8}$$

This way we can write the mean-field inter-cluster Hamiltonian

$$H_{\rm mf} = -\frac{2m^z J_{\rm eff}\ \sigma^z}{\ell}, \tag{4.9}$$

with $\sigma^z = \sum_i^\ell \sigma_i^z$. Intuitively, in the limit $\ell \to N$, namely one single cluster, the Hamiltonian is exact and actually $H_{\rm mf} \xrightarrow[N_{\rm cl}\to 1]{} 0$. In Fig. 4.2 we plot the behavior of the effective longitudinal field $J_{\rm eff}(\alpha) = \frac{1}{\mathcal{N}(\alpha)\ell^{\alpha-1}} \sum_{n=1}^{N_{cl}-1} \frac{J}{n^\alpha}$ as a function of the cluster size for the two different power law exponents $\alpha = 0.9$ (left panel) and $\alpha = 1.2$ (right panel) and for the three different system sizes $N = 10^6, 10^7, 10^8$. The dashed line is the numerical fit interpolating the data. It emerges that for $\alpha < 1$ in the thermodynamic limit the effective field, as expected, goes towards the mean-field value $J_{\rm eff}(0) = 1$. The closer is the power law exponent to $\alpha = 1$, the slower the effective coupling converges to the mean-field value (and the more the finite size

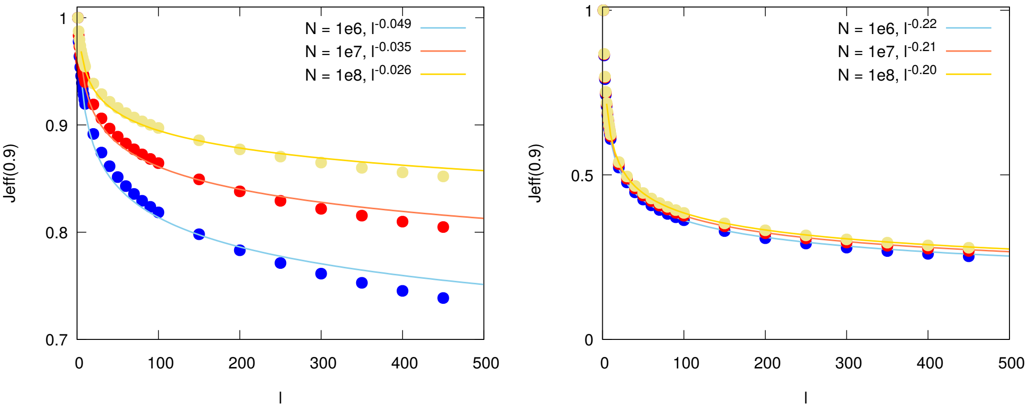

Figure 4.2: Behavior of $J_{\rm eff}(\alpha)$ as a function of the cluster size ℓ for $\alpha = 0.9$ (left panel) and $\alpha = 1.2$ (right panel) and system sizes $N = 10^6, 10^7, 10^8$. In the case $\alpha < 1$ the cluster mean-field coupling approaches in the thermodynamic limit the mean-field one, confirming the equivalence between the LMG-model and the generic case with $\alpha < 1$. As long as $\alpha > 1$ the cluster mean-field coupling approaches zero as $J_{\rm eff}(\alpha) \sim \ell^{\alpha-1}$. For $\alpha < 2$ the decreasing is sub-linear and, also for big cluster sizes, mean-field effects are present.

effects are relevant). For $\alpha > 1$, the effective coupling goes as $J_{\mathrm{eff}}(\alpha) \sim \ell^{\alpha-1}$, thus the mean-field effects are expected to disappear in the big cluster size limit. It is worth to notice that for $1 < \alpha < 2$ the mean-field coupling $J_{\mathrm{eff}}(\alpha)$ decrases with a very slow power law and even at large cluster sizes ($\ell \sim 400$) the mean-field effects are still present.

The CMFT can be used to derive the equilibrium phase diagram solving self-consistently for the ground state the cluster mean-field Hamiltonian

$$H^{\mathrm{CMFT}} = -\sum_{i \neq j \in \beta}^{\ell} J_{ij} \sigma_i^z \sigma_j^z - h \sum_{i \in \beta}^{\ell} \sigma_i^x - \frac{2m^z J_{\mathrm{eff}}\, \sigma^z}{\ell}. \tag{4.10}$$

In Fig. 4.3 we show the value of the ground-state magnetization $m^z = \frac{1}{\ell} \sum_i^{\ell} \langle \sigma_i^z \rangle$ as a function of the transverse field h and the power law exponent α for a cluster length $\ell = 5$ obtained with a precision on the ground state energy $\varepsilon = 1e - 5$. We observe that for $\alpha < 1$, with the exception of a small deviation close to $\alpha = 1$ (due to the finite cluster sizes effects discussed above) the system exhibits the mean-field transition at $h_c^{\mathrm{eq}}(\alpha = 0) = 2$ [115]. In the regime $\alpha > 1$ we observe that the quantum critical point $h_c(\alpha)$ assumes a non trivial dependence on the power law exponent. For large α, instead of recovering the nearest-neighborhood Ising quantum phase transition at $h(\alpha = \infty) = 1$, the phase transition moves toward smaller values of the transverse field to eventually disappear. This result is related to the non mean-field nature of short ranged models. In fact, as mentioned above, the mean-field Hamiltonian for $\alpha > 2$ vanishes as $H_{\mathrm{mf}} \propto 1/\ell^{\alpha-1}$ and the dynamics reduces to the exact dynamics of a ℓ spin chain.

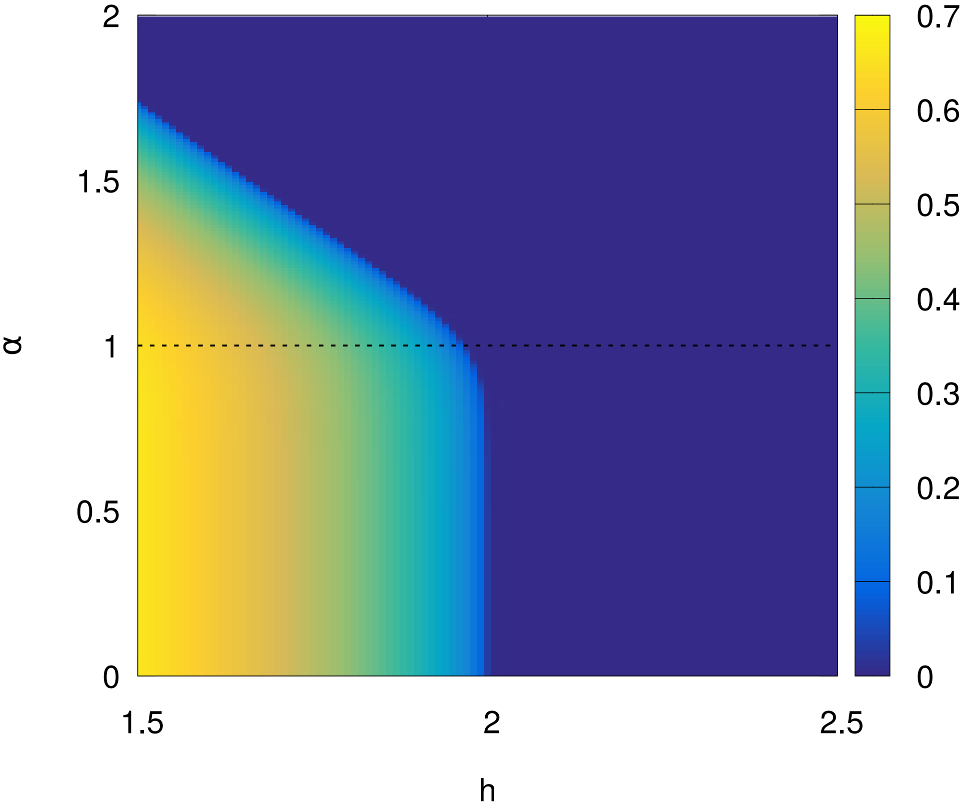

Figure 4.3: Equilibrium phase diagram for the quantum long range Ising model obtained with solving self-consistently for the ground state the cluster mean-field Hamiltonian H^{CMFT} with a cluster size $\ell = 5$ and a precision on the ground state energy $\varepsilon = 10^{-5}$. The order parameter $m^z = \frac{1}{\ell}\sum_i^\ell \langle\sigma_i^z\rangle$ (color scale) is plotted as a function of the transverse field h and the power law exponent α. A quantum phase transition from a ferromagnetic to a paramagnetic phase occurs at a critical value $h_c(\alpha)$. For $\alpha < 1$ the critical point coincides with the mean-field one, while for $\alpha > 1$ it assumes a dependence on the power law exponent. The nearest neighborhood quantum phase transition at $h_c = 1$ is not recovered because of finite size effects.

4.2 Dynamical phase diagram

Let us now analyze the post-quench dynamics of the system. The system is initially prepared in the broken phase with all spins polarized along the z axis, i.e. the $h_0 = 0$ ground state. At time $t = 0$ the transverse field h is suddenly quenched to a finite value. The dynamical order parameter we consider is the asymptotic value of the longitudinal magnetization $\overline{m}^z = \lim_{T\to\infty}\frac{1}{T}\int_0^T dt\,\langle\sigma^z(t)\rangle$, with $\sigma^z = \sum_i^\ell \sigma_i^z$. In what follows we pose $\hbar = 1$. To derive the dynamical phase diagram for the long-range Ising chain at each instant t we integrate the Schrödinger equation

$i\partial_t \left|\psi(t)\right\rangle = H\left|\psi(t)\right\rangle$, directly integrating the 2^ℓ coupled differential equations using a fourth order adaptive step[2] Runge-Kutta method.

The second term of the cluster mean-field Hamiltonian that evolves the system

$$H_{\rm mf} \equiv H_{\rm mf}(t) = -2m^z(t)J_{\rm eff}\,\sigma^z, \qquad m^z(t) = \frac{1}{\ell}\left\langle\psi(t)|\sigma^z|\psi(t)\right\rangle, \tag{4.11}$$

displays a self-consistence time-dependence due to the instantaneous averaged magnetization. Being the time dependence of the Hamiltonian self-consistent the energy

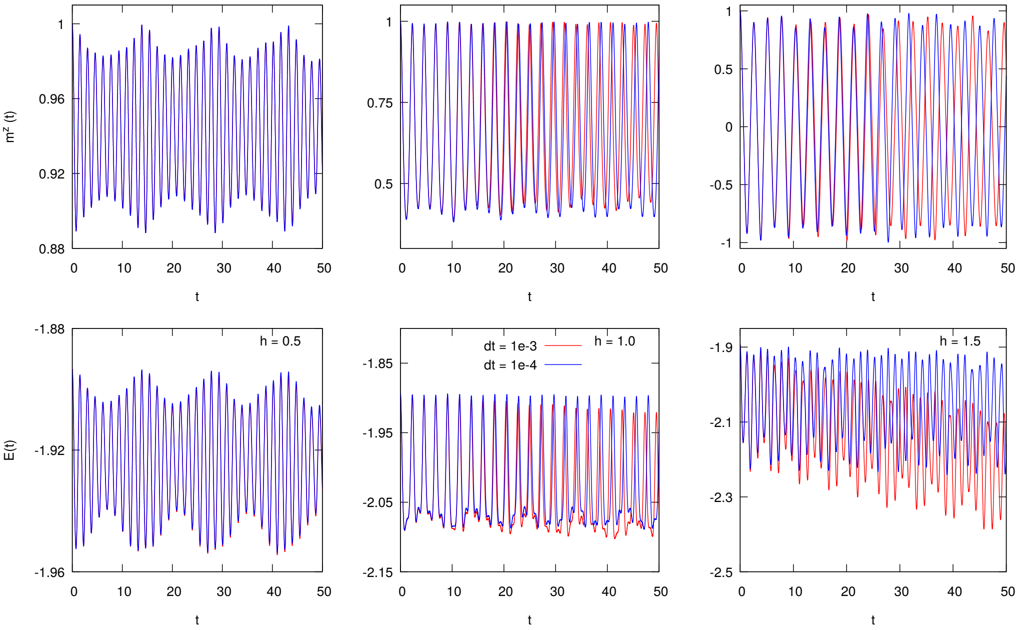

Figure 4.4: Top panels: post-quench dynamics of the dynamical order parameter as a function of time fixed $\alpha = 1.2$ and different updating times $dt = 10^{-3}$ (red lines) and $dt = 10^4$ (blue lines). The system, prepared in the ferromagnetic state, is quenched toward three final values of the transverse field (from left to right) $h = 0.5, 1.0, 1.5$, $\alpha = 1.2$. We chose $\ell = 3$. Bottom panels: the relative behavior of the energy expectation values as a function of time for the same parameters. We observe that for small updating times the expectation value of the Hamiltonian is not conserved and the mean-field approximation introduces an effective dissipation.

is in average conserved thus the system can be considered unitary. It turns out that for small updating times dt the energy is not conserved. In the top panels of Fig. 4.4 we show the behaviour of the dynamical order parameter as a function of the time for three different quenches $h = 0.5, 1.0, 1.5$ in the cases $\alpha = 1.2$ for the two different updating times $dt = 10^{-3}, 10^{-4}$ with $\ell = 3$. In the bottom panels we show the expectation values of the energy as a function of time for the same parameters. While for $dt = 10^{-4}$ the energy expectation value oscillates around an almost constant

---

[2] The algorithm attempts to determine the optimal step-size for a user-specified level of error. Further details on: https://www.gnu.org/software/gsl/doc/html/ode-initval.html

mean value, for $dt = 10^{-3}$ the mean-field approximation introduces and effective dissipation that causes the damping at long time of the order parameter.

We want to derive the dynamical phase diagram showing the dynamical order parameter as a function of the power law exponent α and the final transverse field h. For numerical reasons we have access to the dynamics only up to a finite time T (expressed in unit of J) and the order parameter $\bar{m}^z(T)$ will explicitly depends in this time. To average out the effects of the transient dynamics we evaluate the dynamical order parameter by averaging the longitudinal magnetization in a finite time window. In particular, we chose a posteriori (checking that most of the trajectories have converged at that times) to average in $t = [80, 100]^3$. The main result is the phase diagram in Fig. 4.5. It has been obtained with a cluster size $\ell = 5$,

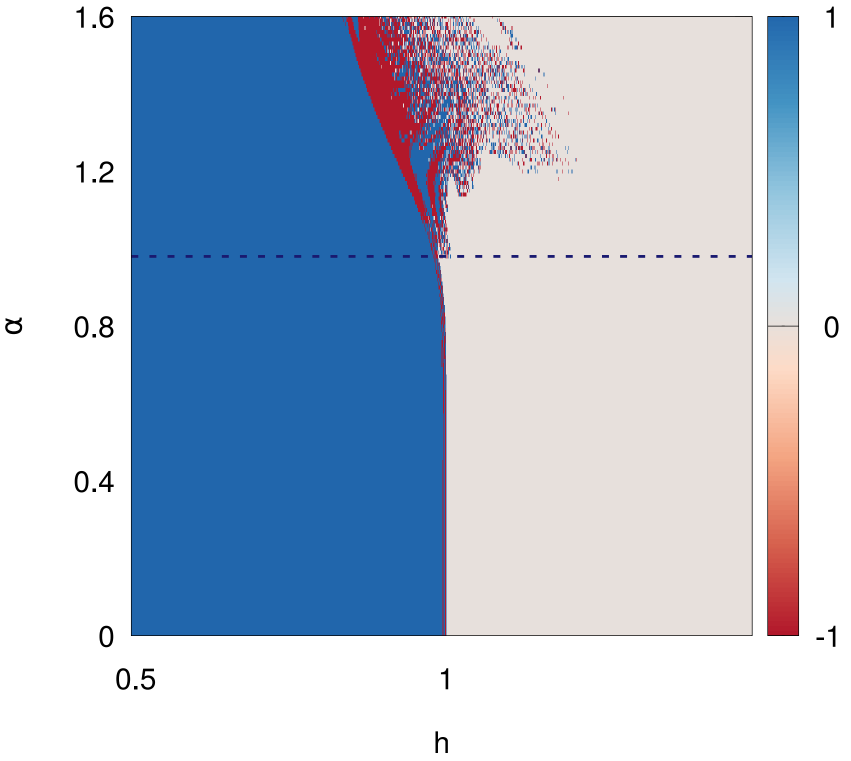

Figure 4.5: Dynamical phase diagram of the post-quench dynamics. The system, prepared in the ferromagnetic ground-state, is quenched toward a final value of the transverse field h. The figure shows the sign of the dynamical order parameter $\bar{m}^z(T)$ as a function of α and h: blue points indicate positive magnetization, red points indicate negative magnetization, white points indicate zero magnetization. The critical value $\alpha = 1$ (dashed line) divides the phase diagram in two regions: for $\alpha < 1$ the system displays the mean-field sharp phase transition, for $\alpha > 1$ the critical point spread in a critical region featuring hypersensitivity to the initial conditions.

---

[3] The convergence time strongly depends on the initial conditions (Hamiltonian parameters,

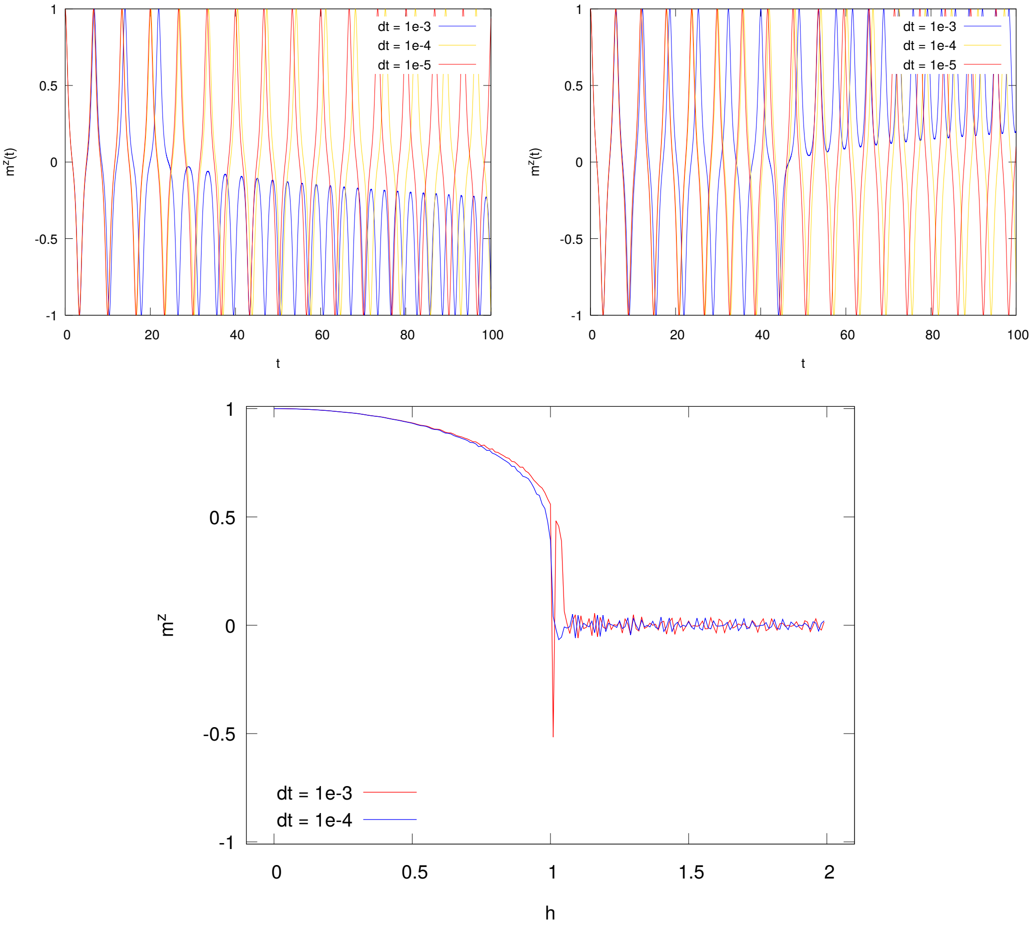

Figure 4.6: Top panels: trajectories of the longitudinal magnetization as a function of time for $\alpha = 0.0$, $h = 1.00, 1.01$, $T = 100$ and $dt = 10^{-3}$ (red line) and 10^{-4} (blue line). Bottom panel: Phase diagram for $\alpha = 0.0$. The figure shows the dynamical order parameter as a function of the final transverse field h for the two cases $dt = 10^{-3}$ (red line) and 10^{-4} (blue line). In both cases we chose an integration time $T = 100$. For small updating time the effective dissipation introduced by the mean-field approximation causes spurious ferromagnetic behaviors that disappear with an increased sensitivity.

integration time $T = 100$, updating time $dt = 10^{-3}$ and resolution $\delta\alpha = 10^{-2}$, $\delta h = 10^{-3}$. It shows the sign[4] of the dynamical order parameter $\bar{m}^z(T)$ (color map) as a function of α and of the final value of the transverse field h. The line $\alpha = 1$ (dashed line) divides the phase diagram into two different regions.

---

cluster dimension..) and it is not ensured that all the trajectories are converged in this time windows, thus this approximation introduce some noise in the final results.

[4] We are interested in the asymptotic dynamics of the systems, in particular on the sign of the magnetization. To improve the readability of the phase diagram and to reduce the transient dynamics effects, we decided to not plot the order parameter but to focus on its sign.

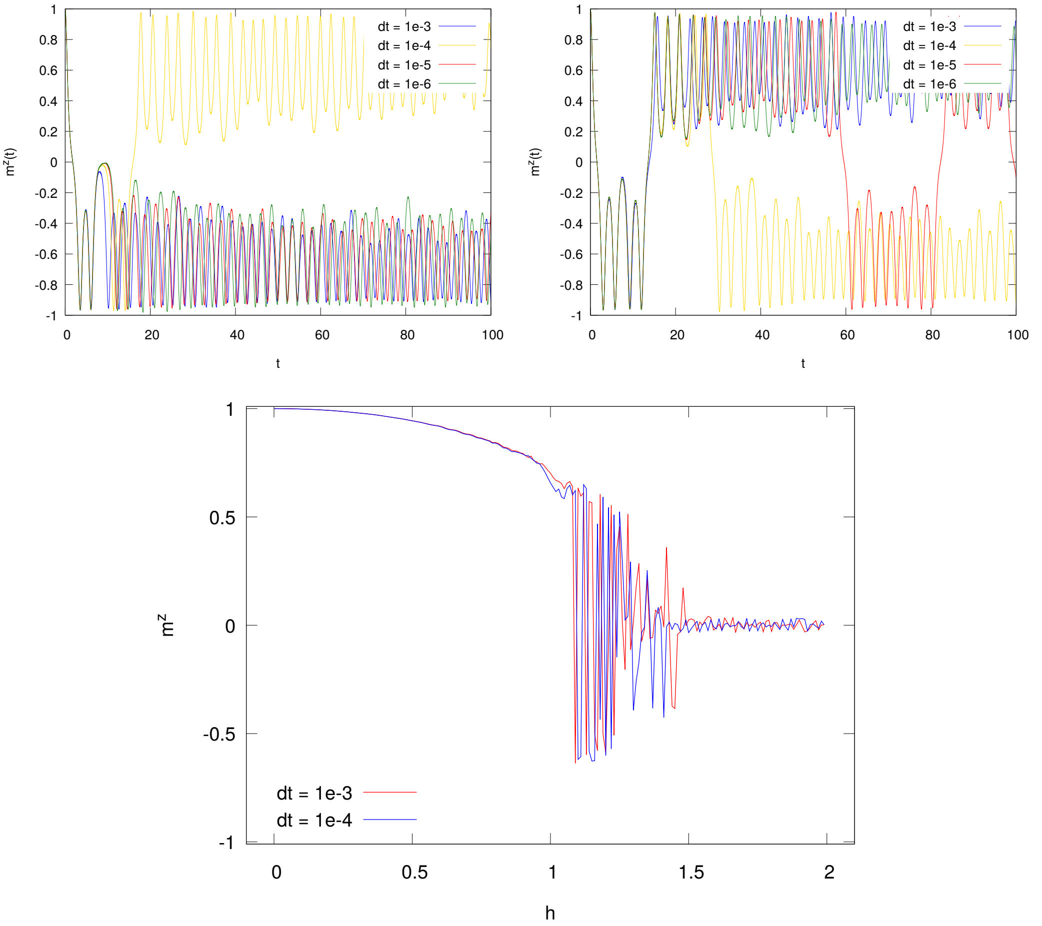

Figure 4.7: Top panels: trajectories of the longitudinal magnetization as a function of time for $\alpha = 1.2$, $h = 1.04, 1.06$, $T = 100$ and $dt = 10^{-3}, 10^{-4}, 10^{-5}, 10^{-6}$. Bottom panel: Phase diagram for $\alpha = 1.2$. The figure shows the dynamical order parameter as a function of the final transverse field h for the two cases $dt = 10^{-3}$ (red line) and 10^{-4} (blue line). In both cases we chose an integration time $T = 100$. In the case $\alpha > 1$ the ferromagnetic stationary states attained by the system survive even improving the approximation suggesting that they are not numerical noise.

For $\alpha < 1$, except for some spurious ferromagnetic (both negative and positive) points that appear very close to the dynamical critical point, we recover the mean-field sharp dynamical quantum phase transition at $h = 1$. This deviation could be understood looking at the trajectories of the order parameter as a function of time. In the top panel of Fig. 4.6 we plot the value of the longitudinal magnetization as a function of time in the case $\alpha = 0.0$ and $h = 1.00, 1.01$ for the two different values of the update time $dt = 10^{-3}$ (red line) and $dt = 10^{-4}$ (blue line). It is evident that the critical value is very sensitive to the simulation parameter and the small dissipation introduced by the mean-field approach causes the destruction of the orbit and a unphysical ferromagnetic behavior. This anomaly disappears reducing the updating time $dt = 10^{-4}$. In the bottom panel of Fig. 4.6 we plot the phase diagram (asymptotic magnetization as a function of the final transverse field) for $\alpha = 0.9$ in the two cases $dt = 10^{-3}$ (red line) and $dt = 10^{-4}$ (blue line). It is evident that in the latter approximation the mean-field quantum phase transition at $h = 1$ is recovered.

At the mean-field level ($\ell = 1$) the sharp quantum phase transition is perfectly recovered even for $\alpha > 1$. However, accounting for short-range correlations by increasing cluster size makes the dynamical critical point spread out in a dynamical critical region that exhibits hypersensitivity of the dynamical order parameter to the model details revealed by the alternation of points with positive and negative magnetization. In analogy with the work Ref. [25] we will refer to this region as the *chaotic region*. This unstable behaviour resembles the one we observed in the case $\alpha < 1$ for $dt = 10^{-3}$, but as shown in Fig. 4.7, in this case it is robust to the updating time. In the top panels of Fig. 4.7 we plot the trajectories of the longitudinal magnetization as a function of time for $\alpha = 1.2$, $h = 1.04, 1.06$ and different $dt = 10^{-3}, 10^{-4}, 10^{-5}, 10^{-6}$. We observe that there is not a well established convergence but the hypersensitivity persists even with very small update times. The same conclusion can be drawn looking at the phase diagram in the bottom panel of Fig. 4.7 that shows the hypersensitivity to be persistent for both the two different updating time $dt = 10^{-3}, 10^{-4}$. The trajectories in the top panels of Fig. 4.7 also suggest that the spurious paramagnetic points within the chaotic region in Fig. 4.5 are points that are not settle yet in a stationary state because of the finiteness of the simulation time. As we will show later, increasing either the cluster size and the simulation time the density of the spurious paramagnetic points decrease systematically.

4.2.1 Chaotic region

The dynamics within the chaotic region is extremely rich. It appears already with cluster sizes $\ell = 2$, suggesting that it is strictly connected to the presence of short-range correlations. Despite this, the form of its boundaries appears to stabilize only for larger cluster sizes ($\ell \geq 5$). The most interesting feature of the chaotic region is that moving toward the paramagnetic region, the phase diagram becomes increasingly complex analogously to what happens when we toss a coin [159]. A tossed coin that is not allowed to bounce has a trivial dynamics and the possible outcome is easily predicted just knowing the initial conditions. Conversely, if the coin is allowed to bounce the dynamics become more complicated. Depending on the number of bounces the process could exhibit hypersensitivity to the initial conditions to eventually become, in the limit of infinite bounces, purely random. In the latter case the outcome would be totally unpredictable. Strzalgo and collaborators [159] have shown that the nature of the process can be encoded in the geometry of the phase diagram in which the principal axis correspond to different initial conditions and the colors are the possible outcome (head or tail). Whenever the coin displays a trivial dynamics, the two phases (head or tail) are well separated and it always

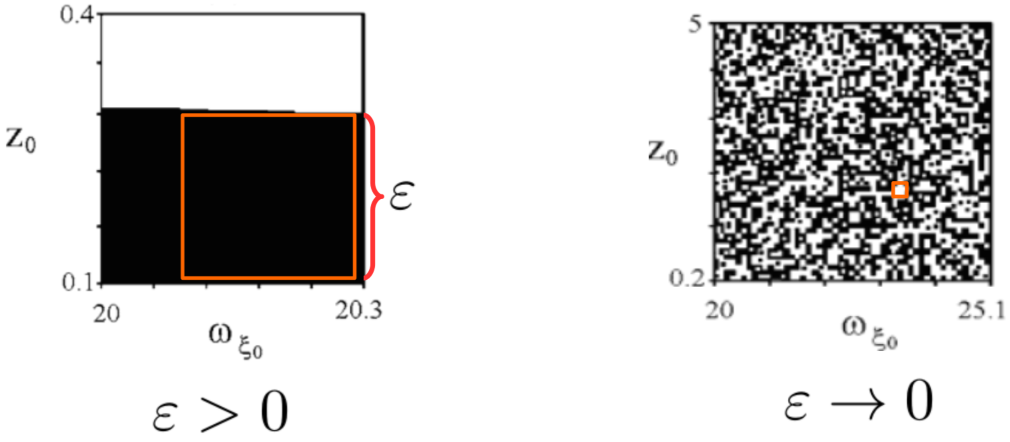

Figure 4.8: Left panel: experimental phase diagram from [159] of the tossed coin as a function of different initial conditions in the case of predictable outcome (left panel) or random process (right panel). In the first case, the two phases head (white points) and tail (black points) are well separated and it is possible to find a neighborhood of size ϵ (orange square) containing points of the same phase. Conversely, in case of a random processes, the two phases intermingle and the phase diagram fractalizes. In this case it is not possible to identify a finite neighborhood of point of the same phase and $\varepsilon \to 0$.

exists an edge between the two as shown in the left panel of Fig. 4.8. Conversely, in the chaotic regime, as shown in the right panel of Fig. 4.8, the phases intermingle and it is not possible to find a division between them. Moreover, it is possible to observe the formation of new structures leading to the *fractalization* of the phase diagram. A way to capture this feature is by defining the maximum size ε (orange square in Fig. 4.8) of the neighborhood of points of the same phase. This way, chaos is defined by the condition $\varepsilon = 0$.

At a first look, a fractalization of the phase diagram is observed also in the dynamical phase diagram in Fig. 4.5. To investigate in more details the emergence of non-trivial structures we performed simulations with higher and higher resolutions. In Fig. 4.9 we show the results obtained, from the left to the right, with $\delta\alpha = \delta h = 5 \times 10^{-3}, 10^{-3}, 5 \times 10^{-4}, 10^{-4}$, within a portion of the chaotic region defined by $1.3 < \alpha < 1.5$ and $0.9 < h < 1.1$. To be more quantitative, in the bottom panels we show the behavior of the maximum neighborhood size $\varepsilon(h)$ evaluated for a fixed value $\alpha = 1.4$ (dotted line). To make a comparison between the data with different resolutions possible, we plot the normalized quantity $\tilde{\varepsilon}(h) = \varepsilon(h)/\varepsilon_{\max}$, with $\varepsilon_{\max} = \max_h \varepsilon(h)$. As expected, it takes a maximal value in the ferromagnetic region and then shrinks to zero in the chaotic phase, independently on the resolution.

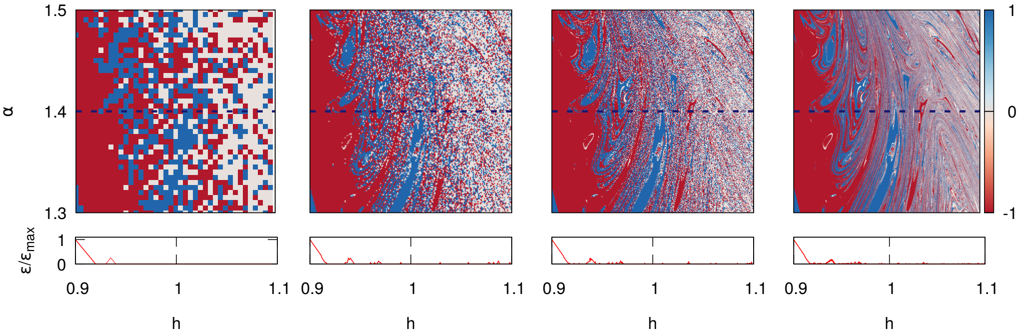

Figure 4.9: A portion of the phase diagram (blue square in Fig. 4.5) for $\ell = 5$ with increasing resolution of $\delta\alpha = \delta h = 5\mathrm{e}-3, 1\mathrm{e}-3, 5\mathrm{e}-4, 1\mathrm{e}-4$. In the critical region the phases strongly intermingle giving rise to new structures whenever the resolution is increased. Bottom panels: size of the maximum neighbourhood ε containing point of the same phase evaluated for $\alpha = 1.4$ (dotted line) as a function of the post quench transverse field h normalized to the valued $\varepsilon_{\max} = \max_h \varepsilon$. Independently on the resolution $\varepsilon/\varepsilon_{\max}$ shrinks to zero for increasing h.

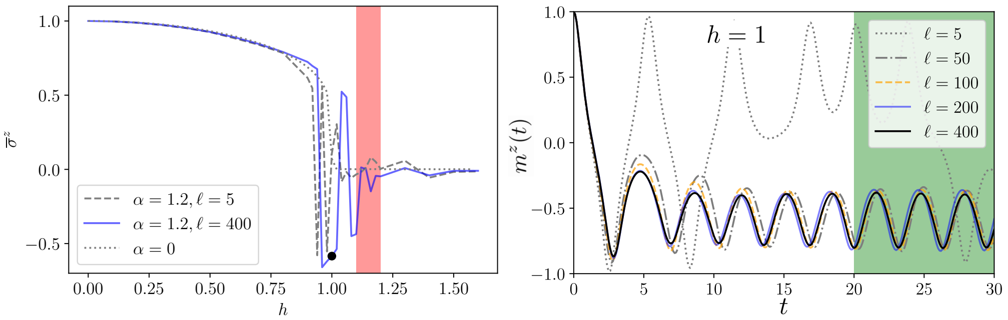

Figure 4.10: (Left panel): Dynamical phase diagram for $\alpha = 1.2$ obtained by CMFT combined with TDVP. We show the dynamical order parameter as a function of the final h. At small final fields, the dynamical order parameter is close to the mean field value (gray dashed line). Close to $h = 1$ we observe that the final magnetization becomes very sensitive to the quench parameter and alternates between positive and negative values. At large transverse fields, the dynamical order parameter vanishes. The data are obtained with the bond dimension $D = 64$. The region in red denotes the range of parameters for which convergence is attained at times longer than the one accessible by the MPS-TDVP.The order parameter is obtained by averaging over the green colored region in the left panel. (Right panel). Convergence of the time-dependent longitudinal magnetization $m^z(t)$ with the cluster size in the dynamical critical region at $\alpha = 1.2$. Relatively large system sizes (around $\ell = 200$, D $= 64$) are necessary to observe convergence.

4.2.2 Convergence

In the stable phases (ferromagnetic and paramagnetic), the fluctuations are weak and the final value of the order parameter is very close to the mean-field one, hence convergence is reached even with small cluster size. Instead, in the critical region, bigger cluster sizes are necessary to observe trajectory collapse. To investigate the convergence, we have used a Matrix Product State–Time Dependent Variational Principle (MPS-TDVP) with a second-order integrator. These results are summarized in Fig. 4.10 where we display the dynamical order parameter as a function of the transverse magnetic field h and in Fig. 4.10 where we show the convergence of a representative trajectory. The presented data are converged with bond dimension $D = 64$ and cluster size $\ell = 200$ (unless specified otherwise). We calculate the dynamical order parameter as a time average of the time-dependent longitudinal field in the time window $t = [20J, 30J]$ (significantly smaller than the one used for Fig. 4.5). Starting at small transverse fields, as expected, we observe a fast convergence of the dynamical order parameter (already at $\ell = 5$). Upon increasing the transverse magnetic field, in the vicinity of the mean field dynamical critical point, we observe a region with interchangeably positive and negative values of m^z. In this region, trajectories converge for relatively large cluster sizes $200 \leq \ell \leq 400$ (see left panel of Fig. 4.10) and are sensitive to the final magnetic field. At large transverse fields, in the paramagnetic region, we observe very fast convergence with cluster size. Although we can reliably assess a large portion of the dynamical chaotic region, a small portion close to the transition to the paramagnetic phase remains elusive. The reasons are the slower convergence with the system size and the slower relaxation to a long-lived state with a well defined dynamical order parameter. As for the phase diagram in Fig. 4.5, we expect that in this region the trajectories to become even more sensitive to the control parameter and the initial condition. As shown in Fig. 4.10 the large-cluster-size simulations ($\ell = 400$) agree well with the small-cluster-size simulations ($\ell = 5$) also very close to the dynamical chaotic region. Therefore, these data suggest that the boundaries of the dynamical chaotic region can be estimated by simulations with small cluster sizes. Also, the tendency of $\varepsilon(h)$ to decrease in the chaotic region for increasing h, discussed above for $\ell = 5$ is qualitatively observed for bigger cluster sizes as could be observed in Fig. 4.11.

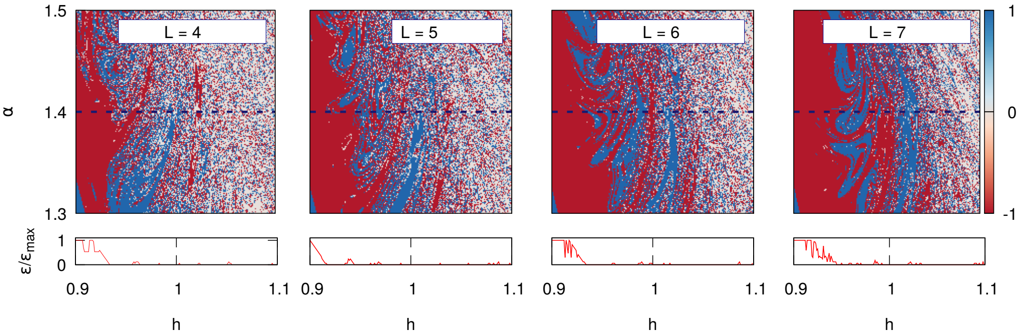

Figure 4.11: Top panels: A portion of the phase diagram for different cluster sizes (from left to right) $\ell = 4, 5, 6, 7$ with resolution of $\delta\alpha = \delta h = 10^{-3}$. Bottom panels: Relative size of the maximum neighbourhood ε containing point of the same phase evaluated for $\alpha = 1.4$ (dotted line) as a function of the post quench transverse field h normalized to the valued $\varepsilon_{\max} = \max_h \varepsilon$. Independently on the cluster size $\varepsilon/\varepsilon_{\max}$ shrinks to zero for increasing h.

Let us investigate more in depth the problem of the data convergence both with the time and the cluster size. The convergence of the cluster mean-field method is subtle. If in the stable phase it is reached with relatively small cluster in relatively small time, in the chaotic phase the convergence strongly depends on the initial conditions. First we studied the convergence with the integration time. In the left panel of Fig. 4.12 we show the phase diagram for $\alpha = 1.2$. In the left panel we plot the long-time averaged magnetization as a function of the transverse field h, in the right panel the sign of the latter for three different simulation times T: $T = 100$ (red points), $T = 200$ (yellow points), $T = 300$ (blue points). The average are evaluated in the three different time windows $t \in [80, 100], [180, 200], [280, 300]$. A good quantity to control to check the convergence is the percentage of spurious paramagnetic points in the chaotic region of the phase diagram. It emerges that in the case of the simulations with $\ell = 5$ and $T = 100$ the percentage of these white spots in the portion of the phase diagram in Fig. 4.5 with $1 < \alpha < 1.6$ and $0.8 < h < 1.2$ is the 41% of the total area. This percentage reduces to 39% increasing the simulation time up to $T = 300$. A faster decreasing can be observed increasing the cluster size, as shown in the right panel of Fig. 4.12. In this figure the percentage of the paramagnetic points is plotted as a function of the cluster length. It emerges that, as expected, this percentage reduces while increasing ℓ supporting the thesis of the total convergence in the limit of an infinite cluster.

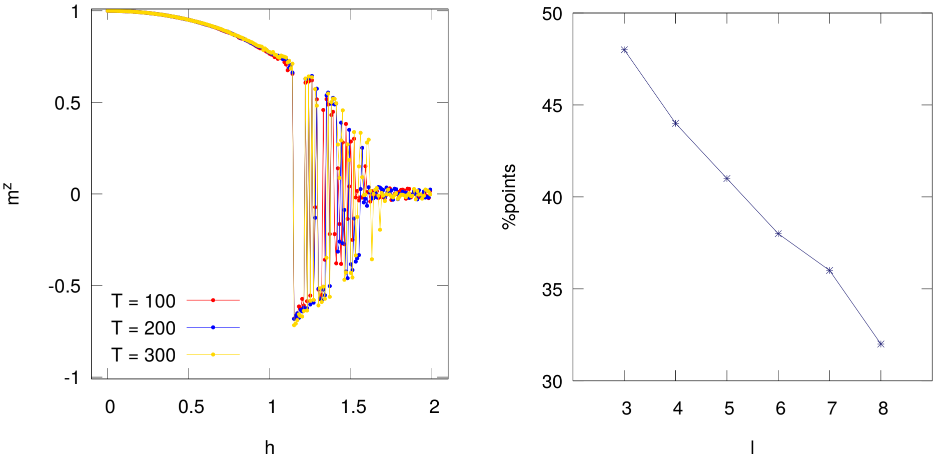

Figure 4.12: Left panel: dynamical phase diagram for $\alpha = 1.2$. We plot the dynamical order parameter as a function of the post-quench transverse field h for three different integration times $T = 100, 200, 300$ fixed $\ell = 5$. The dynamical order parameter is obtained averaging respectively in the time windows $t \in [80, 100], [180, 200], [280, 300]$. The dynamical phase diagram shows a little sensitivity to the integration time. Right panel: percentage of white point in the portion of the phase diagram delimited by $1 < \alpha < 1.6$ and $0.8 < h < 1.2$ as a function of the cluster size ℓ. Increasing the cluster size the density of paramagnetic points in the chaotic region reduces suggesting that the chaotic region is an alternation of positive and negative ferromagnetic phases.

4.2.3 Linear quench

To investigate the robustness of the chaotic region we study the post linear quench dynamics, considering the Hamiltonian with a transverse field varied according to

$$h(t) = \begin{cases} 0 & \text{if } t < 0, \\ h \tanh(\lambda t) & \text{if } t \geq 0. \end{cases} \tag{4.12}$$

The limit $\lambda \to \infty$ coincides with the sudden quench dynamics we have already described. Jaschke and collaborators [160] have shown that the physics of the Kibble-Zurek mechanism holds despite the long range interactions, thus we expect to find in the adiabatic limit $\lambda \to 0$ the same phase diagram as in Fig. 4.5. For intermediate values of the slope we expect to obtain information on the crossover between the chaotic and regular dynamics. To this purpose, we simulated the linear quench dynamics using the cluster mean field approach. As we have done for the sudden quench, the system is initially prepared in the ground state of the Hamiltonian $H_0 = -\sum_{ij} J_{ij}\sigma_i^z\sigma_j^z$, i.e. all spins polarized along the z direction, and at time $t = 0$ the transverse field $h(t) = h\tanh(\lambda t)$ is turned on.

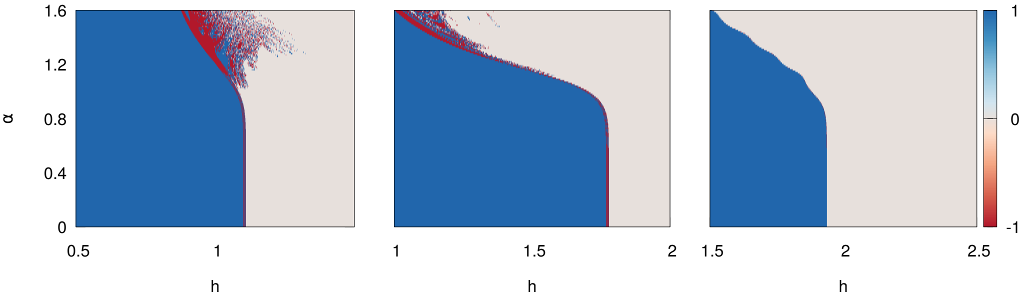

Figure 4.13: Post linear quench dynamical phase diagram. The plot shows the sign of dynamical order parameter (color scale) as a function of the power law exponent α and the final transverse field h for the different slopes $\lambda = 1, 0.5, 0.05$ (respectively from left to right). Blue points indicate positive magnetization, red points indicate negative magnetization, white points indicate zero magnetization. Three different regimes can be observed. In the left panel we observe a dynamics that is very close to the post (sudden) quench one and the chaotic behavior is still present. In the right panel we observe the limit $\lambda \to 0$ and the dynamics becomes adiabatic, in fact the equilibrium phase diagram is recovered. Finally, in the central panel we can observe an intermediate regime in which the dynamics is going towards the equilibrium despite some some reminiscent chaotic region.

The main result can be summarized in the phase diagram in Fig. 4.13 that shows the sign of $\bar{m}^z(T)$ as a function of the power law exponent α and the final transverse field $h(T)$ for three different value of $\lambda = 1, 0.5, 0.05$. The simulations have been run with $\ell = 5$ evolving the dynamics up to a time $T = 200$ with $dt = 10^{-3}$, $\delta\alpha = \delta h = 10^{-3}$. The order parameter has been evaluated averaging in the time window $t \in [180, 200]$ after the asymptotic state has been reached.

From the result in Fig. 4.13 we deduce that there are three different regimes.

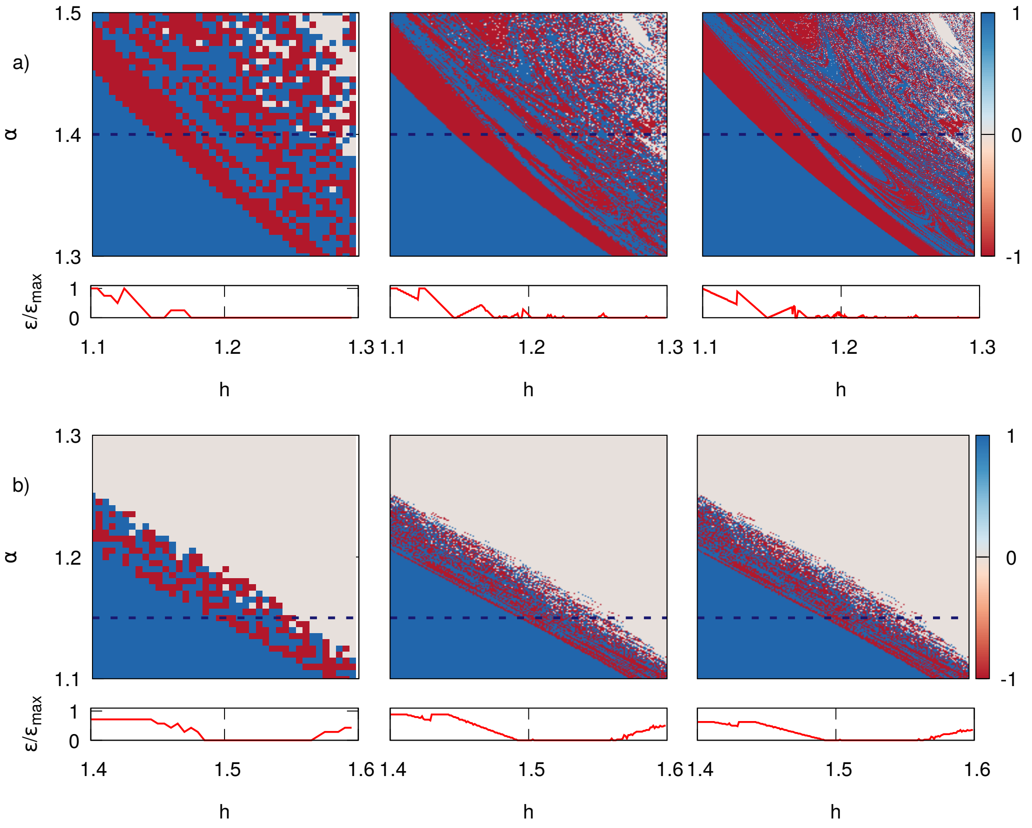

Figure 4.14: **a)** Upper panels: a portion of the phase diagram ($1.3 < \alpha < 1.5$ and $1.1 < h < 1.3$) for three different resolutions (from the left to the right: $\delta\alpha = \delta h = 5 \times 10^{-3}, 10^{-3}, 5 \times 10^{-4}$). Bottom panels: normalized neighborhood $\varepsilon(h)/\max_h \varepsilon(h)$ evaluated at $\alpha = 1.4$ (red dotted line). For these values of the power law exponent $\varepsilon \to 0$ and the system preserve the chaotic features displayed in the case of the sudden quantum quench. **b)** Upper panels: a portion of the phase diagram ($1.1 < \alpha < 1.3$ and $1.4 < h < 1.6$) for three different resolutions (from the left to the right: $\delta\alpha = \delta h = 0.005, 0.001, 0.0005$). Bottom panels: normalized neighborhood $\varepsilon(h)/\max_h \varepsilon(h)$ evaluated at $\alpha = 1.15$ (red dotted line). For this value of the power law exponent the region in which $\varepsilon \to 0$ shrinks, sign of a regularization of the dynamics.

The first (left panel) is the one of the sharp ramp in which, except for a small shift of the dynamical critical point, we recover the same dynamical phase diagram and the same chaotic features of Fig. 4.5. The second one (right panel) is the limit $\lambda \to 0$ in which the chaos is absent and the phase diagram, except for a slight shift in the critical point, starts to resemble the equilibrium one. The last regime is set for an intermediate value of the ramp slope, as could be observed in the central panel of Fig. 4.13. In this regime the system is slowly moving towards the equilibrium phase diagram but still displays a chaotic phase. From this analysis it is still not clear how the crossover between the sudden quench and the adiabatic regime occurs. However, we can carry the same fine details analysis we did for the sudden quench to study the chaotic region of the phase diagram. In the upper panels of Fig. (4.14a) we plot simulations obtained with increasing resolutions (from the left to the right: $\delta\alpha = \delta h = 0.005, 0.001, 0.0005$) of a portion of the phase diagram ($1.3 < \alpha < 1.5$ and $1.1 < h < 1.3$). In the lower panels we plot the respective normalized neighborhood $\varepsilon(h)/\max_h \varepsilon(h)$ evaluated at $\alpha = 1.4$ (red dotted line). It emerges that for these values of the power law exponent $\varepsilon \to 0$ the system preserves the chaotic features displayed in the case of the sudden quantum quench. When we move toward smaller values of α we can see that the chaotic region shrinks. This can be observed in the Fig. (4.14b) where the portion of the phase diagram with $1.1 < \alpha < 1.3$ and $1.4 < h < 1.6$ is plotted as a function of α and h. In the bottom panels the quantity $\varepsilon(h)/\max_h \varepsilon(h)$, evaluated along the line $\alpha = 1.15$, is plotted as a function of the final transverse field. It emerges that the region in which $\varepsilon \to 0$ is smaller, sign that chaos is slowly breaking down. From this analysis we can qualitatively argue that the bigger the power law exponent the more robust is chaos. Therefore, we can conclude that the crossover between the chaotic and the regular dynamics will start first from small power law exponents and will move toward the bigger ones. A quantitative analysis of this behavior can be obtained by looking at

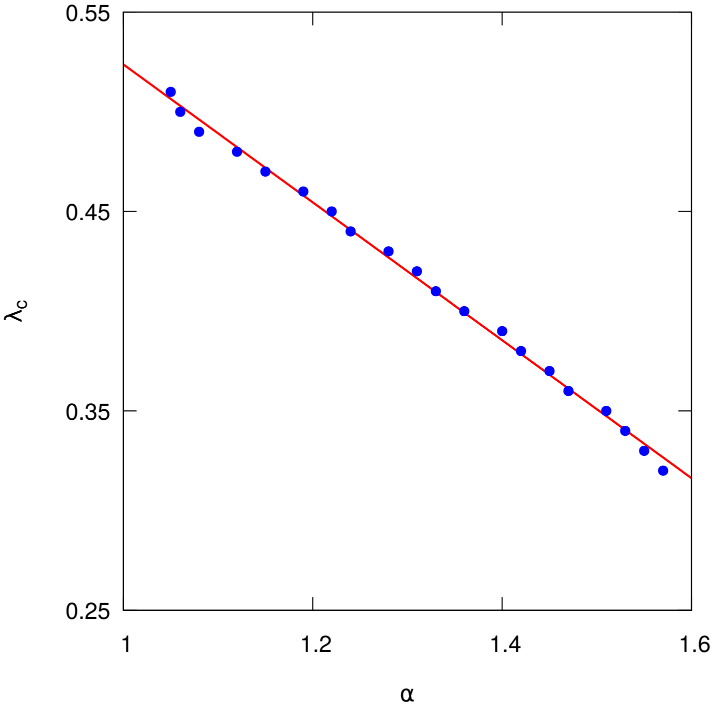

Figure 4.15: Behavior of the critical value λ_c at which the chaotic behavior disappear as a function of the power law exponent α. The blue points are the data extrapolated from the numerical results. The red line is the best fit interpolating the data. We observe a linear trend confirming the claim that the higher the power law exponent the slower the ramp should be to obtain a sharp phase transition.

the critical value λ_c of the slope, at fixed α, below which the transition is sharp. In Fig. 4.15 we plot λ_c as a function of the power law exponent. What emerges is a linear relation between λ_c and α. This result confirms the intuition that the bigger α the smoother has to be a quench in order to observe a sharp phase transition.

5

Dissipative dynamics

CONTENTS

In this chapter we extend the cluster mean-field theory introduced in Chapter 4 to the dynamics of open quantum systems with a particular focus on the dissipative dynamics of the long-range interacting Ising chain. First we derive the cluster mean-field Lindblad equations for two different dissipative processes. Then we study the dynamics of the LMG model to investigate whether the decoherence due to the external environment affects the validity of the mean-field description. Finally we reduce the range of the interactions increasing the power law exponent $\alpha > 1$. In what follows we analyze the dissipative dynamics following a quantum quench: we prepare the system in the ground state of some initial transverse field h_i and at the time $t = 0$ we quench it to a value h.

5.1 Cluster mean-field Lindblad equations

As explained in Chapter 2.2 the system is described by the evolution of the density matrix ρ in the Lindblad form

$$\dot{\rho} = -i[H, \rho] + \sum_{\lambda} \frac{\Gamma_\lambda}{2} \left(2c_\lambda^\dagger \rho c_\lambda - c_\lambda c_\lambda^\dagger \rho - \rho c_\lambda c_\lambda^\dagger \right), \tag{5.1}$$

with c_λ jump operators with associated rate Γ_λ. The cluster mean-field equations for the cluster density matrix are obtained assuming that it is a product of single cluster density matrices $\rho = \bigotimes_\beta^{N_{\rm cl}} \rho_\beta$ and tracing out all the degrees of freedom but one

$$\dot{\rho}_\beta = \partial_t \mathrm{Tr}_{\neq\beta}(\rho) = \mathrm{Tr}_{\neq\beta}\mathcal{L}(\rho) \tag{5.2}$$

In what follows we focus on the dynamics of the long-range interacting Ising chain described in Sec. 3.3

$$H = -\sum_{ij} \frac{J\sigma_i^z \sigma_j^z}{\mathcal{N}(\alpha)|i-j|^\alpha} - h \sum_i \sigma_i^x \tag{5.3}$$

with a dissipation generated by strings of Glauber operators $\sigma_s^{\pm} = \sum_i^{N_s} \sigma_i^{\pm}$ with associated rate $\Gamma_{\pm}/N_s$. In what follows we will show that the length N_s of the string of Glauber operators plays an important role in the dynamics. In particular we will show that as long as $N_s < N$, with N the system size, the system attains a stationary state with a finite or vanishing magnetization depending on the initial conditions. In the case of global dissipative processes $N_s = N$, namely jump operators acting on the whole chain, the system attains an asymptotic state characterized by persistent oscillations in time featuring a time-crystalline behavior.

The Glauber operators choose a favourite alignment (positive or negative for σ_s^+ and σ_s^- respectively) explicitly breaking the natural $\mathcal{Z}_2$ symmetry of the model. The associated master equation is

$$\dot{\rho} = -i[H,\rho] + \frac{\Gamma_+}{N_s}\left(\sigma_s^- \rho \sigma_s^+ - \frac{1}{2}\{\sigma_s^+\sigma_s^-,\rho\}\right) + \frac{\Gamma_-}{N_s}\left(\sigma_s^+ \rho \sigma_s^- - \frac{1}{2}\{\sigma_s^-\sigma_s^+,\rho\}\right). \quad (5.4)$$

The cluster mean-field equation (full derivation in Appendix F) is then

$$\begin{aligned}\dot{\rho} =&\frac{\Gamma_+}{N_s}\sum_{ij}^{\ell}\left(\sigma_i^- \rho \sigma_j^+ - \frac{1}{2}\{\sigma_i^+\sigma_j^-,\rho\}\right) + \frac{\Gamma_-}{N_s}\sum_{ij}^{\ell}\left(\sigma_i^- \rho \sigma_j^+ - \frac{1}{2}\{\sigma_i^+\sigma_j^-,\rho\}\right) \\ &+\frac{\delta\Gamma_{\text{cl}}}{N_s}\sum_i\left(\frac{\langle\sigma^+\rangle_{\text{cl}}\,[\sigma_i^-,\rho]}{2} + \frac{\langle\sigma^-\rangle_{\text{cl}}\,[\rho,\sigma_i^+]}{2}\right),\end{aligned} \quad (5.5)$$

with $\overline{\Gamma} = \Gamma_+ + \Gamma_-$ and $\delta\Gamma_{\text{cl}} = (\Gamma_+ - \Gamma_-)\,(N_s - \ell)\,\theta(N_s - \ell)$, with $\theta(x)$ the Heaviside function. The self-consistent expectation values $\langle\sigma^{\pm}\rangle = \langle\sum_i^{\ell}\sigma_i^{\pm}\rangle$ are evaluated on the cluster.

5.2 LMG Glauber dissipative dynamics

Let us derive the mean-field equations for $\alpha = 0$ (i.e. the fully connected case). First we derive the mean-field equations both for local ($N_s = 1$) and global ($N_s = N$) jump operators, then we present the cluster mean-field results for the general string operator.

5.2.1 Mean-field dynamics

Let us consider two local dissipative processes (that do not preserve the total angular momentum) associated to the local jump operators $\sigma_i^{\pm} = \sigma_i^x \pm i\sigma_i^y$ with associated rate $\gamma^{\pm}$. The Lindblad master equation reads

$$\dot{\rho} = -i[H,\rho] + \sum_{\alpha=\pm}\sum_i \gamma^{\alpha}\left(\sigma_i^{\alpha}\rho\sigma_i^{-\alpha} - \frac{1}{2}\{\sigma_i^{-\alpha}\sigma_i^{\alpha},\rho\}\right) = \dot{\rho}^u + \dot{\rho}^d. \quad (5.6)$$

The dissipative contribution to the equations of motion is given by

$$\begin{aligned}\left\langle \dot{J}^\alpha \right\rangle^d =& \frac{\overline{\gamma}}{2} \sum_i \langle [J_i^x, [J^\alpha, J_i^x]] + [J_i^y, [J^\alpha, J_i^y]] \rangle \\ &+ \frac{i\delta\gamma}{2} \sum_i \langle \{J_i^x, [J^\alpha, J_i^y]\} - \{J_i^y, [J^\alpha, J_i^x]\} \rangle \,,\end{aligned} \tag{5.7}$$

where $\overline{\gamma} = \gamma^+ + \gamma^-$ and $\delta\gamma = \gamma^+ - \gamma^-$. As a result of the anticommutation relations $\{\sigma_i^\alpha, \sigma_i^\beta\} = 0$ we finally get the equation for the normalized spin components $\alpha = \langle \sigma^\alpha \rangle / N$ with $\sigma^\alpha = \sum_i \sigma_i^\alpha$

$$\begin{aligned}\dot{X} &= 2\left(pZ^{p-1}Y - \overline{\gamma}X\right), \\ \dot{Y} &= -2\left(pZ^{p-1}X - hZ + \overline{\gamma}Y\right), \\ \dot{Z} &= -2\left(hY + 2\overline{\gamma}Z - 2\delta\gamma\right).\end{aligned} \tag{5.8}$$

The total angular momentum is not conserved thus the dynamics is not constrained on the Bloch sphere, as emerges by solving the equations of motion in terms of the spherical coordinates $R = (r\sin\theta\cos\varphi, r\sin\theta\sin\varphi, r\cos\theta)$

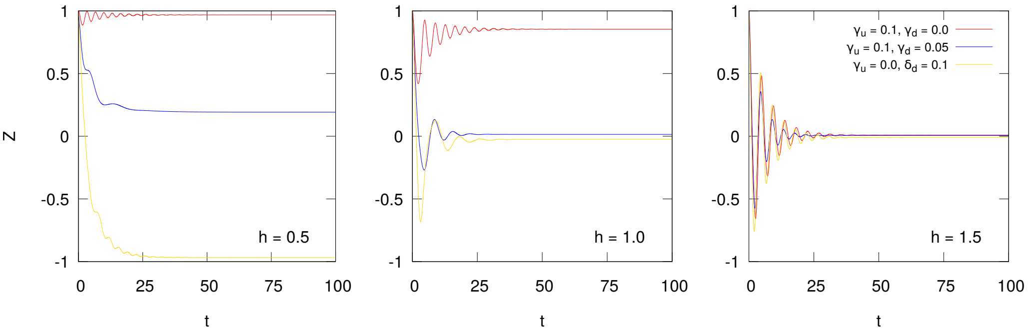

Figure 5.1: Dissipative mean-field trajectories of $Z = \langle J^z \rangle / N$ as a function of time for three different values of the post-quench transverse field (from left to right) $h = 0.5, 1.0, 1.5$ and three different combination of the jumping rate values.

$$\begin{aligned}\dot{r} &= 2r^2\overline{\gamma}(1 + \cos^2\theta) - 4r\delta\gamma\cos\theta, \\ \dot{\varphi} &= \frac{2\cos\theta(h\cos\varphi - 2r\sin\theta)}{\sin\theta}, \\ \dot{\theta} &= \frac{r\overline{\gamma}\sin 2\theta + 2rh\sin\varphi + 4\delta\gamma\sin\theta}{r}.\end{aligned} \tag{5.9}$$

There are two possible solutions of the first equation

$$r = 0, \qquad r = \frac{2\delta\gamma\cos\theta}{\overline{\gamma}(1 + \cos^2\theta)} \tag{5.10}$$

and, depending on the dissipation details, the system can either collapse on the center of the sphere or can sustain a finite magnetization. In Fig. 5.1 we show the trajectories of Z as a function of time for three different values of the final transverse field $h = 0.5, 1.0, 1.5$ and three different combination of the jumping rate values.

Let us now consider two global dissipative processes $J_\pm = \sum_i \sigma_i^\pm$ with associated jumping rate $\Gamma^\pm/N$. Since the $[J^2, J^\pm] = 0$ this dissipation preserves the total angular momentum. The Lindblad master equation is

$$\dot\rho = -i[H,\rho] + \frac{1}{2N}\sum_{\alpha=\pm}\Gamma^\alpha\left(2J^\alpha\rho J^{-\alpha} - \{J^{-\alpha}J^\alpha,\rho\}\right) = \dot\rho^u + \dot\rho^d, \tag{5.11}$$

with $\dot\rho^u$ describing the unitary evolution $\dot\rho^d$ the dissipative one. The mean-field equations of motion for the normalized spin components, up to order $o(1/N)$ reduce to

$$\begin{aligned}
\dot X^d &= \frac{i\delta\Gamma}{2N^2}\left\langle\{J_x,[J_x,J_y]\} - \{J_y,[J_x,J_x]\}\right\rangle = -\frac{\delta\Gamma}{N^2}\left\langle\{J_x,J_z\}\right\rangle\\
\dot Y^d &= \frac{i\delta\Gamma}{2N^2}\left\langle\{J_x,[J_y,J_y]\} - \{J_y,[J_y,J_x]\}\right\rangle = -\frac{\delta\Gamma}{N^2}\left\langle\{J_y,J_z\}\right\rangle\\
\dot Z^d &= \frac{i\delta\Gamma}{2N^2}\left\langle\{J_x,[J_z,J_y]\} - \{J_y,[J_z,J_x]\}\right\rangle = \frac{2\delta\Gamma}{N^2}\left\langle J_x^2 + J_y^2\right\rangle.
\end{aligned} \tag{5.12}$$

Assuming $\langle\sigma^\alpha\sigma^\beta\rangle = \langle\sigma^\alpha\rangle\langle\sigma^\beta\rangle$ the full equations are

$$\begin{aligned}
\dot X &= 2Z\left(ZY - \delta\Gamma X\right),\\
\dot Y &= -2Z\left(ZX - h + \delta\Gamma Y\right),\\
\dot Z &= -2hY + 2\delta\Gamma(X^2+Y^2).
\end{aligned} \tag{5.13}$$

with $\delta\Gamma = \Gamma^+ - \Gamma^-$.

It is possible to analytically derive the stationary states. There are four possible fixed points of the Eq. (5.13), two paramagnetic

$$P_\pm = \left(X = \pm\sqrt{1-\frac{\delta\Gamma^2}{h^2}},\quad Y = \frac{\delta\Gamma}{h},\quad Z = 0\right), \tag{5.14}$$

and two ferromagnetic

$$F_\pm = \left(X = \frac{2h}{4+\delta\Gamma^2},\quad Y = \frac{\delta\Gamma\ h}{4+\delta\Gamma^2},\quad Z = \pm\sqrt{1-\frac{h^2}{4+\delta\Gamma^2}}\right). \tag{5.15}$$

The existence of these states is subject to the constrain $|X|, |Y|, |Z| \le 1$. The last condition implies $g \le \sqrt{4+\delta\Gamma^2}$ automatically implying the other two constraints. Looking at the eigenvalues of the Jacobian $J(X,Y,Z)$ of the linear system in correspondence of the fixed points it is possible to infer the stability of the solutions

$$J(X,Y,Z) = 2\begin{pmatrix} -\delta\Gamma Z & 2Z & 2Y - \delta\Gamma X\\ -2Z & -\delta\Gamma Z & -2X + h - \delta\Gamma Y\\ 0 & -h & -2\delta\Gamma Z\end{pmatrix}. \tag{5.16}$$

The eigenvalues associated to P_+ are

$$\lambda = 0, \qquad \lambda_\pm = \pm\sqrt{h^2 - \delta\Gamma^2}\sqrt{\frac{2}{\sqrt{h^2-\delta\Gamma^2}} - 1}, \tag{5.17}$$

that are real because of the constrain $h^2 < 4 + \delta\Gamma$. Since $\lambda_- < 0 < \lambda_+$ this solution corresponds to a saddle point. Conversely, the eigenvalues associated to P_-

$$\lambda = 0, \qquad \lambda_\pm = \pm i\sqrt{h^2 - \delta\Gamma^2}\sqrt{1 + \frac{2}{\sqrt{h^2-\delta\Gamma^2}}}, \tag{5.18}$$

are purely imaginary, thus it is a marginal fixed point. In the proximity of the ferromagnetic fixed points $F_\pm$ the eigenvalues are

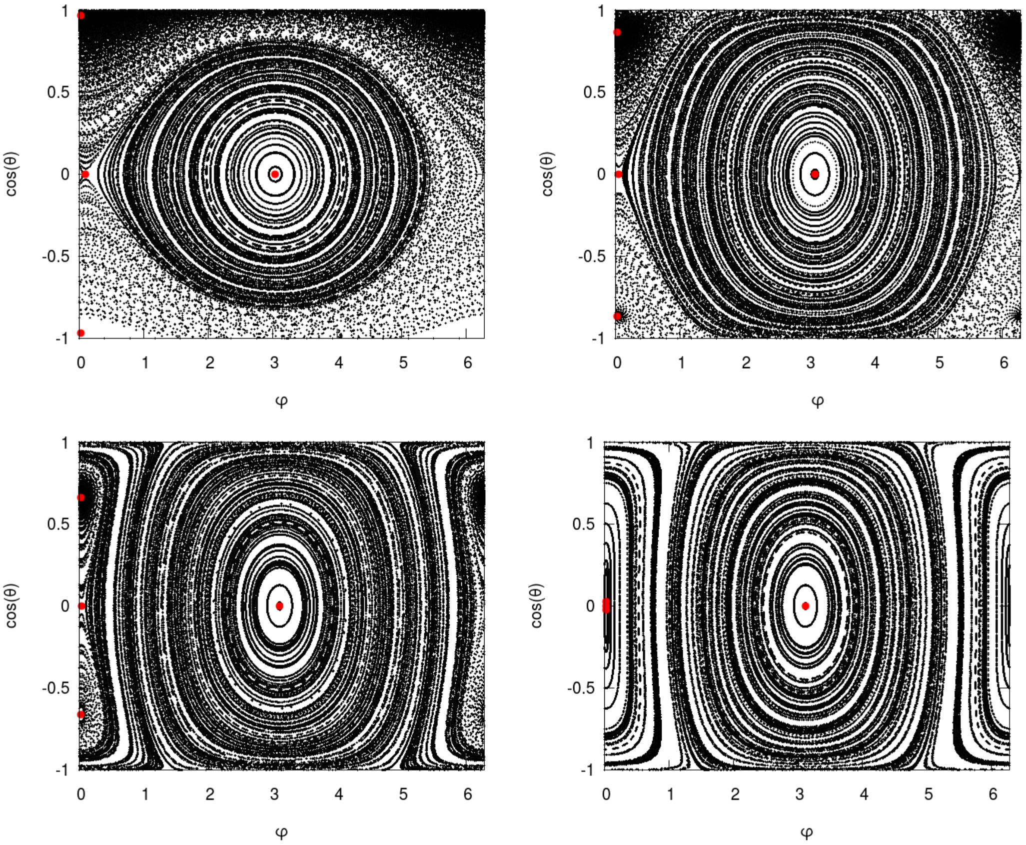

Figure 5.2: Phase portrait of the dynamical system in Eq. (5.20) for post-quench values of the transverse field $h = 0.5, 1.0, 1.5, 2.0$. The red dots are the steady states of the systems. As long as $h < 2$ the system has two ferromagnetic fixed points, one stable and one unstable, a paramagnetic saddle point and a paramagnetic marginal point that acts as generator of periodic orbits.

$$\lambda = -2\delta\Gamma, \qquad \lambda = \mp\delta\Gamma \pm 2i, \tag{5.19}$$

suggesting that the stability of the positive or negative fixed point depends on the sign of $\delta\Gamma$, according with the breaking of the $\mathcal{Z}_2$ symmetry we have discussed above. The equations in spherical coordinates read

$$
\begin{aligned}
\dot{r} &= 2r\delta\Gamma\cos\theta\left(1-\ r^2\right),\\
\dot{\varphi} &= \frac{2\cos\theta\left(h\cos\varphi-2r\sin\theta\right)}{\sin\theta},\\
\dot{\theta} &= \frac{2\left(rh\sin\varphi-\delta\Gamma\sin\theta\right)}{r}.
\end{aligned}
\tag{5.20}
$$

We observe that $r = 1$ is a solution hence the dynamics is easily visualized on the Bloch sphere. In Fig. 5.2 we show the phase portrait for four different values of the final transverse field: $g = 0.5, 1.0, 1.5, 2.0$ fixed $\Gamma^+ = 0.4$ and $\Gamma^- = 0.2$. The red dots correspond to the fixed points. Until $g < 2$ the system has a positive ferromagnetic attractor and a negative ferromagnetic repellor divided by a positive paramagnetic saddle point. The paramagnetic marginal fixed point acts as a generator of non-attractive periodic orbits dividing the phase space in two regions whose stationary state is respectively characterized by a finite or a vanishing magnetization. Crossing the critical point $h = 2$ the system does not have stable solutions anymore and always remains stacked in one of the periodic orbits. The system, thus, exhibits a driven dissipative dynamical phase transition from a dynamical symmetric to a dynamical broken phase as function of h. We can compare this value of h with the value of the transverse field at which the closed version of this system exhibits a dynamical quantum phase transition. In figure 5.3 we show the value of the critical transverse field (color map) as a function of the initial conditions both for the closed dynamics and for the driven dissipative ones. Despite the similarity between the two pictures there is no hint that there could be a correspondence between the closed dynamical phase transition and the dissipative one.

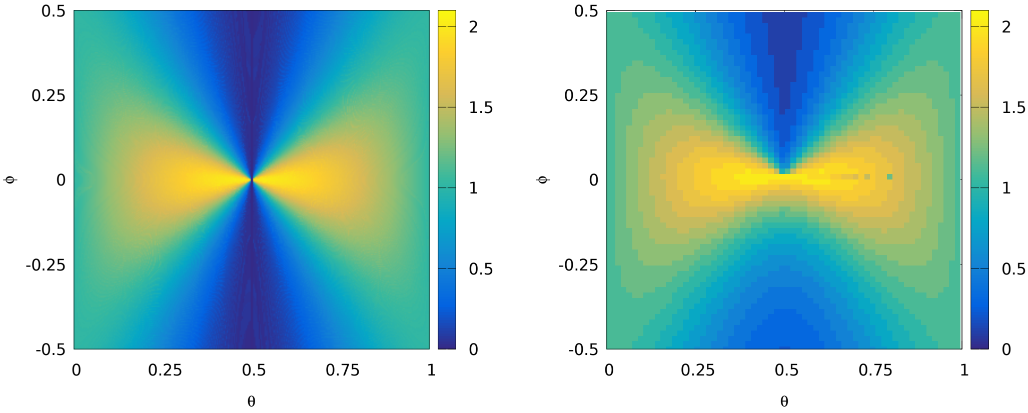

Figure 5.3: Critical value of the transverse field h (color map) at which the closed (left panel) and the dissipative (right panel) dynamical phase transition are observed as a function of the initial conditions in terms of polar and azimuthal angles.

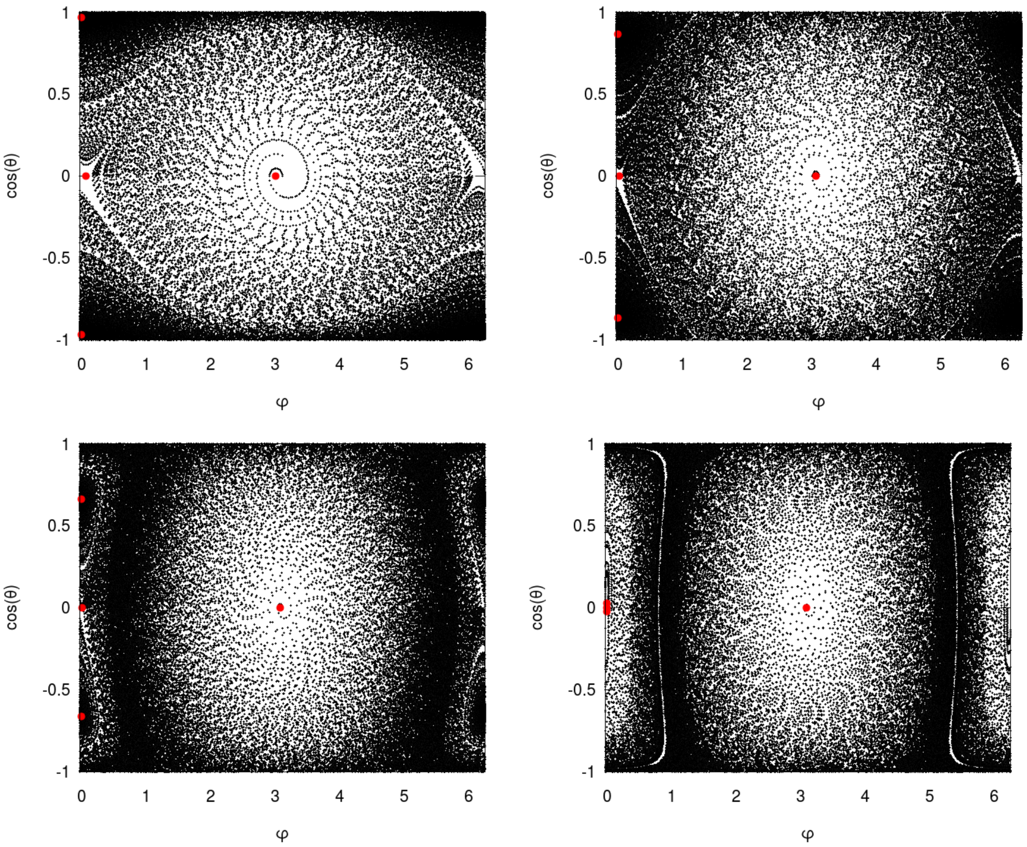

Figure 5.4: Phase portrait of the dynamical system in Eq. (5.20) for post-quench values of the transverse field $h = 0.5, 1.0, 1.5, 2.0$ in presence of a dissipation that does not explicitly break the $\mathcal{Z}_2$ symmetry. The red dots are the steady states of the systems. The two ferromagnetic fixed points are, according with the symmetry of the problem, both stable. The paramagnetic fixed points are, respectively, a saddle and a repellor and the periodic orbits have disappeared in favour of limit cycles appearing for big value of the transverse field.

The Z_2 symmetry can be restored by assuming a state-dependent rate

$$\delta\Gamma(t) = \delta\Gamma \text{sign}(z(t)). \tag{5.21}$$

As it can be seen in Fig. 5.4, where we show the phase portrait in case of symmetry preserving dissipative processes, the two ferromagnetic points are both stable. Moreover it appears a limit cycle that differs from the previous periodic orbit since it attracts the trajectories.

5.3 Cluster mean-field dynamics

The periodic orbits generated by the marginal fixed points are the boundary time-crystals described in 2.2.4, first introduced by Russomanno et al. in [39]. In [40] Riera-Campeny and collaborators have found that collective interactions are not a crucial feature for time-crystalline behavior. The presence of collective decay processes, instead, is relevant to observe subharmonic oscillations. In this section we study the stability of these time-crystals. First we investigate the validity of the mean-field approximation solving the cluster mean-field Lindblad equations in Eq. (5.5). Eq. 5.13 have been derived assuming that $\langle \sigma^\alpha \sigma^\beta \rangle = \langle \sigma^\alpha \rangle \langle \sigma^\beta \rangle$. In this approximation the conservation of the total angular momentum implies $\langle \sigma^2 \rangle = \langle \sigma \rangle^2$,

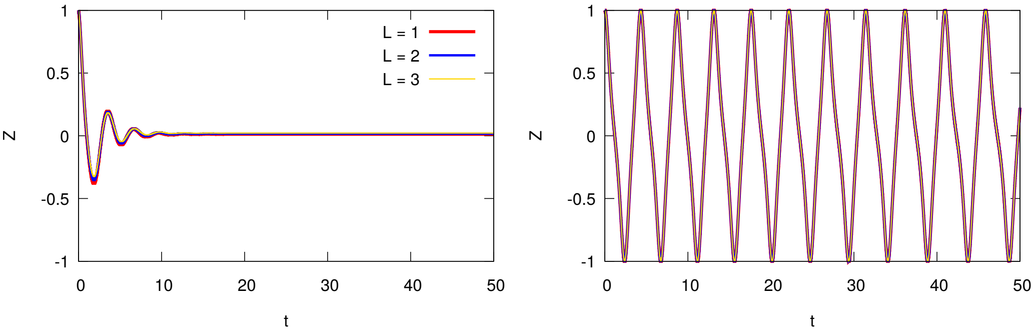

Figure 5.5: Dissipative cluster mean-field trajectories of $Z = \langle J^z \rangle / N$ as a function of time for three different values of the cluster size $\ell = 1, 2, 3$ fixed $\alpha = 0$. We simulated the dissipative dynamics in presence of local (left panel) and global (right panel) jumping operators. The post-quench transverse field is $h = 1.1$, the jumping rates are in both cases $\Gamma^+ = 0.4, \Gamma^- = 0.2$.

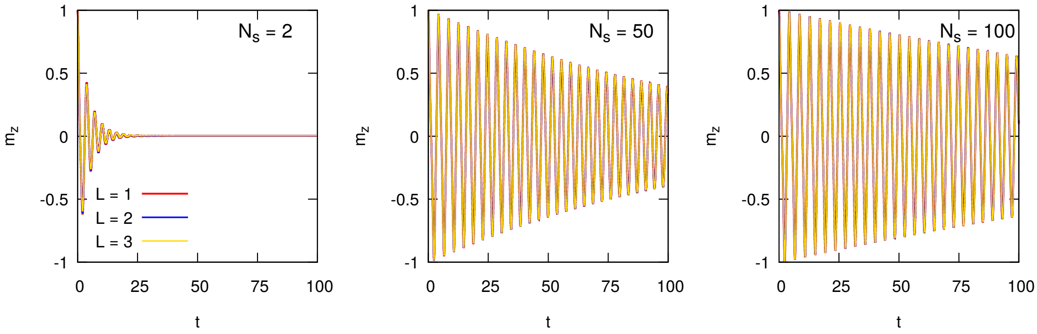

Figure 5.6: Dissipative cluster mean-field trajectories of $Z = \langle J^z \rangle / N$ as a function of time for three different values of the cluster size $\ell = 1, 2, 3$ fixed $\alpha = 0$. We simulated the dissipative dynamics in presence of string Glauber operators involving (from left to right) $N_s = 2, 50, 100$ sites. The post-quench transverse field is $h = 1.1$, the jumping rates are in both cases $\Gamma^+ = 0.4, \Gamma^- = 0.2$. Sistema label

enforcing the trajectories on the surface of the Bloch sphere. In collective models with a unitary dynamics this approximation is exact and the trajectories are insensitive to the cluster size. Local dissipative processes do not introduce the correlations among spins and the mean-field is expected to be exact. Despite this, it is not obvious whether, in presence of global dissipative processes, mean-field is still valid. We simulated the dynamics of the LMG model in presence of dissipation using the cluster mean-field theory for three different cluster sizes $\ell = 1, 2, 3$. We prepare the system in the ground state of the Hamiltonian with $h_0 = 0$ and at time $t = 0$ we quench to a final value $h = 1.10$. In Fig. 5.5 we show the trajectories of the normalized Z component of the magnetization as a function of time in presence of local (left panel) and global (right panel) dissipation fixed $\Gamma^+ = 0.4, \Gamma^- = 0.2$. As expected, the local dissipation is exactly mean-field. The three trajectories overlap also in presence of global dissipation, suggesting that the dynamics is insensitive to the short range correlations.

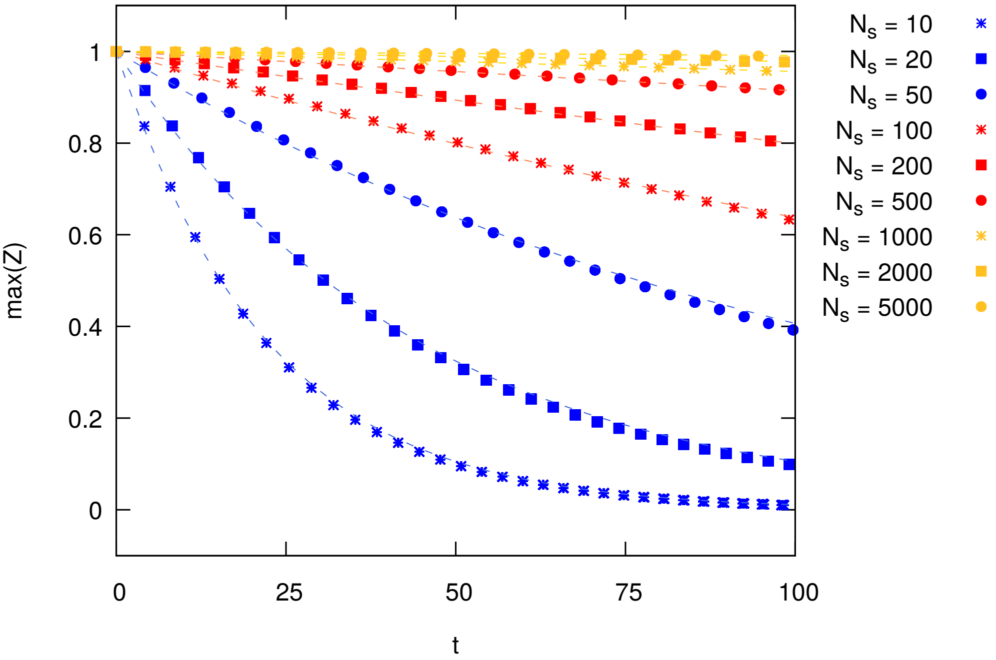

Figure 5.7: Maximum values (per period) of the mean-field trajectory of the normalized component $Z(t)$ in presence of dissipative processes generated by string of Glauber operators with different N_s. The dots are the numerical data extrapolated from Fig. 5.6, while the dashed lines are the numerical fit $f(t) = \exp(-0.45\, t/N_s)$.

We can investigate whether the time crystals in collective models survive to a finite string operators with $N_s < N$. To this purpose we simulated the post-quench dynamics described above in presence of three different dissipative processes characterized by different string lengths. In Fig. 5.6 we show the trajectories for $N_s = 2, 50, 100$ and three different cluster sizes $\ell = 1, 2, 3$. The first trivial observation is that the dynamics is insensitive to the cluster sizes confirming the mean-field nature of the model. More interestingly, increasing the string size N_s, some damped oscillations appear. We observe that the strength of the damping reduces increasing N_s. This can be quantified by looking at the behavior in time of the maximum values (per period) of $Z(t)$ for different N_site. In Fig. 5.7 we plot $\max(Z(t))$ as a function of time for increasing values of N_string. The red dots are the numerical data, the dashed lines are the numerical fit $f(t) = \exp\left(-0.45\ t/N_\mathrm{s}\right)$. We observe that in the limit of global dissipation processes $N_\mathrm{s} \to N$ the damping is infinitely slow and the oscillations persist in time. This result confirms the intuition by Riera-Campeny and collaborators [40] that global dissipation processes are a key ingredient to observe the boundary time crystal described in [39].

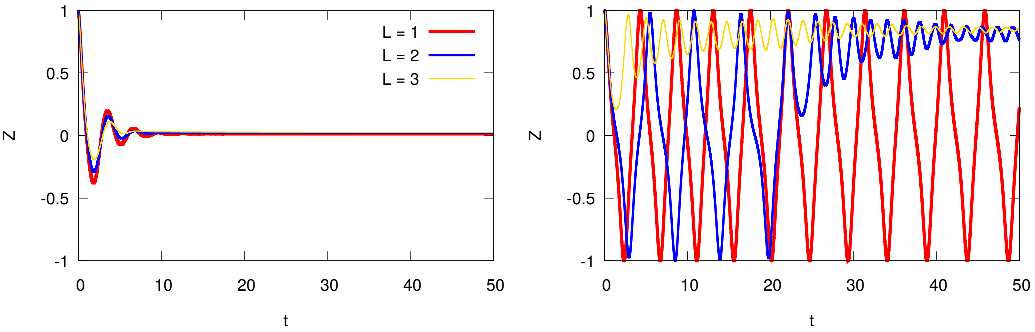

Figure 5.8: Dissipative cluster mean-field trajectories of $Z = \langle J^z \rangle / N$ as a function of time for three different values of the cluster size $\ell = 1, 2, 3$ fixed $\alpha = 1.2$. We simulated the dissipative dynamics in presence of local (left panel) and global (right panel) jumping operators. The post-quench transverse field is $h = 1.1$, the jumping rates are in both cases $\Gamma^+ = 0.4,\ \Gamma^- = 0.2$. We observe that the time-crystalline structure can not survive in presence of short range interactions.

Finally, we can investigate how this scenario changes increasing the power law exponent α. As discussed in Chapter 3.3, in the thermodynamic limit, for $\alpha < 1$ the system is expected to exhibit the mean-field dynamics and, actually, the trajectories at $\alpha = 0.5$ overlap with that at $\alpha = 0$. A more interesting behavior can be observed for $\alpha > 1.2$. In this case, in fact, the introduction of short range correlations can dramatically affect the dynamics depending on N_s. We simulated the same dynamics of Fig. 5.5 with $\alpha = 1.2$. The results are summarized in Fig. 5.8. We observe that in presence of local dissipations the finite range of the interactions does not affect the dynamics and the spin collapses at the center of the Bloch sphere. In case of global dissipation at the mean-field level $\ell = 1$ the boundary time crystal survives. As soon as the cluster size is increased the quantum fluctuations destroy the time order and the dynamics collapses toward a ferromagnetic fixed point. The same fate is reserved to operators with N_s as shown in Fig. 5.9. It emerges that for $\alpha > 1$ time order can not be sustained for any N_s, in fact, increasing the cluster size, the oscillations damp and the system reaches a stationary value characterized by a vanishing or finite value of the magnetization whose sign depends on the sign of $\delta\Gamma$ (inhibiting the emergence of chaotic behavior). An interesting question to answer is whether it

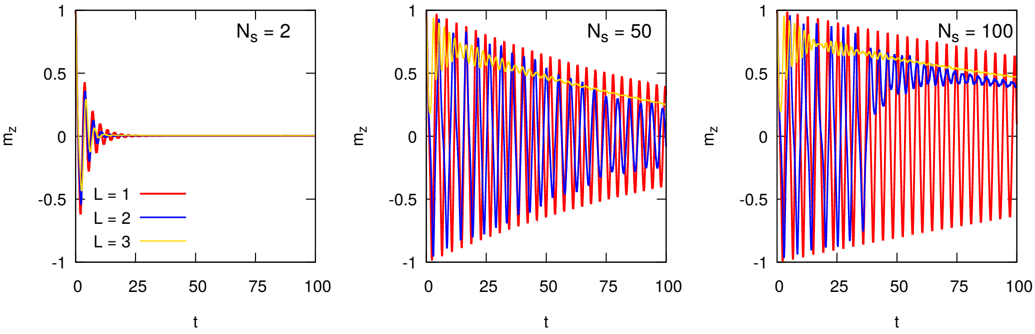

Figure 5.9: Dissipative cluster mean-field trajectories of $Z = \langle J^z \rangle / N$ as a function of time for three different values of the cluster size $\ell = 1, 2, 3$ fixed $\alpha = 1.2$. We simulated the dissipative dynamics in presence of string Glauber operators involving (from left to right) $N_{\mathrm{s}} = 2, 50, 100$ sites. The post-quench transverse field is $h = 1.1$, the jumping rates are in both cases $\Gamma^+ = 0.4, \Gamma^- = 0.2$. The system seems to reach a stationary states with a value of magnetization that is vanishing or finite depending on N_{s}.

exists a critical size $N_{\mathrm{s}}^{\mathrm{c}}$ at which the system undergoes a dynamical phase transition from a dynamical paramagnetic to a dynamical ferromagnetic phase.

6

Conclusions

In this thesis we investigated the dynamics of the long-range interacting Ising model by virtue of the cluster mean-field theory.

The general problem of the non-equilibrium dynamics of quantum many body systems has been widely investigated in the past years. In Chapter 2 we summarized the principal results of the post-quench dynamics for both isolated and open quantum systems. In the first part of this excursus we focused on the dynamics of isolated quantum many body systems and on the problem of quantum thermalization. Special attention has been dedicated to the concept of dynamical quantum phase transitions that constitutes the main argument of this thesis. A critical system prepared in the broken phase and quenched out of equilibrium can sustain long-range order at finite energy density. This is revealed by the expectation value of a dynamical order parameter that assumes a vanishing or finite value depending whether the quench is above or below a dynamical critical value. In the second part we discussed the dynamics of quantum many body systems in contact with an external bath, that is a more realistic modeling of the experimental setups. The dynamics of open quantum systems is given in terms of a master equation, usually in a Lindblad form, for the density matrix ρ. We also discussed the existence of the phase of matter that spontaneously breaks the time-translational symmetry, the so-called time crystals. A possibility to observe time crystal is as surface phenomenon in quantum many body systems connected to an external bath. Recent works [39, 40] have shown that an essential features to observe boundary time-crystalline behavior is the presence of global dissipative processes.

In this thesis we concentrated on the dynamics of long-range interacting systems. In Chapter 3 we introduced the principal properties of algebraic decaying interacting systems. A peculiar case is that of complete connected models displaying a collective dynamics. Among these, we particularly focused on the fully interacting Ising model whose collective dynamics exhibit a dynamical phase transition from a dynamical ferromagnetic phase to a dynamical paramagnetic one. The first part of the thesis is dedicated to investigate the effects on the dynamics of the fluctuation introduced reducing the range of the interactions. The main problem is related to the exponential growth of the Hilbert space that does not allow the access to the dynamics. For this reason we approach the problem by virtue of the cluster mean-field theory, a generalization of the mean-field theory that includes the short-range correlations.

In Chapter 4 we showed the post-quench dynamical phase diagram for the power-law decaying Ising chain. Depending on the power law exponent two different regimes can be identified. In the case of the truly long-range model, the system undergoes the mean-field dynamical phase transition displayed by the complete connected one. Reducing the range of the interactions the critical point spreads in a critical region exhibiting hypersensitivity to the initial conditions. This region, that we named “critical region”, shares the same physics of a tossed coin that, bouncing on the floor, displays a random dynamics with an unpredictable outcome. We elaborated on this analogy performing simulations with higher resolution and revealing the fractal structures of the phase diagram. We also investigated the stability of this chaotic phase in the case of linear quench. We found that reducing the velocity of the quench the chaotic features disappear and the system, for infinitely slow quenches, follows adiabatically the ground states.

There are still open question to answer. In particular, it would be interesting to access the long-range Ising chain dynamics to understand whether the hypersensitivity is a property of the system or is due to the non-linearity introduced by the cluster mean-field approach. Despite many experimental realizations have been proposed, chaos is expected to be incredibly sensitive to finite-sizes effects and to survive only in the thermodynamic limit. It would also be interesting to investigate different models with different symmetries to establish a possible relation between the symmetry group and the chaotic behavior.

In the second part of the thesis we consider the dynamics of the long-range interacting Ising chain in presence of Glauber dissipation processes by solving the cluster mean-field Lindblad equation. First we focused on the fully connected Ising model whose dynamics, in presence of global dissipative processes, exhibits persistent oscillations in time revealing the existence of a boundary time-crystal. In particular, we studied the stability of the boundary time-crystal performing simulations with string of N_s operators. We found that the oscillations of the order parameter decay following the exponential behavior $f(t) = \exp(-0.45\ t/N_s)$, suggesting that boundary time crystals can survive only in presence of global dissipative processes. Lastly, we simulated the dynamics reducing the range of the interactions. The preliminary results suggest that time-crystalline structures are not allowed in short ranged systems that, for any value of N_s, always reach a stationary state characterized by a finite or vanishing value of the magnetization. Future perspectives of this works are directed to the understanding of the dissipative dynamics of the long-range Ising chain. A possible interesting question regarding the characterization of the steady states is whether it exists a critical value of N_s at which the stationary states exhibits a phase transition from a ferromagnetic to a paramagnetic one. Another interesting possibility is to extend this work to different kinds of dissipative processes, for instance order parameter preserving ones, to better understand which symmetries are responsible of non-trivial dynamical behavior. Moreover, we plan to use the cluster mean-field formalism to the dynamics of the periodically driven long-range interacting Ising chain to investigate the fate of the non-trivial dynamical phase observed by Lerose and collaborators in [161].

A

Phase space formalism

In this appendix we describe the phase space formalism of the quantum mechanics, that uses the language of deterministic (classical) trajectories together with stochastic quantum jumps. In what follows we present both the coordinate-momentum representation (connected to the corpuscular or Newtonian classical limit) and the coherent state representation (connected to the wave limit). To this purpose it is important to introduce some concepts. It is defined *Weyl symbol* the one to one map between quantum operators and phase space functions. In case of hermitian operators this map is real. The Weyl symbol of the density matrix is called *Wigner function* and it could also be not positive definite, thus it referred as Wigner quasi-probability distribution. The knowledge of the Wigner function and of the Weyl symbols of various operators gives the complete description of a system. To evaluate the Weyl symbol it is possible to introduce the *Bopp operators*. Finally, the *Moyal product* defines the Weyl symbol of the product of two operators.

A.1 Coordinate-momentum representation

This is the formalism that naturally emerges from the path integral description of quantum dynamics and gives the most intuitive connection between classical and quantum realm. In this formalism the conjugate phase space operators $\hat{x}$ and $\hat{p}$ are treated symmetrically. Given a generic operator $\hat{\Omega}(\hat{x},\hat{p})$ the relative Weyl symbol is defined as follows

$$\hat{\Omega}(\hat{x},\hat{p}) \mapsto \Omega_W(\bar{x},\bar{p}) = \int d\xi\, \langle \bar{x} - \frac{\bar{\xi}}{2}|\hat{\Omega}(\hat{x},\hat{p})|\bar{x} + \frac{\bar{\xi}}{2}\rangle \exp\left(i\bar{p}\cdot\bar{\xi}/\hbar\right). \tag{A.1}$$

The vectorial notation reminds that we are dealing with a generic d-dimensional multi-particles phase space of dimension $2D$ (for a N-particles system $D = Nd$, with d dimensionality). Some simplifications could be done:

- If the operators in $\hat{\Omega}(\hat{x},\hat{p})$ is such that the coordinate operators are on the left of the momentum ones the Weyl symbol reduces to

  $$\Omega_W(\bar{x},\bar{p}) = \int \frac{d\xi d\eta}{(4\pi\hbar)^D}\Omega\left(\bar{x} - \frac{\bar{\xi}}{2}, \bar{p} + \frac{\bar{\eta}}{2}\right) \exp\left(i\bar{\eta}\cdot\bar{\xi}/2\hbar\right), \tag{A.2}$$

  with $\Omega(\bar{x},\bar{p}) = \hat{\Omega}(\hat{x} \to \bar{x}, \hat{p} \to \bar{p})$.

- If the operator $\hat{\Omega}(\hat{x},\hat{p})$ is written in the symmetrized form or is such that $\hat{\Omega}(\hat{x},\hat{p}) = A(\hat{x}) + B(\hat{p})$ the Weyl symbol is obtained with the simple substitution $\Omega(\bar{x},\bar{p}) = \hat{\Omega}(\hat{x}\to\bar{x}, \hat{p}\to\bar{p})$. To symmetrize non-symmetric operators is a goo strategy to write the Weyl symbols. For example, let us consider the operator $\hat{x}\hat{p}$

$$\hat{x}\hat{p} = \frac{\hat{x}\hat{p}+\hat{p}\hat{x}}{2} + \frac{[\hat{x},\hat{p}]}{2} = xp + \frac{i\hbar}{2}. \tag{A.3}$$

By virtue of the definition above, the Wigner function is shortly given

$$W(\bar{x},\bar{p}) = \int d\xi \, \langle \bar{x} - \frac{\bar{\xi}}{2}|\rho|\bar{x}+\frac{\bar{\xi}}{2}\rangle \exp\left(i\bar{p}\cdot\bar{\xi}/\hbar\right) \equiv \int d\xi \rho\left(\bar{x}-\frac{\bar{\xi}}{2}, \bar{x}+\frac{\bar{\xi}}{2}\right)\exp\left(i\bar{p}\cdot\bar{\xi}/\hbar\right). \tag{A.4}$$

The knowledge of the Wigner function gives access to the expectation values of a generic operator

$$\langle\hat{\Omega}(\hat{x},\hat{p})\rangle = \iint \frac{d\bar{x}d\bar{p}}{(2\pi\hbar)^D} W(\bar{x},\bar{p})\Omega_W(\bar{x},\bar{p}). \tag{A.5}$$

To evaluate the Weyl symbol is useful to introduce the *Bopp operators*, pseudo-differential operators that allow to map the quantum operators on the relative Weyl simbols:

$$\hat{x} = \bar{x} + \frac{i\hbar}{2}\frac{\overrightarrow{\partial}}{\partial p}, \quad \hat{p} = \bar{p} - \frac{i\hbar}{2}\frac{\overrightarrow{\partial}}{\partial x}, \tag{A.6}$$

that are equivalent (it can be seen integrated by part) to

$$\hat{x} = \bar{x} - \frac{i\hbar}{2}\frac{\overleftarrow{\partial}}{\partial p}, \quad \hat{p} = \bar{p} + \frac{i\hbar}{2}\frac{\overleftarrow{\partial}}{\partial x}. \tag{A.7}$$

Using the first definition it is possible to evaluate

$$(\hat{x}\hat{p})_W = (\hat{x}\hat{p}I) = \left(\bar{x} + \frac{i\hbar}{2}\frac{\overrightarrow{\partial}}{\partial p}\right)\left(\bar{p} - \frac{i\hbar}{2}\frac{\overrightarrow{\partial}}{\partial x}\right) = xp + \frac{i\hbar}{2}. \tag{A.8}$$

Similarly using the second definition

$$(\hat{x}\hat{p})_W = (I\hat{x}\hat{p}) = \left(\bar{x} - \frac{i\hbar}{2}\frac{\overleftarrow{\partial}}{\partial p}\right)\left(\bar{p} + \frac{i\hbar}{2}\frac{\overleftarrow{\partial}}{\partial x}\right) = xp + \frac{i\hbar}{2}. \tag{A.9}$$

The Moyal product of two operators $\hat{\Omega}_1$ and $\hat{\Omega}_2$ is defined as follows

$$(\Omega_1\Omega_2)_W(\bar{x},\bar{p}) = \Omega_{1W}(\bar{x},\bar{p})\exp\left(-i\hbar\Lambda/2\right)\Omega_{2W}(\bar{x},\bar{p}), \tag{A.10}$$

with Λ a simplectic operator defined $\Lambda = \sum_j \frac{\overleftarrow{\partial}}{\partial p_j}\frac{\overrightarrow{\partial}}{\partial x_j} - \frac{\overleftarrow{\partial}}{\partial x_j}\frac{\overrightarrow{\partial}}{\partial p_j}$. It is worth to observe that $-A\Lambda B = \{A,B\}_p$, being $\{\dots\}_p$ the Poisson brackets. From this it is possible to write the definition of the Moyal product

$$(\Omega_1\Omega_2)_W(\bar{x},\bar{p}) = \Omega_{1W}(\bar{x},\bar{p})\exp\left(i\hbar\{\dots\}/2\right)\Omega_{2W}(\bar{x},\bar{p}). \tag{A.11}$$

For example it will be

$$(\hat{x}\hat{p})_W = x \exp\left(-\frac{i\hbar}{2}\Lambda\right) p = xp - \frac{i\hbar}{2}\Lambda = xp + \frac{i\hbar}{2}. \tag{A.12}$$

The Moyal product could be used to derive the expression for the commutator of two operators

$$\begin{aligned} \hat{\Omega}_1, \hat{\Omega}_2 t &= -2i\Omega_{1W} \sin\left(\frac{\hbar}{2}\Lambda\right)\Omega_{2W} \\ &= -2i\Omega_{1W} \sin\left(\frac{\hbar}{2}\{\dots\}_p\right)\Omega_{2W} \\ &= i\hbar\{\Omega_1, \Omega_2\}_{MB}, \end{aligned} \tag{A.13}$$

and we have defined the Moyal braket

$$\{\dots\}_{MB} = \frac{2}{\hbar} \sin\left(\frac{\hbar}{2}\{\dots\}_p\right). \tag{A.14}$$

From this definition it is possible to observe that $\{\dots\}_{MB} \xrightarrow[x\to 0]{} \{\dots\}_p$ and the correspondence principle naturally arises. It is also possible to derive the expression for the evolution of any quantum operator

$$\dot{\hat{O}} = -\frac{i}{\hbar}[\hat{O}, \hat{H}] = \{O, H\}_{MB} \xrightarrow[\hbar\to 0]{} \{O, H\}_p, \tag{A.15}$$

that is the classical equation of motion.

A.2 Coherent state representation

A coherent state is by definition an eigenstate of a bosonic annihilation operator $\hat{\psi}\left|\psi\right\rangle_c = \psi\left|\psi\right\rangle_c$. The most natural coherent state is the vacuum, from this the generic coherent state can be constructed $\left|\psi\right\rangle_c = \exp\hat{\psi}\hat{\psi}^\dagger\left|0\right\rangle = \sum_n \frac{\hat{\psi}^n}{\sqrt{n!}}\left|n\right\rangle$, with $\left|n\right\rangle = \frac{\hat{\psi}^{\dagger n}}{\sqrt{n!}}\left|0\right\rangle$ the generic Fock state. The action of the creation operator on the coherent state $\hat{\psi}^\dagger\left|\psi\right\rangle_c = \partial_\psi\left|\psi\right\rangle_c$ resembles the conjugate structure in the coordinates-momentum representations. Despite this, the set of coherent states are not orthogonal nor normalized (${}_c\left\langle\psi|\psi\right\rangle_c = \exp\psi^*\psi$), thus they form an over-complete basis

$$I = \int d\psi d\psi^* e^{-|\psi|^2}\left|\psi\right\rangle_c {}_c\left\langle\psi\right|. \tag{A.16}$$

It is possible to shortly generalize all the concepts given in the previous subsection. The Weyl symbol of the operators

$$\Omega_W(\bar{\psi}, \bar{\psi}^*) = \frac{1}{\mathcal{N}} \iint d\bar{\eta} d\bar{\eta}^* \left\langle\bar{\psi} - \frac{\bar{\eta}}{2}\right|\Omega(\hat{\psi}, \hat{\psi}^\dagger)\left|\bar{\psi} + \frac{\bar{\eta}}{2}\right\rangle e^{-|\bar{\psi}|^2 - \frac{|\bar{\eta}|^2}{4}} e^{1/2(\bar{\eta}^*\bar{\psi} - \bar{\eta}\bar{\psi}^*)}, \tag{A.17}$$

with $\mathcal{N}$ Hilbert space dimension. The $\bar{\psi} = \{\psi_j\}$ are the complex amplitudes corresponding to single-particle eigenstates. The subscripts j could denote coordinates, momenta, different internal spin states, etc. Analogously to the previous case, in case of symmetrically ordered operators the Weyl symbol is obtained by substitution $\Omega_W(\bar{\psi}, \bar{\psi}^*) = \hat{\Omega}(\hat{\psi} \mapsto \bar{\psi}, \hat{\psi}^\dagger \mapsto \bar{\psi}^*)$. In case of normally ordered operators it would be

$$\Omega_W(\bar{\psi}, \bar{\psi}^*) = \frac{1}{\mathcal{N}} \iint d\bar{\eta} d\bar{\eta}^* \Omega \left(\bar{\psi}^* - \frac{\bar{\eta}^*}{2}, \bar{\psi} + \frac{\bar{\eta}}{2} \right) e^{|\eta|^2/2} \tag{A.18}$$

The Wigner function is simply given by definition

$$W(\bar{\psi}, \bar{\psi}^*) = \frac{1}{\mathcal{N}} \iint d\bar{\eta} d\bar{\eta}^* \, \langle \bar{\psi} - \frac{\bar{\eta}}{2} | \hat{\rho} | \bar{\psi} + \frac{\bar{\eta}}{2} \rangle \, e^{-|\bar{\psi}|^2 - \frac{|\bar{\eta}|^2}{4}} e^{1/2(\bar{\eta}^* \bar{\psi} - \bar{\eta} \bar{\psi}^*)}, \tag{A.19}$$

and it holds that

$$\langle \hat{\Omega}(\hat{\psi}, \hat{\psi}^\dagger) \rangle = \iint d\bar{\psi} d\bar{\psi}^* W(\bar{\psi}, \bar{\psi}^*) \Omega_W(\bar{\psi}, \bar{\psi}^*). \tag{A.20}$$

The Bopp operators could be generalized as follows

$$\hat{\psi}_j = \psi_j + \frac{1}{2} \frac{\overrightarrow{\partial}}{\partial \psi_j^*} = \psi_j - \frac{1}{2} \frac{\overleftarrow{\partial}}{\partial \psi_j^*}, \quad \hat{\psi}^\dagger = \psi_j^* - \frac{1}{2} \frac{\overrightarrow{\partial}}{\partial \psi_j} = \psi_j^* + \frac{1}{2} \frac{\overleftarrow{\partial}}{\partial \psi_j}. \tag{A.21}$$

The Moyal product could be written as follows

$$(\Omega_1 \Omega_2)_W(\bar{\psi}, \bar{\psi}^*) = \Omega_{1W}(\bar{\psi}, \bar{\psi}^*) \exp\left(-i\hbar \Lambda_c/2\right) \Omega_{2W}(\bar{\psi}, \bar{\psi}^*), \tag{A.22}$$

with $\Lambda_c = \sum_j \frac{\overleftarrow{\partial}}{\partial \psi_j} \frac{\overrightarrow{\partial}}{\partial \psi_j^*} - \frac{\overleftarrow{\partial}}{\partial \psi_j^*} \frac{\overrightarrow{\partial}}{\partial \psi_j}$. This defines the coherent state Poisson brakets $\{A, B\}_c = A \Lambda_c B$ such that in the limit of big occupation number it is $[\dots] \to \{\dots\}_c$. The choice of the $\hbar$ constant in the definition of the coherent brackets has been done in order to have in the wave limit the classical equation of motion $i\hbar \partial_t \psi_j = \psi_j, H_c$. Notice that in the case of bosonic systems with two body interactions this equation reduces to the Gross-Pitaevskii one. Finally we can introduce the coherent Moyle brakets by the definition of the commutator

$$[\hat{\Omega}_1 \hat{\Omega}_2]_W = 2\Omega_{1W} \sinh\left(\frac{\Lambda_c}{2}\right) \Omega_{2W} = \{\Omega_{1W}, \Omega_{2W}\}_{MBC}. \tag{A.23}$$

To conclude it is worth to underline that these two representation correspond to the dual descriptions of the phase space (corpuscular and wave) that is available only for bosonic system due to the lack of a classical counterpart of the Grassman variables needed to the coherent state description of the fermionic systems.

Some words must be spent to the spin operators case. All the discussion above could be generalized to the spin case with some caveat. Let us assume to consider a spin systems described by the collective spin variables S^α. From the algebra of the collective spin variables

$$\left[\frac{S^\alpha}{N}, \frac{S^\beta}{N} \right] = i \frac{\hbar}{N} \varepsilon_{\alpha\beta\gamma} \frac{S^\gamma}{N} = i\hbar^{\text{eff}} \varepsilon_{\alpha\beta\gamma} \frac{S^\gamma}{N}. \tag{A.24}$$

naturally emerges an effective Planck constant $\hbar^{\text{eff}} = \hbar/N$ suggesting that, in the thermodynamic limit, the system is perfectly classical and the phase space representation should work. The Bopp operators defined as follows

$$\hat{S}^{\alpha} = S^{\alpha} - \frac{i}{2} S^{\beta} \epsilon_{\alpha\beta\gamma} \frac{\partial}{\partial S^{\gamma}} \tag{A.25}$$

could be used to evaluate the Weyl symbols of the operators. To evaluate the dynamics it is needed the definition of the spin Poisson brackets

$$\{f, g\}_{Ps} = \varepsilon_{\alpha\beta\gamma} \frac{\partial f}{\partial S^{\alpha}} \frac{\partial g}{\partial S^{\beta}} S^{\gamma}. \tag{A.26}$$

This way the equation of motion for the spin variables is given, in the first approximation, to

$$\dot{S}^{\alpha} = \{H, S^{\alpha}\}_{Ps}. \tag{A.27}$$

It is important to observe that this mapping could describe the semi-classical dynamics of collective systems in the thermodynamic limit, namely it holds only in the Holstein-Primakoff validity regime when the system behaves as a collection of harmonic oscillators.

B

Spin-squeezing

In the last decades spin squeezing has attracted considerable attention, both theoretically and experimentally, due to its versatility in the applications (a full review in [162]). For example, it can be used to detect quantum entanglement, in fact Tóth and collaborators [163, 164] have proved a close relation between spin-1/2 entangled states and spin squeezed states. The relevance of this result relies in the fleetness of experimental realization and detection of spin squeezed state [165–167]. Beside this, spin squeezing is also useful for quantum computation [168, 169] and quantum simulation [170] and provides a good instrument to improve the precision of the measurements, e.g. in the Ramsey spectroscopy [171, 172] or in gravitational-wave interferometers [173].

Despite its feasibility, the definition of the spin squeezing and of the spin-squeezing parameters is not unique and depends on the contest it is considered. The definition of squeezing has been given in the contest of quantum optics [174, 175] and it is usually referred to bosonic particles. Given the bosonic operator a and $a^\dagger$ obeying the canonical commutation relations $[a, a^\dagger] = 1$, we can introduce the coordinate momentum operators given by $x = (a + a^\dagger)/2$ and $p = (a - a^\dagger)/2i$, with $[x, p] = i$ and $\hbar = 1$. The Heisenberg uncertainty relation states that $\Delta x \Delta p \geq 1/2$, with $\Delta A = \sqrt{\langle A^2 \rangle - \langle A \rangle^2}$. In literature a *coherent state* is an eigenstate $|\alpha\rangle$ of the destruction operator $a\,|\alpha\rangle = \alpha\,|\alpha\rangle$ (e.g. the vacuum state). Coherent states satisfy the relation $\Delta x = \Delta p = 1/\sqrt{2}$ thus they are also defined minimum uncertainty states. Whenever the variance on one of the two directions becomes smaller than the coherent one, the coherent state becomes squeezed. The so-called *principal quadrature squeezing* can be quantified introducing the parameter ζ_B^2. Defined a generic operator on the $x - p$ plane

$$x_\theta = e^{i\theta a^\dagger a} x e^{-i\theta a^\dagger a} = a e^{-i\theta} + a^\dagger e^{i\theta}, \tag{B.1}$$

whose special case are $x = x_0$ and $p = x_{\pi/2}$, we can introduce

$$\begin{aligned} \zeta_B^2 &= \min_{\theta \in (0, 2\pi)} (\Delta x_\theta)^2 \\ &= 1 + 2\left(\langle a^\dagger a \rangle - |\langle a \rangle|^2 - |\langle a^2 \rangle - \langle a \rangle^2|\right). \end{aligned} \tag{B.2}$$

This way, the condition $\zeta_B^2 < 1/2$ indicates bosonic principal squeezing.

The generalization of this parameter in the case of spin systems is not straightforward. Let us consider a system of N spin-1/2 interacting particles. We can introduce the angular momentum operators $J_\alpha = \frac{1}{2}\sum_l \sigma_{zl}$ that obey to the $SU(2)$ commutation relations $[J_\alpha, J_\beta] = i\varepsilon_{\alpha\beta\gamma}J_\gamma$. This results in the Heisenberg uncertainty

$$\Delta J_\alpha \Delta J_\beta \geq |\langle J_\gamma\rangle|/2. \tag{B.3}$$

We can also introduce the coherent spin states (CSS) as a direct product of single spin states

$$|\theta,\phi\rangle = \bigotimes_{l=1}^{N}\left(\cos\frac{\theta}{2}|0\rangle_l + e^{i\phi}\sin\frac{\theta}{2}|1\rangle_l\right), \tag{B.4}$$

with $\sigma_{lz}|0\rangle_l = |0\rangle_l$ and $\sigma_{lz}|1\rangle_l = -|1\rangle_l$. Another definition could be given in terms of Dicke states $|s,m\rangle$, eigenstates of S^2 and S^z with eigenvalues $s(s+1)$ and m respectively,

$$|\alpha\rangle = (1+|\alpha|^2)^{-s}\sum_{m=-s}^{s}\begin{pmatrix} 2s \\ s+m \end{pmatrix}\alpha^{s+m}|s,m\rangle\,,\ \alpha\in\mathbb{C}, \tag{B.5}$$

with $\alpha = -\tan(\theta/2)\exp(-i\varphi)$.

The spin-squeezing could be defined by analogy with the bosonic case introducing the following squeezing parameter

$$\zeta_H^2 = \frac{2\,(\Delta J_{\vec{n}_1})^2}{|\langle J_{\vec{n}_2}\rangle|} = \frac{1-(\vec{n}_0\cdot\vec{n}_1)^2}{|\vec{n}_0\cdot\vec{n}_2|}, \tag{B.6}$$

with $\vec{n}_0, \vec{n}_1, \vec{n}_2$ orthogonal unit vectors. However, this is not a desirable definition since it turns out that $\zeta_H^2 < 1$ on a CSS. This is due to the fact that, unlike the bosonic systems, the variance of a CSS is not equal in all the directions but depends on the *mean-spin direction* (MSD) $\vec{n}_0$ defined as

$$\vec{n}_0 = \frac{\langle\vec{J}\rangle}{|\langle\vec{J}\rangle|}. \tag{B.7}$$

We can define $n_\perp$ the axis perpendicular to the MSD. It can be proved that for a CSS $(\Delta_{\vec{n}_\perp})^2 = j/2$, with j eigenvalue of the total angular momentum. This way it is possible to introduce the spin squeezing parameter (not unique)

$$\xi_S^2 = \frac{\min(\Delta J_{\vec{n}_\perp}^2)}{j/2} = \frac{4\min(\Delta J_{\vec{n}_\perp}^2)}{N}. \tag{B.8}$$

This parameter is such that for the pure uncorrelated CSS $|\theta,\phi\rangle$ it is $\xi_S^2 = 1$. Whenever correlations arise in the system, namely entanglement is generated, one direction squeezes and the spin squeezing parameter reduces to $\xi_S^2 < 1$.

C

Generalization of the Dicke model

In this appendix we describe the experimental realization of non-equilibrium stationary states of the Dicke model and its possible generalization to more complex models.

C.1 NESS realization of the Dicke model

The idea behind the NESS realization of a Dicke is that a condensate of atoms (usually a Bose-Einstein condensate (BEC)), into a cavity, for some values of the coupling with the radiation field, self-organizes on a pattern where the atoms are separated by an integer multiple of the wavelength and the atom scatter light coherently if lighted with a strong enough pump. This is a pump-cavity scattering driven process: first a pump photon is virtually absorbed by an atom, this way the atom gains one photon momentum along the pump axis in the direction of the pump photon; then the photon is scattered into a cavity mode and the atom gains momentum along the cavity axis in the opposite direction of the emitted photon. This processes allow the ground state of a BEC, naturally a zero momentum state, to be excited to a finite momentum one. Depending on the relative geometry between the cavity and the pump, it is possible to realize different models. A single cavity lighted orthogonally is the prototype of a two level system interacting with the electromagnetic field. If we assume the cavity to be single mode, in an opportune time dependent frame rotating with the pump frequency, this set up is described by the Hamiltonian in Eq. (3.13). Varying the cavity-pump angle is a way to achieve different models. For example, if the single mode cavity is dressed by a pump with an angle of $2\pi/3$, the effective model is that of a three levels system interacting with a bosonic mode [176, 177]. By adding cavities it is possible to enhance the symmetries of the model, as has been done by Donner and collaborators.

C.2 Three-levels system in two optical cavities

Donner and collaborators [178] consider two optical cavities with a crossing angle of $\frac{2\pi}{3}$ sourrounding a BEC of $N = 2 \times 10^5$ ^{87}Rb atoms dressed by an external pumping that is not orthogonal with the cavities. All the atoms in the BEC start in the state

$|p=0\rangle$ and, by virtue of the pump-cavity scattering described above, can be excited to the level $|\pm\mathbf{k}_p \pm \mathbf{k}_c\rangle$ depending on the scattering direction. The reverse process is equally probable: the excited states form a pair of equal absolute momentum with opposite direction, in order to have the ground state connected with two excited states: the less energetic $\omega_- = \omega_r$ and the more energetic $\omega_+ = 3\omega_r$, being ω_r the recoil energy due to the pumping. For symmetry reasons the two eigenstate are superposition of the equal absolute momentum states:

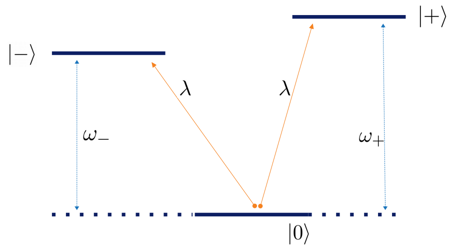

Figure C.1

$$\begin{aligned} |+\rangle &= \frac{1}{\sqrt{2}}(|+\mathbf{k}_p+\mathbf{k}_c\rangle + |-\mathbf{k}_p-\mathbf{k}_c\rangle), \\ |-\rangle &= \frac{1}{\sqrt{2}}(|-\mathbf{k}_p+\mathbf{k}_c\rangle + |+\mathbf{k}_p-\mathbf{k}_c\rangle). \end{aligned} \tag{C.1}$$

The Hamiltonian of this system is the sum of three terms $H = H_1 + H_2 + H_{12}$ with $1, 2$ cavity indices. The latter term describes the interaction among the cavities that is experimentally negligible with respect to the cavity terms. Thus, in what follows we assume $H_{12} = 0$. The cavity Hamiltonian reads

$$H_i = \Omega_i a_i^\dagger a_i + \omega_+ A^+_{+,i} + \omega_- A^-_{-,i} + \frac{\lambda_i}{\sqrt{N}}(a_i^\dagger + a_i)\left(A^0_{+,i} + A^+_{0,i} + A^0_{-,i} + A^-_{0,i}\right), \tag{C.2}$$

with $A^s_{r,i} = \sum_{j=1}^N |r_i\rangle^{(j)}\langle s_i|$, being $r_i, s_i \in \{0,+,-\}$. We also pose $\Omega_i = \omega_p - \omega_i < 0$ the detuning between resonance frequency of cavity i and pump laser frequency. In general $-\Omega_i \in [2,5]$. This Hamiltonian describes a three-level system (sketched in Fig. C.1), in which the two excited level $|+\rangle, |-\rangle$ are connected with the ground state $|0\rangle$, interacting with two ideal optical cavities.

In what follows we assume the experimental parameters $\omega_- = 2\pi \times 3.7$ kHz and $\omega_+ = 3\omega_-$ and we express all the energies in unit of the recoil frequency defined in Appendix C. By virtue of a generalized Holstein-Primakoff transformation [176, 177, 179] it is possible to map the generator $A^s_{r,i}$ of the group $U(N_\ell)$, with N_ℓ the number of levels, onto a combination of creation and annihilation operators $b_r^\dagger, b_r$ of $N_\ell - 1$ Holstein-Primakoff bosons, fulfilling the canonical commutator relations.

Given a reference level m the map is

$$\left.\begin{aligned} A_r^s &= b_{r,i}^\dagger b_{s,i} \\ A_r^m &= b_{r,i}^\dagger \Theta_{m,i}(N) \\ A_m^s &= \Theta_{m,i}(N) b_{s,i} \\ A_m^m &= \Theta_{m,i}(N)^2, \end{aligned}\right\} r, s \neq m, \tag{C.3}$$

with $\Theta_{m,i}(N) = \sqrt{N - \sum_{r\neq m} b_{r,i}^\dagger b_{r,i}}$, $\langle b_{r,i}^\dagger b_{r,i}\rangle \leq N$ and $\sum_{r\neq m}\langle b_{r,i}^\dagger b_{r,i}\rangle \leq N$. Posing $m = 0$ the Hamiltonian becomes

$$H = \sum_{i=1,2}\left[\Omega_i a_i^\dagger a_i + \omega_+ b_{i+}^\dagger b_{i+} + \omega_{i-} b_{i-}^\dagger b_{i-} + \frac{\lambda_i}{\sqrt{N}}\left(a_i^\dagger + a_i\right)\left(b_{+i}^\dagger \Theta_0(N) + b_{i-}^\dagger \Theta_0(N) + h.c.\right)\right] \tag{C.4}$$

This model has a $\mathcal{Z}_2$ symmetry generated by the operator $C = a_i^\dagger a_i + b_{+,i}^\dagger b_{+,i} + b_{-,i}^\dagger b_{-,i}$. Under the assumption of identical cavities the model exhibits an extra $U(1)$ symmetry. This is evident from Fig. C.2 where the mean-field energy landscape (color map) is plotted as a function of the cavities fields for different values of the cavities frequencies $\Omega_1 = 1$, $\Omega_2 = 4$ (top left panel), $\Omega_1 = 4$, $\Omega_2 = 1$ (top right panel), $\Omega_1 = \Omega_2 = 1$ (bottom panel). The equilibrium phase transition can be recovered minimizing the classical Hamiltonian

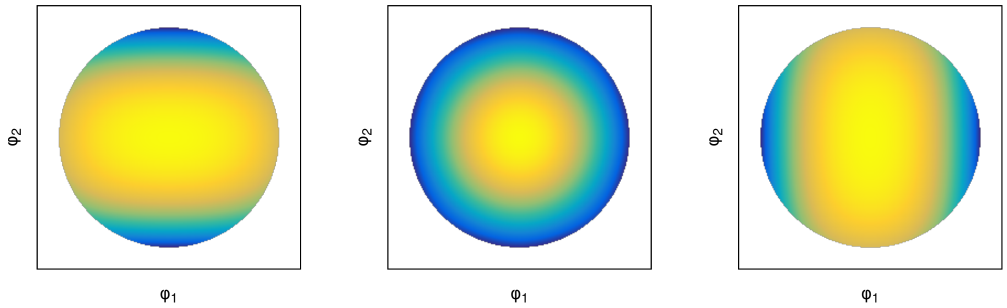

Figure C.2: Mean-field energy landscape of the model in Eq. (C.4) for $\Omega_1 = 1$, $\Omega_2 = 4$ (left panel), $\Omega_1 = \Omega_2 = 1$ (central panel) and $\Omega_1 = 4$, $\Omega_2 = 1$ (right panel), fixed $\omega_\pm = 1$ and $\lambda = 10.3\omega_r$.

$$H = N\sum_{i=1,2}\left[\Omega_i\varphi_i^2 + \omega_+\psi_{i+}^2 + \omega_-\psi_{i-}^2 + 4\lambda_i\varphi_i\psi_0\left(\psi_{+i} + \psi_{-i}\right)\right], \tag{C.5}$$

obtained by substituting $a_i = \sqrt{N}\varphi_i$, $b_{\pm,i} = \sqrt{N}\psi_{\pm,i}$, $b_{0,i} = \sqrt{N}\psi_{0,i}$, under the constrain $\psi_0 = \sqrt{1 - \sum_i(\psi_{+i}^2 + \psi_{-i})}$. The equilibrium phase diagram is shown in Fig. C.3 where the ground state photonic population $\langle a_i^\dagger a_i\rangle_0$ (color map) is plotted as a function of the cavities detuning Ω_1, Ω_2 for both cavities. Each cavity undergoes a quantum phase transition from a normal to a superradiant phase at the critical

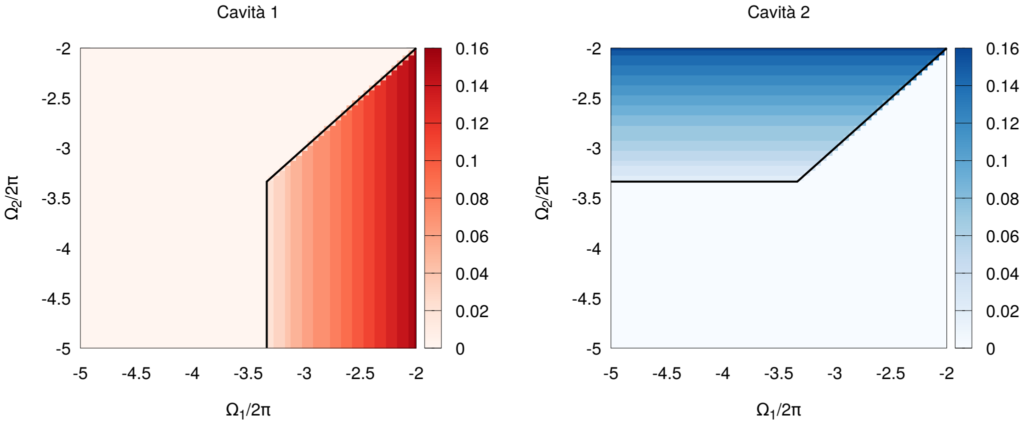

Figure C.3: Equilibrium phase diagram of the "Donner Hamiltonian" obtained with a mean-field analysis for $\lambda = 13\ \omega_r$, red and blue indicate, respectively, photons in cavity one and two. Dark blue lines are the mean-field critical lines.

point $\lambda_{c,i} = \sqrt{\bar{\omega}\Omega_i}/2$, with $\bar{\omega}^{-1} = \omega_+^{-1} + \omega_-^{-1}$. Only in the case of identical cavities, i.e. the case in which the system is also U(1) symmetric, superradiance is observed in both cavities simultaneously.

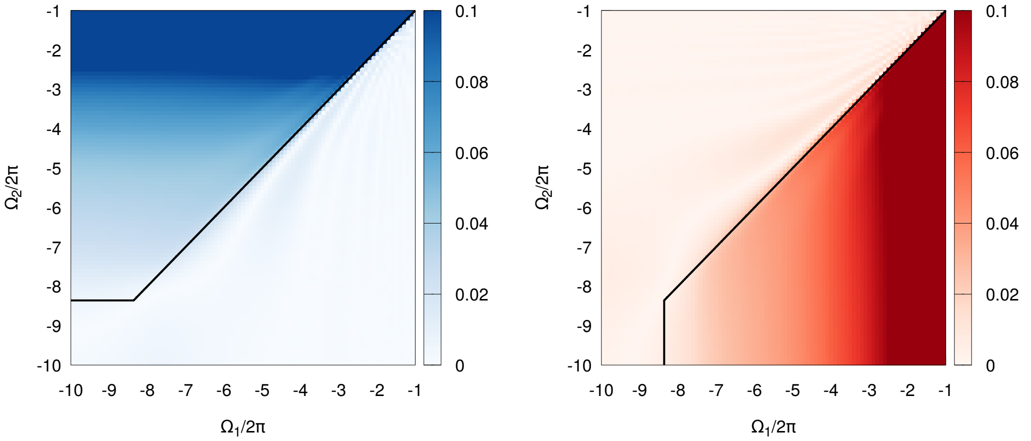

Figure C.4: Dynamical phase diagram for the two cavities with $\lambda = 10.3\omega_r$ and $\Omega_1 = \Omega_2 = 1$. The plot shows the value of the cavity fields respectively in cavity 1 and in cavity 2 as a function of the quenched cavity frequencies Ω_1 and Ω_2. Black line is obtained inverting the relation for the empirical dynamical critical value $\frac{\lambda_{\mathrm{cr}}^{\mathrm{eq}}(\Omega_i)}{2}$.

Posing $\varphi_j = \varphi_j^r + i\varphi_j^i$ and $\psi_{\pm j} = \psi_{\pm j}^r + i\psi_{\pm j}^i$, the classical dynamics is given by this set of coupled differential equations

$$\begin{cases} \dot{\varphi}^r_j = -\Omega \varphi^i_j, \\ \dot{\varphi}^i_j = \Omega \varphi^r_j + 2\lambda_j \psi_0 \left(\psi^r_{+,j} + \psi^i_{-j} \right), \\ \dot{\psi}^r_{\pm j} = -\omega_\pm \psi^i_{\pm j} + 2\lambda_j \ \varphi^r_j \frac{\psi^i_{\pm j} \sum_j \left(\psi^r_{+j} + \psi^r_{-j} \right)}{\psi_0}, \\ \dot{\psi}^i_{\pm j} = \omega_\pm \psi^r_{\pm j} + 2\lambda_j \ \varphi^r_j \left(\psi_0 - \frac{\psi^r_{\pm j} \sum_j \left(\psi^r_{+j} + \psi^r_{-j} \right)}{\psi_0} \right), \end{cases} \tag{C.6}$$

being $j = 1, 2$ the cavity index and $\psi_0 = \sqrt{1 - \sum_{j=1,2} (|\psi^+_j|^2 + |\psi^-_j|^2)}$.

Let us assume to prepare the system in the ground state of $\Omega_1 = \Omega_2 = 1$ (broken phase) and to quench the values of the cavities detuning Ω_1, Ω_2. The dynamical phase diagram is shown in Fig. C.4, where we plot the values of the cavity field φ_i for both the cavities as a function of the post-quench detuning. We show the value of $\overline{\varphi}_i = \lim_{T \to \infty} \frac{1}{T} \int_0^T dt \ \varphi_i(t)$ for the two cavities as a function of the post-quench detuning. The black line $\lambda^d_c = \lambda_c / 2$, empirically chosen, locates the dynamical phase transition.

D

From classical to quantum chaos

In the thermodynamic limit the Dicke Hamiltonian is exactly integrable. Moving toward finite sizes the integrability breaks and the system is allowed to display quantum chaotic effects. A possible signature of the quantum chaos is the character of the nearest-neighborhood energy level distribution $P(S)$, as conjectured by Bohigas [67]. Classical integrable systems have high degrees of freedom resulting in many conserved quantum numbers in their quantum counterpart that allow level crossing in the spectrum that is expected to be peaked on $S = 0$. Once the integrability is broken and the system behaves chaotically, the quantum energy spectrum is expected to be highly correlated and absent of crossing leading to a $P(S \to 0) \to 0$. The precise form of the $P(S)$ for such systems strongly depends on the symmetries of the model, but one of the most popular (that turns out to be the relevant one in the case of the Dicke model) is the Wigner-Dyson distribution $P(S) = \frac{\pi S}{2} \exp\left(-\frac{\pi S^2}{4}\right)$. More details can be found in [68, 69, 71–75].

Emary and collaborator [127, 128] have shown that the finite size Dicke Hamiltonian displays such a crossover in the quantum energy spectrum exactly at the critical point λ_c. To this purpose they diagonalize exactly the Hamiltonian to evaluate the distribution function $P(S)$ on the unfolded spectrum [70]. In Fig. D.1 we show our reproduction of their results. They have been obtained diagonalizing the Hamiltonian in a Hilbert space product of the total pseudospin Hilbert space with $N = 10$ and the truncated (we chose the maximum number of bosons $n = 100$) bosonic one. The diagonalization is performed in the even parity sector of the Hilbert space. It is evident the crossover from a Poisson distribution to a Wigner-Dyson one. In

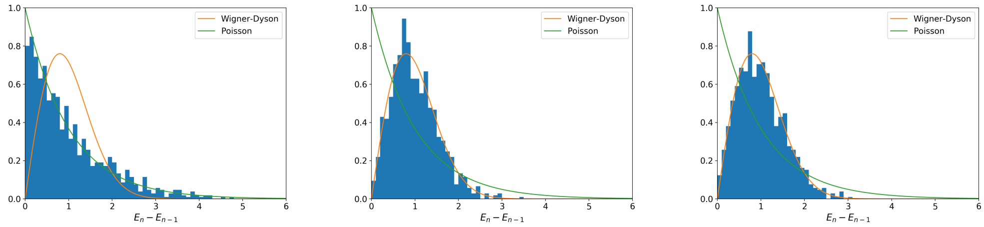

Figure D.1: Nearest-neighborhood level distribution for the Dicke model for the three different values of the coupling (from left to right) $\lambda = 0.4\lambda_c, 1.0\lambda_c, 1.6\lambda_c$. The spectrum has been derived assuming $N = 10$ and truncating the bosonic Hilbert space to $n = 100$. The orange line represents the Wigner-Dyson distribution, while the green line is the Poisson one. The coupling $\lambda = 1.0\lambda_c$ is the critical value at which the distribution qualitative changes.

this work the authors verify that this signature is, according with the conjecture of Bohigas, the counterpart of a classical chaotic behaviour. The classical Hamiltonian is obtained first expressing the quantum Hamiltonian in Eq. (3.13) in terms of coordinate-momentum operators $\hat{x}, \hat{p}$ [127, 128] and then assuming $[\hat{x}, \hat{p}] = 0$. This way the Hamiltonian becomes

$$H^{\mathrm{cl}} = -N\omega_0 + \frac{1}{2}\left(\omega^2 x_a^2 + p_a^2 + \omega_0 x_b^2 + p_b^2\right) + 2\lambda\sqrt{\omega\omega_0}\, x_a x_b \sqrt{1 - \frac{\omega_0^2 x_b^2 + p_b^2}{4N\omega_0}}, \tag{D.1}$$

that in the limit $N \to \infty$ reduces to Eq. (3.15). The Hamilton equations for the conjugate variables (fixed $\tilde{\lambda} = 2\lambda\sqrt{\omega\omega_0}$) are easily derived

$$\begin{aligned}
\dot{p}_a &= -\ \omega^2 x_a - \tilde{\lambda} x_b \sqrt{1 - \frac{\omega_0^2 x_b^2 + p_b^2}{4N\omega_0}}, \\
\dot{x}_a &= \quad p_a, \\
\dot{p}_b &= -\ \omega_0^2 x_b - \tilde{\lambda} x_a \sqrt{1 - \frac{\omega_0^2 x_b^2 + p_b^2}{4N\omega_0}} + \frac{\tilde{\lambda} x_a \omega_0 x_b^2}{4N\sqrt{1 - \frac{\omega_0^2 x_b^2 + p_b^2}{4N\omega_0}}}, \\
\dot{x}_b &= \quad p_b - \frac{\tilde{\lambda} x_a x_b p_b}{4N\omega_0\sqrt{1 - \frac{\omega_0^2 x_b^2 + p_b^2}{4N\omega_0}}}.
\end{aligned} \tag{D.2}$$

A trivial solution is $x_a = x_b = p_a = p_b$ and it is stable for $\lambda < \lambda_c^{\mathrm{N}} = \frac{\lambda_c}{\sqrt{1-1/4N}}$. When the coupling crosses this critical value two other fixed points

$$\left(x_a = \pm x_a^N, p_a = 0, x_b = \pm x_b^N, p_b = 0\right) \tag{D.3}$$

appear, with $x_{a(b)}^N$ some function of ω, λ, N that can be analytically derived. The interesting result is that the system undergoes a rapid change at $\lambda = \lambda_c^N$ from a simple quasi periodic behaviour to an intricate chaotic behaviour. This is shown in Fig. D.2, where we reproduce the phase space projection ($p_a = p_b = 0$) for the classical Dicke Hamiltonian. The trajectories are obtained choosing $N = 100$, $\omega = \omega_0 = 1$ for the different values of the coupling $\lambda = 1.0\lambda_c, 1.06\lambda_c, 1.2\lambda_c, 1.6\lambda_c$. The initial condition is $x_a(0) = x_b(0) = 1, p_a(0) = p_b(0) = 0$.

The same result could be obtained in the case of the two cavities model presented by Donner and collaborators [178]. In terms of conjugate variables the Hamiltonian reads

$$\begin{aligned}
H =& \frac{1}{2}\sum_i \left(\Omega^2 x_{a_i}^2 + p_{a_i}^2 + \omega_+ x_{+i}^2 + p_{+i}^2 + \omega_{-i} x_{-i}^2 + p_{-i}^2\right) \\
&+ 2\lambda\sqrt{\omega}\sqrt{1 - \sum_j \frac{\omega_+^2 x_{+j}^2 + p_{+j}^2}{4N\omega_+} - \frac{\omega_-^2 x_{-j}^2 + p_{-j}^2}{4N\omega_-}} \sum_i x_{a_i}(\sqrt{\omega_+} x_{+i} + \sqrt{\omega_-} x_{-i}),
\end{aligned} \tag{D.4}$$

namely a set of six coupled harmonic oscillators whose classical limit is well defined. The trajectories in the projected phase space of the associated classical equation of motions display the same chaotic behaviour discussed above.

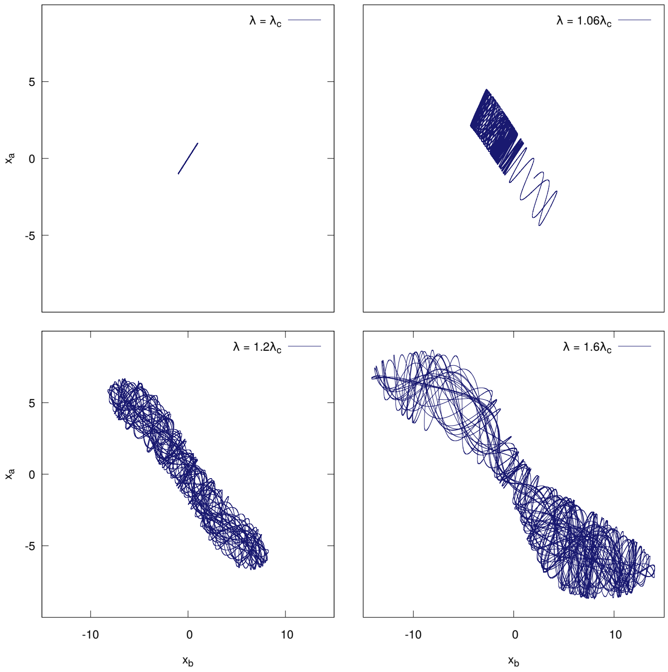

Figure D.2: phase space projection ($p_a = p_b = 0$) for the classical Dicke Hamiltonian. The trajectories are obtained choosing $N = 100$, $\omega = \omega_0 = 1$ for the different values of the coupling $\lambda = 1.0\lambda_c, 1.06\lambda_c, 1.2\lambda_c, 1.6\lambda_c$. The initial condition is $x_a(0) = x_b(0) = 1, p_a(0) = p_b(0) = 0$.

E

Time-dependent spin waves approximation

The time dependent spin-waves approximation [180] is a generalization of the spin waves expansion in a time-dependent framework aligned with the mean-spin direction (MSD) defined in Appendix B. First it is necessary to perform a time-dependent change of frame according to the right-handed Cartesian triple

$$\hat{Z} := \begin{bmatrix} \sin\theta\cos\phi \\ \sin\theta\sin\phi \\ \cos\theta \end{bmatrix} \qquad \hat{X} := \begin{bmatrix} \cos\theta\cos\phi \\ \cos\theta\sin\phi \\ -\sin\theta \end{bmatrix} \qquad \hat{Y} := \begin{bmatrix} -\sin\phi \\ \cos\phi \\ 0 \end{bmatrix} \tag{E.1}$$

implemented by the unitary operator

$$V = \exp\left(\frac{i\phi}{2}\sum_j \sigma_j^z\right)\exp\left(\frac{i\theta}{2}\sum_j \sigma_j^y\right). \tag{E.2}$$

The spin operators in the rotating frame σ^α are obtained by applying the rotation to the Pauli matrices in the fixed one τ^α

$$\sigma_j^X \equiv V\tau_j^x V^\dagger = \hat{X}\cdot\vec{\tau}_j, \quad \sigma_j^Y \equiv V\tau_j^y V^\dagger = \hat{Y}\cdot\vec{\tau}_j, \quad \sigma_j^Z \equiv V\tau_j^z V^\dagger = \hat{Z}\cdot\vec{\tau}_j. \tag{E.3}$$

The total spin operator is

$$\vec{\sigma}_j = \hat{X}\cdot\sigma_j^X + \hat{Y}\cdot\sigma_j^Y + \hat{Z}\cdot\sigma_j^Z. \tag{E.4}$$

In this new reference frame the Hamiltonian is time-dependent, hence the dynamics of the operators should account for an additional term (analogous to the apparent forces in classical mechanics) due to the rotation. The equation of motion for the generic operator O reduces to

$$\dot{O} = i[\tilde{H}, O], \tag{E.5}$$

with $\tilde{H} = H + iV\dot{V}^\dagger$ and

$$iV\dot{V}^\dagger = -\frac{1}{2}\omega\cdot\sigma, \tag{E.6}$$

defined

$$\omega^X \equiv X\cdot\omega = -\sin\theta\dot{\phi}, \quad \omega^Y \equiv Y\cdot\omega = \dot{\theta}, \quad \omega^Z \equiv Z\cdot\omega = \cos\theta\dot{\phi}. \tag{E.7}$$

The motion of the frame can be deduced imposing the mean-spin direction α, namely

$$\langle\sigma^\beta(t)\rangle \equiv \langle\sigma^\gamma(t)\rangle \equiv 0 \qquad \langle\sigma^\beta(0)\rangle \equiv \langle\sigma^\gamma(0)\rangle \equiv 0, \tag{E.8}$$

and it is equivalent to require $\dot\sigma^\beta, \dot\sigma^\gamma = O(1)$.

Let us apply the time-dependent spin wave approximation to study the nonequilibrium dynamics of the long-range interacting Ising chain in Eq. (3.19). In the frame rotated according to Eq. (E.1) the Hamiltonian reads

$$\begin{aligned}\frac{\tilde H}{N} =& - J_0 \left(\frac{V_{Xx}\sigma_0^X + V_{Yx}\sigma_0^Y + V_{Zx}\sigma_0^Z}{N} \right)^2 - h \left(\frac{V_{Xz}\sigma_0^X + V_{Yz}\sigma_0^Y + V_{Zz}\sigma_0^Z}{N} \right) \\ & - \sum_{k\neq 0} J_k \left(\frac{V_{Xx}\sigma_k^X + V_{Yx}\sigma_k^Y + V_{Zx}\sigma_k^Z}{N} \right) \left(\frac{V_{Xx}\sigma_{-k}^X + V_{Yx}\sigma_{-k}^Y + V_{Zx}\sigma_{-k}^Z}{N} \right) \\ & + \frac{\sin\theta \;\; \dot\phi}{2} \frac{\tilde\sigma_0^X}{N} - \frac{\dot\theta}{2}\frac{\tilde\sigma_0^Y}{N} - \frac{\cos\theta \;\dot\phi}{2}\frac{\tilde\sigma_0^Z}{N}.\end{aligned} \tag{E.9}$$

We perform the Holstein-Primakoff on the real space operators choosing $\alpha = Z$ as the mean spin direction[1] the motion of the frame is given imposing $\dot\sigma^X, \dot\sigma^Y$ to be non-extensive. Solving the Heisenberg equation we have

$$\begin{cases} \sigma_j^X &= b_j^\dagger + b_j - \frac{b_j^\dagger \left(b_j^\dagger + b_j\right) b_j}{2}, \\ \sigma_j^Y &= i\left(b_j^\dagger - b_j\right) - \frac{i b_j^\dagger \left(b_j^\dagger - b_j\right) b_j}{2}, \\ \sigma_j^Z &= 1 - 2 b_j^\dagger b_j. \end{cases} \tag{E.10}$$

The Fourier-transformation reads

$$\begin{cases} \sigma_k^X &= \sqrt{N}\left(b_{-k}^\dagger + b_k\right) - \frac{\sum_{qp} b_{p-k-q}^\dagger \left(b_q^\dagger + b_{-q}\right) b_p}{2\sqrt{N}} \\ \sigma_k^Y &= i\sqrt{N}\left(b_k^\dagger - b_{-k}\right) - \frac{i\sum_{qp} b_{p+k-q}^\dagger \left(b_q^\dagger - b_{-q}\right) b_p}{2\sqrt{N}} \\ \sigma_k^Z &= N\delta_{k,0} - 2\sum_q b_q^\dagger b_{q+k}. \end{cases} \tag{E.11}$$

with $b_j = \frac{1}{\sqrt{N}}\sum_k e^{ikj} b_k$. Up to quadratic order in the fluctuations, the total spin $\sigma^2 = \sigma_0^{X^2} + \sigma_0^{Y^2} + \sigma_0^{Z^2}$ is given by

$$\sigma^2 \approx \left(N - 2\sum_{k\neq 0} b_k^\dagger b_k \right)\left(N - 2\sum_{k\neq 0} b_k^\dagger b_k + 1 \right), \tag{E.12}$$

that means that the spin waves, i.e. fluctuations with a finite momentum, are responsible for the destruction of the mean field direction.[2] The Holstein-Primakoff approximation is valid as long as the MSD is not destructed, i.e. as long as the density of spin waves $\varepsilon = \frac{2}{N}\sum_{k\neq 0}\langle b_k^\dagger b_{-k}\rangle$ remains small.

---

[1] Actually the MSD can not be totally arbitrary. The parametrization is singular in the ferromagnetic fixed point and it is not allowed to chose that as mean-spin direction.

[2] The zero momentum fluctuations do no contribute to the destruction of the MSD but contributes to the dynamics of the spin squeezing (see Appendix B). For this reason the dynamics of the correlator $\langle b_0^\dagger b_0\rangle$ grows for time larger than the Ehrenfest time. Since in what follows we assume to work in the thermodynamic limit, we neglect its dynamics for the rest of the discussion.

Being H_0 the 0-mode part of the Hamiltonian, we have $\tilde{H} = \tilde{H}_0 + \tilde{V}$. The first one reads

$$\tilde{H}_0 = x(t)\frac{\sigma_0^X}{N} + y(t)\frac{\sigma_0^Y}{N} + z(t)\frac{\sigma_0^Z}{N} - J_0 \left(V_{Xx}\frac{\sigma_0^X}{N} + V_{Yx}\frac{\sigma_0^Y}{N} + V_{Zx}\frac{\sigma_0^Z}{N} \right)^2 , \tag{E.13}$$

with

$$x(t) = h\sin\theta + \sin\theta s\dot{\varphi}, \qquad y(t) = -s\dot{\theta}, \qquad z(t) = -h\cos\theta - \cos\theta s\dot{\varphi}. \tag{E.14}$$

We observe that this term preserves the number of bosons, in fact the terms with an odd number of bosons $\tilde{H}_0^{\mathrm{odd}}$

$$\tilde{H}_0^{\mathrm{odd}} = \left(x(t) - 2J_0 \sin\theta\cos\theta\cos^2\varphi\frac{\sigma_0^Z}{N} \right) \frac{\sigma_0^X}{N} + \left(y(t) + 2J_0\sin\theta\cos\varphi\sin\varphi\frac{\sigma_0^Z}{N} \right) \frac{\sigma_0^Y}{N} = 0. \tag{E.15}$$

are vanishing by virtue of the frame equations of motion. In accordance with the conservation of the total angular momentum this implies σ^{tot} to contain even power of the boson operators. The effect of the zero momentum part of the Hamiltonian on the motion of the frame is obtained imposing

$$\begin{aligned} \dot{\sigma}^X &= \frac{1}{i}\left[X\cdot\vec{\tau}, \tilde{H}\right] = N \left(-\frac{\dot{\theta}}{2} + 2J_0\sin\theta\cos\phi\sin\phi\ \frac{\sigma^Z}{N} \right) \frac{\sigma^Z}{N} + O(N^0), \\ \dot{\sigma}^Y &= \frac{1}{i}\left[Y\cdot\vec{\tau}, \tilde{H}\right] = N \left(-\frac{\sin\theta\dot{\phi}}{2} - h\sin\theta + 2J_0\cos\theta\cos^2\phi\sin\theta\ \frac{\tilde{\sigma}_0^Z}{N} \right) \frac{\tilde{\sigma}_0^Z}{N} + O(N^0). \end{aligned} \tag{E.16}$$

to be non-extensive

$$\begin{aligned} \dot{\phi} &= 4J\cos\theta\cos^2\phi\frac{\tilde{\sigma}^Z}{N} - 2h, \\ \dot{\theta} &= 4J\sin\theta\cos\phi\sin\phi\frac{\tilde{\sigma}^Z}{N}. \end{aligned} \tag{E.17}$$

To see the effect of the fluctuations we first write $k \neq 0$ part of the hamiltonian V

$$\begin{aligned} \tilde{V} = &-\sum_k \frac{J_k}{N^2}\left(\cos^2\theta\cos^2\phi\ \sigma_k^X\sigma_{-k}^X + \sin^2\phi\ \sigma_k^Y\sigma_{-k}^Y + \sin^2\theta\cos^2\phi\ \sigma_k^Z\sigma_{-k}^Z\right) \\ &-\sum_{k\neq 0} \frac{J_k}{N^2}\sin\theta\left(\cos\theta\cos^2\phi\left(\sigma_k^X\sigma_{-k}^Z + \sigma_k^Z\sigma_{-k}^X\right) - \cos\phi\sin\phi\left(\sigma_k^Y\sigma_{-k}^Z + \sigma_k^Z\sigma_{-k}^Y\right)\right) \\ &+\sum_k \frac{J_k}{N^2}\sin\phi\cos\phi\cos\theta\left(\sigma_k^X\sigma_{-k}^Y + \sigma_k^Y\sigma_{-k}^X\right). \end{aligned} \tag{E.18}$$

To account for the effects of the spin-waves in the frame equations of motion adding we impose the following terms

$$\begin{aligned}
\left[\tilde{V},\sigma_0^X\right] &= -\frac{N}{i}\sum_{k\neq 0} J_k \left(f(\theta,\phi)\left(\frac{\sigma_k^X\sigma_{-k}^Y+\sigma_k^Y\sigma_{-k}^X}{N^2}\right) + 2g(\theta,\phi)\frac{\sigma_k^Y\sigma_{-k}^Y}{N^2}\right) + O\left(\frac{1}{\sqrt{N}}\right) \\
&= -\frac{2N}{i}\sum_{k\neq 0} J_k \left(f(\theta,\phi)\left(\frac{b^\dagger_{-k}b^\dagger_k+b_kb_{-k}}{N}\right) - g(\theta,\phi)\frac{\left(b^\dagger_k-b_{-k}\right)\left(b^\dagger_{-k}-b_k\right)}{N}\right) \\
&+\ O\left(\frac{1}{\sqrt{N}}\right),
\end{aligned}$$

$$\begin{aligned}
\left[\tilde{V},\sigma_0^Y\right] &= \frac{N}{i}\sum_{k\neq 0} J_k \left(2f(\theta,\phi)\frac{\sigma_k^X\sigma_{-k}^X}{Ns} - g(\theta,\phi)\left(\frac{\sigma_k^X\sigma_{-k}^Y+\sigma_k^Y\sigma_{-k}^X}{N^2}\right)\right) + O\left(\frac{1}{\sqrt{N}}\right) \\
&= \frac{2N}{i}\sum_{k\neq 0} J_k \left(f(\theta,\phi)\frac{\left(b^\dagger_k+b_{-k}\right)\left(b^\dagger_{-k}+b_k\right)}{N} - g(\theta,\phi)\left(\frac{b^\dagger_{-k}b^\dagger_k+b_kb_{-k}}{N}\right)\right) \\
&+ O\left(\frac{1}{\sqrt{N}}\right),
\end{aligned} \tag{E.19}$$

where $f(\theta,\phi)=\cos^2\phi\sin(2\theta)$ and $g(\theta,\phi)=\sin(2\phi)\sin\theta$. to be non-extensive. This leads to

$$\begin{cases}
\dot{\theta}(t) = 2J_0\sin\theta\sin(2\phi)(1-\varepsilon) - 4\sum_{k\neq 0} J_k\left(\cos^2\phi\sin(2\theta)\frac{\Delta_k^r}{N} + \sin(2\phi)\sin\theta\ \frac{\Delta_k^r-\Delta_k^b}{N}\right), \\
\dot{\phi}(t) = -2h + 4J_0(1-\varepsilon)\cos\theta\cos^2\phi + 4\sum_{k\neq 0} J_k\left(\cos^2\phi\cos\theta\frac{\Delta_k^r+\Delta_k^b}{N} - \sin(2\phi)\frac{\Delta_k^r}{N}\right),
\end{cases} \tag{E.20}$$

defined

$$\Delta_k^b = \langle b_k^\dagger b_k + b_{-k}b^\dagger_{-k}\rangle\,,\quad \Delta_k^r = \langle b_kb_{-k} + b_k^\dagger b^\dagger_{-k}\rangle\,,\quad \Delta_k^i = i\ \langle b_kb_{-k} - b_k^\dagger b^\dagger_{-k}\rangle\,. \tag{E.21}$$

The equations of motion for the correlators are given by the quadratic Hamiltonian

$$H^f = \sum_{k\neq 0}\tilde{\varepsilon}_k\left(b_k^\dagger b_k + b_{-k}b^\dagger_{-k}\right) + \tilde{\lambda}_k b_k^\dagger b^\dagger_{-k} + \tilde{\lambda}_k^* b_kb_{-k} + \text{const} + O(1/\sqrt{N}), \tag{E.22}$$

with

$$\begin{aligned}
\tilde{\varepsilon}_k &= \cos^2\phi\sin^2\theta(J_k-2J_0) - J_k, \\
\tilde{\lambda}_k &= J_k\left(\cos^2\phi\sin^2\theta - 1 + i\sin(2\phi)\cos\theta\right).
\end{aligned} \tag{E.23}$$

This gives

$$\begin{aligned}
\dot{\Delta}_k^b &= 4Re(\lambda_k)\Delta_k^i + 4Im(\lambda_k)\Delta_k^r, \\
\dot{\Delta}_k^r &= -4\varepsilon_k\Delta_k^i + 4Im(\lambda_k)\Delta_k^b, \\
\dot{\Delta}_k^i &= 4\varepsilon_k\Delta_k^r + 4Re(\lambda_k)\Delta_k^b.
\end{aligned} \tag{E.24}$$

The stability of the approximation is determined by the instantaneous dispersion relation of the spin waves, i.e. the quasi-energies of the Hamiltonian H^f_{fixed} fixed $\dot{\theta} = \dot{\phi} = 0$

$$H^f_{\text{fixed}} = -\sum_{k\neq 0} \epsilon_k \left(b_k b_k^\dagger + b_{-k}^\dagger b_{-k}\right) + \Lambda_k b_k b_{-k} + \Lambda_k^* b_{-k}^\dagger b_k^\dagger, \tag{E.25}$$

with

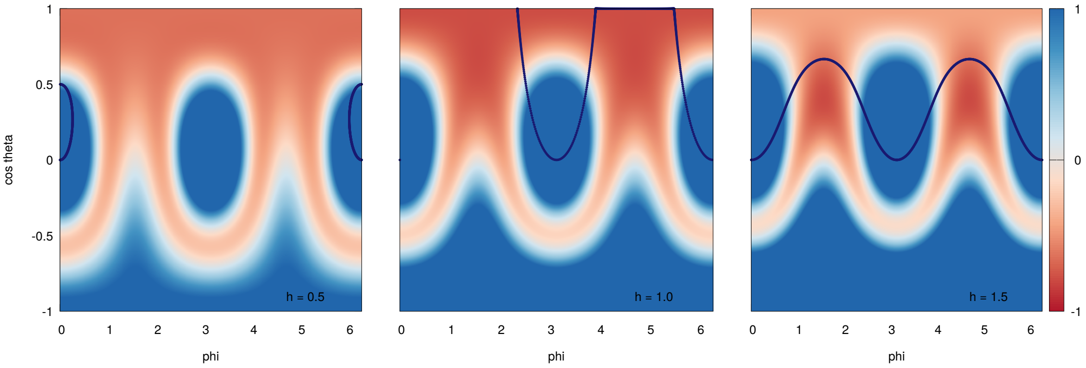

Figure E.1: Square of the dispersion E_k^2 (color map) as a function of the azimuthal angle ϕ and $\cos\theta$ for the three different transverse fields $h = 0.5, 1.0, 1.5$ fixed $\alpha = 1.2$. The blue line is the mean-field trajectory in the phase space at that final value of the transverse field.

$$\begin{aligned} \epsilon_k &= J_k(\cos^2\phi\cos^2\theta + \sin^2\phi) - 2J_0\cos^2\phi\sin^2\theta - h\cos\theta, \\ \Lambda_k &= J_k(\cos\phi\cos\theta + i\sin\phi)^2. \end{aligned} \tag{E.26}$$

The dispersion relation reduces to

$$E_k = \sqrt{\left(2\tilde{J}_0\cos^2\phi + h\cos\theta\right)\left(2\cos^2\phi\left(\tilde{J}_0 - J_k\cos^2\theta\right) + h\cos\theta - 2J_k\sin^2\phi\right)}, \tag{E.27}$$

where $\tilde{J}_0 = J_0\sin^2\phi$. In the correspondence of the ferromagnetic point the approximation is always stable independently on the transverse field value $E_k(\theta = \frac{\pi}{2}, \phi = 0) = \pm 2J_0$. As expected, in the paramagnetic point (in which ϕ is not well defined) the energy does not depend on the azimuthal angle $E_k(\theta = 0, \phi) = \sqrt{h\,(h - 2J_k)}$. Whenever we have $J_{k\neq 0} = 0$ since

$$E_k^2(J_{k\neq 0} = 0) = \left(2J_0\cos^2\phi\sin^2\theta + h\cos\theta\right)^2 > 0 \quad \forall h, \tag{E.28}$$

the approximation is stable. This means that in the thermodynamic limit the spin waves expansion is valid for $\alpha < 1$. The stability of the spin waves approximation for $\alpha \geq 1$ could be studied numerically. In Fig. E.1 we plot the square of the dispersion E_k^2 (color map) as a function of the azimuthal angle ϕ and of $\cos\theta$ for three different transverse fields $h = 0.5, 1.0, 1.5$ fixed $\alpha = 1.2$. The blue line is the mean-field trajectory in the phase space. Every time the classical trajectory crosses an instability region the spin waves density increases leading to the failure of the approximation. This result suggests that the spin-waves expansion is stable only for quenches that are below the mean-field dynamical critical point $h = 1$ and can not be used to study the dynamics after critical quench.

F

Cluster mean-field Lindblad equation – Derivation

In this appendix we derive the cluster mean-field equation for the density matrix for the power law decaying Ising chain in presence of dissipation.

The cluster mean-field equations of motion are obtained assuming the density matrix to be a product of cluster density matrices $\rho = \bigotimes_{\beta}^{N} \rho_\beta$, with β a cluster index and ρ_β of dimension $2^\ell \times 2^\ell$ with ℓ the cluster dimension. The effective master equation is obtained tracing out all the cluster egrees of freedom but one

$$\dot{\rho}_\beta = \partial \mathrm{Tr}_{\neq beta}(\rho) = \mathrm{Tr}_{\neq beta}\mathcal{L}(\rho). \tag{F.1}$$

In this derivation we use the following properties of the Kronecker product

1. $(A \otimes B)(C \otimes D) = AC \otimes BD$,
2. $\mathrm{Tr}\,(A \otimes B) = \mathrm{Tr}\,(B \otimes A) = \mathrm{Tr}(A)\mathrm{Tr}(B)$.

F.1 Glauber dissipation

Let us consider jump operators of the form $\sigma_s^\pm = \sum_l^{N_{\text{siti}}} \sigma_l^\pm$, where $\sigma_\ell^\pm \equiv I_1 \otimes ..\sigma_\ell^\pm \otimes ..I_N$ are single site operators. The master equation reads

$$\dot{\rho} = \sum_{l,m}^{N_{\text{siti}}} \frac{\Gamma_+}{N_{\text{siti}}} \left(\sigma_l^- \rho \sigma_m^+ - \frac{1}{2}\{\sigma_l^+ \sigma_m^-, \rho\} \right) + \frac{\Gamma_-}{N_{\text{siti}}} \left(\sigma_l^+ \rho \sigma_m^- - \frac{1}{2}\{\sigma_l^- \sigma_m^+, \rho\} \right). \tag{F.2}$$

We consider a product density matrix of the form $\rho = \bigotimes_{\beta}^{N_{\text{cl}}} \rho_\beta$ with ρ_β single cluster density matrices of dimension $2^\ell \times 2^\ell$, with ℓ the length of the cluster β. The spin operators acting on the cluster β are defined $\sigma_{\beta,l}^\pm \equiv I_1 \otimes ..\sigma_l.. \otimes I_\ell$ with $l \in \beta$. Let us focus on the first term and then the other follows automatically.

$$\begin{aligned}
&\sum_{l,m} \left(\sigma_l^- \bigotimes_{\beta}^{N_{\text{cl}}} \rho_\beta \sigma_m^+ - \frac{1}{2}\{\sigma_l^+ \sigma_m^-, \bigotimes_{\beta}^{N_{\text{cl}}} \rho_\beta\} \right) \\
&= \sum_{m,l}^{\ell} \left(\sigma_{\beta,l}^- \rho_\beta \sigma_{\beta,m}^+ - \frac{\sigma_{\beta,l}^+ \sigma_{\beta,m}^- \rho_\beta}{2} - \frac{\rho_\beta \sigma_{\beta,l}^+ \sigma_{\beta,m}^-}{2} \right) \\
&+ \sum_{l,m}^{\ell} \left(\sigma_{\beta,l}^- \rho_\beta \otimes \rho_\alpha \sigma_{\alpha,m}^+ - \frac{\sigma_{\beta,l}^+ \rho_\beta \otimes \sigma_{\alpha,m}^- \rho_\alpha}{2} - \frac{\rho_\beta \sigma_{\beta,l}^+ \otimes \rho_\alpha \sigma_{\alpha,m}^-}{2} \right)
\end{aligned} \tag{F.3}$$

where, for simplicity of notation, we pose

$$\begin{aligned} &\sigma^{\pm}_{\beta,l}\rho_\beta\sigma^{\mp}_{\beta,m} \equiv \rho_1\otimes\ldots\sigma^{\pm}_{\beta,l}\rho_\beta\sigma^{\mp}_{\beta,m}\cdots\otimes\rho_{N_{\rm cl}},\\ &\sigma^{\pm}_{\alpha,l}\rho_\alpha\otimes\rho_\beta\sigma^{\mp}_{\beta,m} \equiv \rho_1\otimes\ldots\sigma^{\pm}_{\alpha,l}\rho_\alpha\otimes\cdots\otimes\rho_\beta\sigma^{\mp}_{\beta,m}\cdots\otimes\rho_{N_{\rm cl}}. \end{aligned} \tag{F.4}$$

Tracing out the degrees of freedom we obtain

$$\begin{aligned} &{\rm Tr}_{\neq\gamma}\sum_{l,m}^{N}\left(\sigma^-_l\bigotimes_{\beta}^{N_{\rm cl}}\rho_\beta\sigma^+_m-\frac{1}{2}\{\sigma^+_l\sigma^-_m,\bigotimes_{\beta}^{N_{\rm cl}}\rho_\beta\}\right)\\ &={\rm Tr}_{\neq\gamma}\sum_{l,m}^{\ell}\left(\sigma^-_{\beta,l}\rho_\beta\otimes\rho_\alpha\sigma^+_{\alpha,m}-\frac{\sigma^+_{\beta,l}\rho_\beta\otimes\sigma^-_{\alpha,m}\rho_\alpha}{2}-\frac{\rho_\beta\sigma^+_{\beta,l}\otimes\rho_\alpha\sigma^-_{\alpha,m}}{2}\right)\\ &+\,{\rm Tr}_{\neq\gamma}\sum_{l,m}^{\ell}\left(\sigma^-_{\beta,l}\rho_\beta\sigma^+_{\beta,m}-\frac{\sigma^+_{\beta,l}\sigma^-_{\beta,m}\rho_\beta}{2}-\frac{\rho_\beta\sigma^+_{\beta,l}\sigma^-_{\beta,m}}{2}\right)\\ &=\frac{1}{2}\left(\sum_\alpha\sum_m^{\ell}{\rm Tr}'_{\neq\gamma}(\rho_\alpha\sigma^+_{\alpha,m})\right)\sum_i^{\ell}\left[\sigma^-_{\gamma,i},\rho_\gamma\right]+\frac{1}{2}\left(\sum_\alpha\sum_m^{\ell}{\rm Tr}'_{\neq\gamma}(\rho_\alpha\sigma^-_{\alpha,m})\right)\sum_i^{\ell}\left[\rho_\gamma,\sigma^+_{\gamma,i}\right]\\ &+\sum_{l,m}^{\ell}\left(\sigma^-_{\gamma,l}\rho_\gamma\sigma^+_{\gamma,m}-\frac{\sigma^+_{\gamma,l}\sigma^-_{\gamma,m}\rho_\gamma}{2}-\frac{\rho_\gamma\sigma^+_{\gamma,l}\sigma^-_{\gamma,m}}{2}\right), \end{aligned} \tag{F.5}$$

where we have used the identity[1] ${\rm Tr}_\alpha\left(\sigma^-_{\alpha,l}\rho_\alpha\sigma^+_{\alpha,m}-\frac{1}{2}\{\sigma^+_{\alpha,l}\sigma^-_{\alpha,m},\rho_\alpha\}\right)=0$ Assuming that all the clusters are equivalent we obtain the Lindblad equation for the cluster density matrix

$$\dot\rho=\frac{\overline{\Gamma}}{N_{\rm siti}}\sum_{ij}^{\ell}\left(\sigma^-_i\rho\sigma^+_j-\frac{1}{2}\{\sigma^+_i\sigma^-_j,\rho\}\right)+\frac{\delta\Gamma_{\rm cl}}{N_{\rm siti}}\sum_i\left(\frac{\langle\sigma^+\rangle_{\rm cl}\,[\sigma^-_i,\rho]}{2}+\frac{\langle\sigma^-\rangle_{\rm cl}\,[\rho,\sigma^+_i]}{2}\right), \tag{F.6}$$

with $\overline{\Gamma}=\Gamma_++\Gamma_-$ and $\delta\Gamma_{\rm cl}=(\Gamma_+-\Gamma_-)\,(N_{\rm siti}-\ell)\,\theta(N_{\rm siti}-\ell)$, with $\theta(x)$ the Heaviside function. The self-consistent expectation values $\langle\sigma^\pm\rangle=\langle\sum_i^\ell\sigma^\pm_i\rangle$ are evaluated on the cluster.

---

[1] Intuitively it is a consequence of the Lindblad form of the master equation that preserve the trace of the density matrix.

Bibliography

[1] G Gallavotti, *Statistical mechanics, a short treatise* (Springer, 1999).

[2] F. Reif, *Fundametnals of statistical and thermal physics* (McGraw-Hill, 1965).

[3] T. Mori, T. N. Ikeda, E. Kaminishi, and M. Ueda, “Thermalization and prethermalization in isolated quantum systems: a theoretical overview”, Journal of Physics B: Atomic, Molecular and Optical Physics **51**, 112001 (2018) `10.1088/1361-6455/aabcdf`.

[4] J. von Neumann, “Proof of the ergodic theorem and the h-theorem in quantum mechanics”, The European Physical Journal H **35**, 201–237 (2010) `10.1140/epjh/e2010-00008-5`.

[5] S. Goldstein, D. A. Huse, J. L. Lebowitz, and R. Tumulka, “Thermal equilibrium of a macroscopic quantum system in a pure state”, Physical Review Letters **115** (2015) `10.1103/physrevlett.115.100402`.

[6] S. Popescu, A. J. Short, and A. Winter, “Entanglement and the foundations of statistical mechanics”, Nature Physics **2**, 754–758 (2006) `10.1038/nphys444`.

[7] S. Goldstein, J. L. Lebowitz, R. Tumulka, and N. Zanghì, “Canonical typicality”, Physical Review Letters **96** (2006) `10.1103/physrevlett.96.050403`.

[8] O. Inozemcev and I. Volovich, *Does the eigenstate thermalization hypothesis imply thermalization?*, 2020.

[9] L. D’Alessio, Y. Kafri, A. Polkovnikov, and M. Rigol, “From quantum chaos and eigenstate thermalization to statistical mechanics and thermodynamics”, Advances in Physics **65**, 239–362 (2016) `10.1080/00018732.2016.1198134`.

[10] J. R. Garrison and T. Grover, “Does a single eigenstate encode the full hamiltonian?”, Physical Review X **8** (2018) `10.1103/physrevx.8.021026`.

[11] A. Polkovnikov, K. Sengupta, A. Silva, and M. Vengalattore, “Colloquium: nonequilibrium dynamics of closed interacting quantum systems”, Reviews of Modern Physics **83**, 863–883 (2011) `10.1103/revmodphys.83.863`.

[12] M. Rigol, V. Dunjko, and M. Olshanii, “Thermalization and its mechanism for generic isolated quantum systems”, Nature **452**, 854–858 (2008) `10.1038/nature06838`.

[13] T. Langen, R. Geiger, M. Kuhnert, B. Rauer, and J. Schmiedmayer, “Local emergence of thermal correlations in an isolated quantum many-body system”, Nature Physics **9**, 640–643 (2013) `10.1038/nphys2739`.

[14] A. Rosch, D. Rasch, B. Binz, and M. Vojta, “Metastable superfluidity of repulsive fermionic atoms in optical lattices”, Physical Review Letters **101** (2008) `10.1103/physrevlett.101.265301`.

[15] J. Marino and A. Silva, “Nonequilibrium dynamics of a noisy quantum ising chain: statistics of work and prethermalization after a sudden quench of the transverse field”, Physical Review B **89** (2014) `10.1103/physrevb.89.024303`.

[16] T. Langen, T. Gasenzer, and J. Schmiedmayer, “Prethermalization and universal dynamics in near-integrable quantum systems”, Journal of Statistical Mechanics: Theory and Experiment **2016**, 064009 (2016) `10.1088/1742-5468/2016/06/064009`.

[17] J. Berges, S. Borsanyi, and C. Wetterich, “Prethermalization”, Phys. Rev. Lett. **93**, 142002 (2004).

[18] M. Marcuzzi, J. Marino, A. Gambassi, and A. Silva, “Prethermlization from a low-density holstein-primakoff expansion”, Phys. Rev. B **94**, 214304 (2016).

[19] G. Menegoz and A. Siilva, “Prethermalization of weakly interacting bosons after a sudden interaction quench”, J. Stat. Mech. **P05035** (2015).

[20] C. Kollath, A. M. Läuchli, and E. Altman, “Quench dynamics and nonequilibrium phase diagram of the bose-hubbard model”, Physical Review Letters **98** (2007) `10.1103/physrevlett.98.180601`.

[21] M. Gring, M. Kuhnerta, T. Langen, T. Kitagawa, B. Rauer, M. Schreitl, L. Mazets, D. A. Smith, E. Demler, and J. Schmiedmayer, “Relaxation and prethermalization in an isolated quantum system”, Scince **337** (2012).

[22] J. Lang, B. Frank, and J. C. Halimeh, “Dynamical quantum phase transitions: a geometric picture”, Physical Review Letters **121** (2018) `10.1103/physrevlett.121.130603`.

[23] S. A. Weidinger, M. Heyl, A. Silva, and M. Knap, “Dynamical quantum phase transitions in systems with continuous symmetry breaking”, Physical Review B **96** (2017) `10.1103/physrevb.96.134313`.

[24] M. Sandri, M. Schiró, and M. Fabrizio, “Linear ramps of interaction in the fermionic hubbard model”, Physical Review B **86** (2012) `10.1103/physrevb.86.075122`.

[25] V. Gurarie, “Nonequilibrium dynamics of weakly and strongly paired superconductors”, Physical Review Letters **103** (2009) `10.1103/physrevlett.103.075301`.

[26] B. Sciolla and G. Biroli, “Quantum quenches and off-equilibrium dynamical transition in the infinite-dimensional bose-hubbard model”, Physical Review Letters **105** (2010) `10.1103/physrevlett.105.220401`.

[27] R. Barankov and L. Levitov, “Synchronization versus dephasing in the pairing dynamics of cold fermions”, APS, Y32 (2007).

[28] M. Eckstein, M. Kollar, and P. Werner, “Thermalization after an interaction quench in the hubbard model”, Physical review letters **103**, 056403 (2009) `10.1103/PhysRevLett.103.056403`.

[29] M. Schiró and M. Fabrizio, “Time-dependent mean field theory for quench dynamics in correlated electron systems”, Physical Review Letters **105** (2010) `10.1103/physrevlett.105.076401`.

[30] H. Watanabe and M. Oshikawa, “Absence of quantum time crystals”, Physical Review Letters **114** (2015) `10.1103/physrevlett.114.251603`.

[31] F. Gambetta, F. Carollo, M. Marcuzzi, J. Garrahan, and I. Lesanovsky, “Discrete time crystals in the absence of manifest symmetries or disorder in open quantum systems”, Physical Review Letters **122** (2019) `10.1103/physrevlett.122.015701`.

[32] C.-h. Fan, D. Rossini, H.-X. Zhang, J.-H. Wu, M. Artoni, and G. C. La Rocca, “Discrete time crystal in a finite chain of rydberg atoms without disorder”, Physical Review A **101** (2020) `10.1103/physreva.101.013417`.

[33] A. Russomanno, F. Iemini, M. Dalmonte, and R. Fazio, “Floquet time crystal in the lipkin-meshkov-glick model”, Physical Review B **95** (2017) `10.1103/physrevb.95.214307`.

[34] D. V. Else, B. Bauer, and C. Nayak, “Floquet time crystals”, Physical Review Letters **117** (2016) `10.1103/physrevlett.117.090402`.

[35] A. Lazarides, S. Roy, F. Piazza, and R. Moessner, “Time crystallinity in dissipative floquet systems”, Physical Review Research **2** (2020) `10.1103/physrevresearch.2.022002`.

[36] F. M. Surace, A. Russomanno, M. Dalmonte, A. Silva, R. Fazio, and F. Iemini, “Floquet time crystals in clock models”, Phys. Rev. B **99**, 104303 (2019) `10.1103/PhysRevB.99.104303`.

[37] J. Zhang, P. W. Hess, A. Kyprianidis, P. Becker, A. Lee, J. Smith, G. Pagano, I.-D. Potirniche, A. C. Potter, A. Vishwanath, and et al., “Observation of a discrete time crystal”, Nature **543**, 217–220 (2017) `10.1038/nature21413`.

[38] S. Choi, J. Choi, R. Landig, G. Kucsko, H. Zhou, J. Isoya, F. Jelezko, S. Onoda, H. Sumiya, V. Khemani, and et al., “Observation of discrete time-crystalline order in a disordered dipolar many-body system”, Nature **543**, 221–225 (2017) `10.1038/nature21426`.

[39] F. Iemini, A. Russomanno, J. Keeling, M. Schirò, M. Dalmonte, and R. Fazio, “Boundary time crystals”, Physical Review Letters **121** (2018) `10.1103/physrevlett.121.035301`.

[40] A. Riera-Campeny, M. Moreno-Cardoner, and A. Sanpera, “Time crystallinity in open quantum systems”, Quantum **4**, 270 (2020) `10.22331/q-2020-05-25-270`.

[41] G. Piccitto, B. Žunkovič, and A. Silva, "Dynamical phase diagram of a quantum ising chain with long-range interactions", Physical Review B **100** (2019) `10.1103/physrevb.100.180402`.

[42] G. Piccitto and A. Silva, "Crossover from fast to slow dynamics in a long range interacting ising chain", Journal of Statistical Mechanics: Theory and Experiment **2019**, 094017 (2019) `10.1088/1742-5468/ab3a27`.

[43] L. Foini, L. F. Cugliandolo, and A. Gambassi, "Dynamic correlations, fluctuation-dissipation relations, and effective temperatures after a quantum quench of the transverse field ising chain", Journal of Statistical Mechanics: Theory and Experiment **2012**, P09011 (2012) `10.1088/1742-5468/2012/09/p09011`.

[44] W. H. Zurek, "Cosmological experiments in superfluid helium?", Nature **317**, 505 (1985).

[45] W. H. Zurek, "Cosmological experiments in condensed matter systems", Physics Reports **276**, 177 (1996).

[46] T. Kibble, "Phase-transition dynamics in the lab and the universe", Physics Today **60**, 47 (2007).

[47] T. W. Kibble, "Topology of cosmic domains and strings", Journal of Physics A: Mathematical and General **9**, 1387 (1976).

[48] A. Polkovnikov, "Universal adiabatic dynamics in the vicinity of a quantum critical point", Phys. Rev. B **72**, 161201 (2005) `10.1103/PhysRevB.72.161201`.

[49] J. Dziarmaga, "Dynamics of a quantum phase transition: exact solution of the quantum ising model", Phys. Rev. Lett. **95**, 245701 (2005) `10.1103/PhysRevLett.95.245701`.

[50] W. H. Zurek, U. Dorner, and P. Zoller, "Dynamics of a quantum phase transition", Phys. Rev. Lett. **95**, 105701 (2005) `10.1103/PhysRevLett.95.105701`.

[51] C. Neill, P. Roushan, M. Fang, Y. Chen, M. Kolodrubetz, Z. Chen, A. Megrant, R. Barends, B. Campbell, B. Chiaro, and et al., "Ergodic dynamics and thermalization in an isolated quantum system", Nature Physics **12**, 1037–1041 (2016) `10.1038/nphys3830`.

[52] J. Eisert, M. Friesdorf, and C. Gogolin, "Quantum many-body systems out of equilibrium", Nature Physics **11**, 124–130 (2015) `10.1038/nphys3215`.

[53] T. Kinoshita, T. Wenger, and D. Weiss, "A quantum newton's cradle", Nature **440**, 900 (2006) `10.1038/nature04693`.

[54] E. T. Jaynes, "Information theory and statistical mechanics", Phys. Rev. **106**, 620 (1957) `10.1103/PhysRev.106.620`.

[55] E. T. Jaynes, "Information theory and statistical mechanics. ii", Phys. Rev. **108**, 171 (1957) `10.1103/PhysRev.108.171`.

[56] J.-S. Caux and R. M. Konik, "Constructing the generalized gibbs ensemble after a quantum quench", Physical Review Letters **109** (2012) `10.1103/physrevlett.109.175301`.

[57] M. Cramer, C. M. Dawson, J. Eisert, and T. J. Osborne, "Exact relaxation in a class of nonequilibrium quantum lattice systems", Physical Review Letters **100** (2008) `10.1103/physrevlett.100.030602`.

[58] T. Langen, S. Erne, R. Geiger, B. Rauer, T. Schweigler, M. Kuhnert, W. Rohringer, I. E. Mazets, T. Gasenzer, and J. Schmiedmayer, "Experimental observation of a generalized gibbs ensemble", Science **348**, 207–211 (2015) `10.1126/science.1257026`.

[59] D. Fioretto and G. Mussardo, "Quantum quenches in integrable field theories", New Journal of Physics **12**, 055015 (2010) `10.1088/1367-2630/12/5/055015`.

[60] P. Calabrese, F. H. L. Essler, and M. Fagotti, "Quantum quench in the transverse field ising chain: i. time evolution of order parameter correlators", Journal of Statistical Mechanics: Theory and Experiment **2012**, P07016 (2012) `10.1088/1742-5468/2012/07/p07016`.

[61] P. Calabrese, F. H. L. Essler, and M. Fagotti, "Quantum quenches in the transverse field ising chain: ii. stationary state properties", Journal of Statistical Mechanics: Theory and Experiment **2012**, P07022 (2012) `10.1088/1742-5468/2012/07/p07022`.

[62] P. Calabrese and J. Cardy, "Quantum quenches in extended systems", Journal of Statistical Mechanics: Theory and Experiment **2007**, P06008–P06008 (2007) `10.1088/1742-5468/2007/06/p06008`.

[63] F. H. L. Essler and M. Fagotti, "Quench dynamics and relaxation in isolated integrable quantum spin chains", J. Stat. Mech. **2016**, 064002 (2016).

[64] M. Rigol, V. Dunjko, V. Yurovsky, and M. Olshanii, "Relaxation in a completely integrable many-body quantum system: anab initiostudy of the dynamics of the highly excited states of 1d lattice hard-core bosons", Physical Review Letters **98** (2007) `10.1103/physrevlett.98.050405`.

[65] L. D'Alessio, Y. Kafri, A. Polkovnikov, and M. Rigol, "From quantum chaos and eigenstate thermalization to statistical mechanics and thermodynamics", Advances in Physics **65**, 239–362 (2016) `10.1080/00018732.2016.1198134`.

[66] M. C. Bañuls, J. I. Cirac, and M. B. Hastings, "Strong and weak thermalization of infinite nonintegrable quantum systems", Physical Review Letters **106** (2011) `10.1103/physrevlett.106.050405`.

[67] O. Bohigas, M. J. Giannoni, and C. Schmit, "Characterization of chaotic quantum spectra and universality of level fluctuation laws", Physical Review Letters **52**, 1 (1984).

[68] T. Zimmermann, H. Koppel, E. Haler, H.-D. Meyer, and L. S. Cederbaum, "Energy level statistics of coupled oscilaltors", Phisica Scripta **35**, 125 (1987).

[69] M. Razavy, “Level spacing associated with a classically degenerate motion”, Physics Letters A **113**, 297 (1985).

[70] S. M. Abuelenin, “On the spectral unfolding of chaotic and mixed systems”, Physica A: Statistical Mechanics and its Applications **492**, 564–570 (2018) `10.1016/j.physa.2017.08.158`.

[71] N. Novkovski and G. Ivanovski, “On the theory of energy level distribution for regular spectra”, Physics Letters A **131**, 178 (1988).

[72] T. H. Seligman, J. Verbaarschot, and M. R. Zirnbauer, “Quantum spectra and transition from regular to chaotic classical motion”, Physical Review Letters **53**, 215 (1984).

[73] V. A. Podolskiy and E. E. Narimanov, “Level spacing distribution in systems with partially chaotic classical dynamics”, Physics Letters A **362**, 412–416 (2007) `10.1016/j.physleta.2006.10.065`.

[74] E. B. Rozenbaum, S. Ganeshan, and V. Galitski, “Universal level statistics of the out-of-time-ordered operator”, Physical Review B **100** (2019) `10.1103/physrevb.100.035112`.

[75] G. Akemann, M. Kieburg, A. Mielke, and T. Prosen, “Universal signature from integrability to chaos in dissipative open quantum systems”, Physical Review Letters **123** (2019) `10.1103/physrevlett.123.254101`.

[76] M. Kollar, F. A. Wolf, and M. Eckstein, “Generalized gibbs ensemble prediction of prethermalization plateaus and their relation to nonthermal steady states in integrable systems”, Physical Review B **84** (2011) `10.1103/physrevb.84.054304`.

[77] M. Stark and M. Kollar, *Kinetic description of thermalization dynamics in weakly interacting quantum systems*, 2013.

[78] M. Heyl, A. Polkovnikov, and S. Kehrein, “Dynamical quantum phase transitions in the transverse-field ising model”, Physical Review Letters **110** (2013) `10.1103/physrevlett.110.135704`.

[79] M. Heyl, “Dynamical quantum phase transitions: a brief survey”, EPL (Europhysics Letters) **125**, 26001 (2019) `10.1209/0295-5075/125/26001`.

[80] I. Homrighausen, N. O. Abeling, V. Zauner-Stauber, and J. C. Halimeh, “Anomalous dynamical phase in quantum spin chains with long-range interactions”, Phys. Rev. B **96**, 104436 (2017).

[81] J. Lang, B. Frank, and J. C. Halimeh, “Concurrence of dynamical phase transitions at finite temperature in the fully connected transverse-field ising model”, Physical Review B **97** (2018) `10.1103/physrevb.97.174401`.

[82] G. Piccitto and A. Silva, “Dynamical phase transition in the transverse field ising chain characterized by the transverse magnetization spectral function”, Physical Review B **100** (2019) `10.1103/physrevb.100.134311`.

[83] P. Jurcevic, H. Shen, P. Hauke, C. Maier, T. Brydges, C. Hempel, B. P. Lanyon, M. Heyl, R. Blatt, and C. F. Roos, "Direct observation of dynamical quantum phase transitions in an interaction many-body system", Phys. Rev. Lett. **119**, 080501 (2017).

[84] N. Fläschner, D. Vogel, M. Tarnowski, B. S. Rem, D.-S. Lühmann, M. Heyl, J. C. Budich, L. Mathey, K. Sengstock, and C. Weitenberg, "Observation of dynamical vortices after quenches in a system with topology", Nature Physics **14**, 265–268 (2017) `10.1038/s41567-017-0013-8`.

[85] D. Dylewsky, J. K. Freericks, M. L. Wall, A. M. Rey, and M. Foss-Feig, "Nonperturbative calculation of phonon effects on spin squeezing", Physical Review A **93** (2016) `10.1103/physreva.93.013415`.

[86] J. Zhang, G. Pagano, P. W. Hess, A. Kyprianidis, P. Becker, H. Kaplan, A. V. Gorshkov, Z.-X. Gong, and C. Monroe, "Observation of a many-body dynamical phase transition with a 53-qubit quantum simulator", Nature **551**, 601 (2017).

[87] H. Bernien, S. Schwartz, A. Keesling, H. Levine, A. Omran, H. Pichler, S. Choi, A. S. Zibrov, M. Endres, M. Greiner, V. Vuletić, and M. D. Lukin, "Probing many-body dynamics on a 51-atom quantum simulator", Nature **551**, 579–584 (2017) `10.1038/nature24622`.

[88] A. J. Daley, "Quantum trajectories and open many-body quantum systems", Advances in Physics **63**, 77–149 (2014) `10.1080/00018732.2014.933502`.

[89] F. Wilczek, "Quantum time crystals", Physical Review Letters **109** (2012) `10.1103/physrevlett.109.160401`.

[90] V. Khemani, R. Moessner, and S. L. Sondhi, *A brief history of time crystals*, 2019.

[91] K. Sacha and J. Zakrzewski, "Time crystals: a review", Reports on Progress in Physics **81**, 016401 (2017) `10.1088/1361-6633/aa8b38`.

[92] A Campa, T. Dauxois, D. Fanelli, and S. Ruffo, *Physics of long-range interacting systems* (Oxford University Press, 2014).

[93] M Kac, G. Uhlenbeck, and P. Hemmer, "On the van der waals theory of the vapor-liquid equilibrium. i. discussion of a one-dimensional model", Journal of Mathematical Physics **4**, 216 (1963).

[94] M. Kastner, "N-scaling of timescales in long-range n-body quantum systems", J. Stat. Mech. **0104003** (2017).

[95] P. Hauke and L. Tagliacozzo, "Spread of correlations in long-range interaction quantum systems", Phys. Rev. Lett **111**, 207202 (2013).

[96] L. Cevolani, G. Carleo, and L. Sanchez-Palencia, "Protected quasi-locality in quantum systems with long-range interactions", Phys. Rev. A **92** (2015).

[97] M. Foss-Feig, Z.-X. Gong, C. W. Clark, and A. V. Gorshkov, "Nearly-linear light cones in long-range interacting quantum systems", Phys. Rev. Lett. **114**, 157201 (2015).

[98] P. Richerme, Z.-X. Gong, A. Lee, C. Senko, J. Smith, M. Foss-Feig, S. Michalakis, A. V. Gorshkov, and C. Monroe, “Non-local propagation of correlations in long-range interaction quantum systems”, Nature **551**, 198 (2014).

[99] M. F. Maghrebi, Z.-X. Gong, M. Foss-Feig, and A. V. Gorshkov, “Causality and quantum criticality in long-range lattice models”, Phys. Rev. B **93**, 125128 (2016).

[100] L. Cevolani, G. Carleo, and L. Sanchex-Palencia, “Spreading of correlations in exactly-solvable quantum models with long-range interactions in arbitrary dimensions”, New J. Phys. **18** (2016).

[101] J. Eisert, M. van den Worm, S. Manmana, and M. Kastner, “Breakdown of quasilocality in long-range quantum lattice models”, Physical review letters **111**, 260401 (2013) `10.1103/PhysRevLett.111.260401`.

[102] T. Matsuta, T. Koma, and S. Nakamura, “Improving the lieb–robinson bound for long-range interactions”, Annales Henri Poincaré **18**, 519–528 (2016) `10.1007/s00023-016-0526-1`.

[103] A. Lerose and S. Pappalardi, “Origin of the slow growth of entanglement entropy in long-range interacting spin systems”, Physical Review Research **2** (2020) `10.1103/physrevresearch.2.012041`.

[104] W Dür, L Hartmann, M. Lewenstein, and H.-J. Briegel, “Entanglement in spin chains and lattices with long-range ising-type interactions”, Physical review letters **94**, 097203 (2005) `10.1103/PhysRevLett.94.097203`.

[105] M. E. Fisher, S.-k. Ma, and B. Nickel, “Critical exponents for long-range interactions”, Physical Review Letters **29**, 917 (1972).

[106] N. Defenu, A. Codello, S. Ruffo, and A. Trombettoni, “Criticality of spin systems with weak long-range interactions”, Journal of Physics A: Mathematical and Theoretical **53**, 143001 (2020) `10.1088/1751-8121/ab6a6c`.

[107] A. Lerose and S. Pappalardi, *Bridging entanglement dynamics and chaos in semiclassical systems*, 2020.

[108] B. Sciolla and G. Biroli, “Quantum quenches, dynamical transitions, and off-equilibrium quantum criticality”, Physical Review B **88** (2013) `10.1103/physrevb.88.201110`.

[109] N. Shammah, S. Ahmed, N. Lambert, S. De Liberato, and F. Nori, “Open quantum systems with local and collective incoherent processes: efficient numerical simulations using permutational invariance”, Physical Review A **98** (2018) `10.1103/physreva.98.063815`.

[110] I. Homrighausen and S. Kehrein, *Out of equilibrium mean field dynamics in the transverse field ising model*, 2019.

[111] P. Ehrenfest, “Bemerkung über die angenaherte gultigkeit der klassischen mechanik innerhalb der quantenmechanik”, Zeitschrift fur Physika **45**, 455 (1927).

[112] P. G. Silvestrov and C. W. J. Beenakker, “Ehrenfest times for classically chaotic systems”, Physical Review E **65** (2002) `10.1103/physreve.65.035208`.

[113] V. Bapst and G. Semerjian, “On quantum mean-field models and their quantum annealing”, Journal of Statistical Mechanics: Theory and Experiment **2012**, P06007 (2012) `10.1088/1742-5468/2012/06/p06007`.

[114] H. J. Lipkin, N Meshkov, and A. Glick, “Validity of many-body approximation methods for a solvable model:(i). exact solutions and perturbation theory”, Nuclear Physics **62**, 188 (1965).

[115] B. Zunkovic, A. Silva, and M. Fabrizio, “Dynamical phase transitions and loschmidt echo in the infinite-range xy model”, Philos. Trans. R. Soc. A **374**, 20150160 (2016).

[116] P. Ribeiro, J. Vidal, and R. Mosseri, “Exact spectrum of the lipkin-mshkov-glick model in the thermodynamic limit and finite-size corrections”, Phys. Rev. E **78**, 021106 (2008).

[117] J. C. Louw, J. N. Kriel, and M. Kastner, “Thermalization of a lipkin-meshkov-glick model coupled to a bosonic bath”, Physical Review A **100** (2019) `10.1103/physreva.100.022115`.

[118] S. Pappalardi, A. Russomanno, B. Žunkovič, F. Iemini, A. Silva, and R. Fazio, “Scrambling and entanglement spreading in long-range spin chains”, Physical Review B **98** (2018) `10.1103/physrevb.98.134303`.

[119] R. H. Dicke, “Coherence in spontaneous radiation processes”, Physical Review **93** (1954).

[120] K. Hepp and E. H. Lieb, “Equilibrium statistical mechanics of matter interacting with the quantized radiation field”, Physical Review A **8**, 2517 (1973).

[121] Y. K. Wang and F. Hioe, “Phase transition in the dicke model of superradiance”, Physical Review A **7**, 831 (1973).

[122] J. Keeling, M. J. Bhaseen, and B. D. Simons, “Collective dynamics of bose-einstein condensates in optical cavities”, Physical Review Letters **105** (2010) `10.1103/physrevlett.105.043001`.

[123] A. V. Andreev, V. I. Emel’yanov, and Y. A. Il’inskiĭ, “Collective spontaneous emission (dicke superradiance)”, Soviet Physics Uspekhi **23**, 493 (1980).

[124] K. Baumann, C. Guerlin, F. Brennecke, and T. Esslinger, “Dicke quantum phase transition with a superfluid gas in an optical cavity”, Nature **464**, 1301–1306 (2010) `10.1038/nature09009`.

[125] S Schmidt, G Blatter, and J Keeling, “From the jaynes–cummings–hubbard to the dicke model”, Journal of Physics B: Atomic, Molecular and Optical Physics **46**, 224020 (2013) `10.1088/0953-4075/46/22/224020`.

[126] N. Tonchev, J. Brankov, and V. Zagrebnov, “Overview of the superradiant phase transition: the dicke model”, JOURNAL OF OPTOELECTRONICS AND ADVANCED MATERIALS **11**, 1142 (2009).

[127] C. Emary and T. Brandes, “Chaos and the quantum phase transition in the dicke model”, Physical Review E **67** (2003) `10.1103/physreve.67.066203`.

[128] C. Emary and T. Brandes, “Quantum chaos triggered by precursors of a quantum phase transition: the dicke model”, Physical Review Letters **90** (2003) `10.1103/physrevlett.90.044101`.

[129] M. J. Bhaseen, J. Mayoh, B. D. Simons, and J. Keeling, “Dynamics of nonequilibrium dicke models”, Physical Review A **85** (2012) `10.1103/physreva.85.013817`.

[130] P. Kirton, M. M. Roses, J. Keeling, and E. G. Dalla Torre, “Introduction to the dicke model: from equilibrium to nonequilibrium, and vice versa”, Advanced Quantum Technologies **2**, 1800043 (2018) `10.1002/qute.201800043`.

[131] M. Diver, G. Robb, and G.-L. Oppo, “Nonlinear and chaotic dynamics of a bose-einstein condensate in an optical cavity”, Physical Review A **89**, 033602 (2014).

[132] K Rzażewski, K Wódkiewicz, and W Żakowicz, “Phase transitions, two-level atoms, and the a 2 term”, Physical Review Letters **35**, 432 (1975).

[133] P. Nataf and C. Ciuti, “No-go theorem for superradiant quantum phase transitions in cavity qed and counter-example in circuit qed”, Nature communications **1**, 1 (2010).

[134] D. Nagy, G. Szirmai, and P. Domokos, “Critical exponent of a quantum-noise-driven phase transition: the open-system dicke model”, Physical Review A **84** (2011) `10.1103/physreva.84.043637`.

[135] P. Kirton and J. Keeling, “Superradiant and lasing states in driven-dissipative dicke models”, New Journal of Physics **20** (2017) `10.1088/1367-2630/aaa11d`.

[136] M. Gegg, A. Carmele, A. Knorr, and M. Richter, “Superradiant to subradiant phase transition in the open system dicke model: dark state cascades”, New Journal of Physics **20**, 013006 (2018) `10.1088/1367-2630/aa9cdd`.

[137] B. Garraway, “The dicke model in quantum optics: dicke model revisited”, Philosophical transactions. Series A, Mathematical, physical, and engineering sciences **369**, 1137 (2011) `10.1098/rsta.2010.0333`.

[138] L. Beguin, A. Vernier, R. Chicireanu, T. Lahaye, and A. Browaeys, “Direct measurement of the van der waals interaction between two rydberg atoms”, Physical review letters **110**, 263201 (2013) `10.1103/PhysRevLett.110.263201`.

[139] H. Labuhn, D. Barredo, S. Ravets, S. de Léséleuc, T. Macrì, T. Lahaye, and A. Browaeys, “Tunable two-dimensional arrays of single rydberg atoms for realizing quantum ising models”, Nature **534**, 667–670 (2016) `10.1038/nature18274`.

[140] G Pagano, P. W. Hess, H. B. Kaplan, W. L. Tan, P Richerme, P Becker, A Kyprianidis, J Zhang, E Birckelbaw, M. R. Hernandez, Y. Wu, and C. Monroe, "Cryogenic trapped-ion system for large scale quantum simulation", Quantum Science and Technology **4**, 014004 (2018) `10.1088/2058-9565/aae0fe`.

[141] J. W. Britton, B. C. Sawyer, A. C. Keith, C.-C. J. Wang, J. K. Freericks, H. Uys, M. J. Biercuk, and J. J. Bollinger, "Engineered two-dimensional ising interactions in a trapped-ion quantum simulator with hundreds of spins", Nature **484**, 489–492 (2012) `10.1038/nature10981`.

[142] P. Richerme, Z.-X. Gong, A. Lee, C. Senko, J. Smith, M. Foss-Feig, S. Michalakis, A. V. Gorshkov, and C. Monroe, "Non-local propagation of correlations in quantum systems with long-range interactions", Nature **511**, 198–201 (2014) `10.1038/nature13450`.

[143] B. Neyenihuis, J. Smith, A. C. Lee, J. Zhang, P. Richerme, P. W. hess, Z.-X. Gong, A. V. Gorshkov, and C. Monroe, "Observation of prethermalization in long-range interaction spin chains", Science Advances **3** (2017).

[144] G. Bohnet, B. Sawyer, J. W. Britton, M. L. Wall, A. M. Rey, M. Foss-Feig, and J. J. Bollinger, "Quantum spin dynamics and entanglement generation with hundred of trapped ions", Science **352**, 1297 (2016).

[145] J. Zhang, P. W. Hess, A. Kypriandis, P. Becker, A. Lee, J. Smith, G. Pagano, I.-D. Ptorniche, A. C. Potter, A. Vishwanath, N. Y. Yao, and C. Monroe, "Observation of a discrete time crystal", Nature **543**, 217 (2017).

[146] Z.-X. Gong, M. F. Maghrebi, A. Hu, M. Foss-Feig, P. Richerme, C. Monroe, and A. V. Gorshkov, "Kaleidoscope of quantum phases in a long-range interactiong spin-1-chain", Phys. Rev. B **93**, 205225 (2016).

[147] P. W. Hess, P. Becker, H. B. Kaplan, A. Kyprianidis, A. C. Lee, B. Neyenhuis, G. Pagano, P. Richerme, C. Senk, J. Smith, W. L. Tan, J. Zhang, and C. Monroe, "Non-thermalization in trapped atomic ion spin chains", Phil. Trans. R. Soc. A (2017).

[148] R. Islam, C. Senko, W. C. Campbell, S. Korenblit, J. Smith, A. Lee, E. E. Edwards, C.-C. J. Wang, J. K. Freericks, and C. Monroe, *Emergence and frustration of magnetic order with variable long-range interactions in a trapped ion quantum simulator*, (2012) `arXiv:1210.0142v1[quant-ph]`.

[149] S. Olmschenk, K. C. Younge, D. L. Moehring, D. N. Matsukevich, P. Maunz, and C. Monroe, "Manipulation and detection of a trapped yb+ hyperfine qubit", Phys. Rev. A **76**, 052314 (2007).

[150] K.-K. Ni, S. Ospelkaus, M. H. G. de Miranda, A. Pe'er, B. Neyenhuis, J. J. Zirbel, S. Kotochigova, P. S. Julienne, D. S. Jin, and J. Ye, "A high phase-space-density gas of polar molecules", Science **322**, 231–235 (2008) `10.1126/science.1163861`.

[151] S. A. Moses, J. P. Covey, M. T. Miecnikowski, D. S. Jin, and J. Ye, "New frontiers for quantum gases of polar molecules", Nature Physics **13**, 13–20 (2016) `10.1038/nphys3985`.

[152] E. Donley, N. Claussen, S. Thompson, and C. Wieman, "Atom–molecule coherence in a bose-einstein condensate", Nature **417**, 529 (2002) `10.1038/417529a`.

[153] S. Jochim, M. Bartenstein, A. Altmeyer, G. Hendl, S. Riedl, C. Chin, J. H. Denschlag, and R. Grimm, "Bose-einstein condensation of molecules", Science **302**, 2101 (2003).

[154] J. Herbig, T. Kraemer, M. Mark, T. Weber, C. Chin, H.-C. Nägerl, and R. Grimm, "Preparation of a pure molecular quantum gas", Science (New York, N.Y.) **301**, 1510 (2003) `10.1126/science.1088876`.

[155] T. Köhler, K. Góral, and P. S. Julienne, "Production of cold molecules via magnetically tunable feshbach resonances", Reviews of Modern Physics **78**, 1311–1361 (2006) `10.1103/revmodphys.78.1311`.

[156] K. Bergmann, H. Theuer, and B. W. Shore, "Coherent population transfer among quantum states of atoms and molecules", Rev. Mod. Phys. **70**, 1003 (1998) `10.1103/RevModPhys.70.1003`.

[157] C. Sanderson and R. Curtin, "Armadillo: a template-based c++ library for linear algebra", Journal of Open Source Software **1**, 26 (2016).

[158] C. Sanderson and R. Curtin, "A user-friendly hybrid sparse matrix class in c++", Lecture Notes in Computer Science **10931**, 422 (2018).

[159] J. Strzalgo, J. Grabski, A. Stefansi, P. Perilkowski, and T. Kapitaniak, "Dynamics of coin tossing is predictable", Physics Report **469**, 59 (2008).

[160] D. Jaschke, K. Maeda, J. D. Whalen, M. L. Wall, and L. D. Carr, "Critical phenomena and kibble–zurek scaling in the long-range quantum ising chain", New Journal of Physics **19**, 033032 (2017) `10.1088/1367-2630/aa65bc`.

[161] A. Lerose, J. Marino, A. Gambassi, and A. Silva, "Prethermal quantum many-body kapitza phases of periodically driven spin systems", Physical Review B **100** (2019) `10.1103/physrevb.100.104306`.

[162] J. Ma, X. Wang, C. Sun, and F. Nori, "Quantum spin squeezing", Physics Reports **509**, 89–165 (2011) `10.1016/j.physrep.2011.08.003`.

[163] G. Tóth, C. Knapp, O. Gühne, and H. J. Briegel, "Spin squeezing and entanglement", Phys. Rev. A **79**, 042334 (2009) `10.1103/PhysRevA.79.042334`.

[164] O. Gühne and G. Tóth, "Entanglement detection", Physics Reports **474**, 1–75 (2009) `10.1016/j.physrep.2009.02.004`.

[165] J Esteve, C Gross, A Weller, S Giovanazzi, and M. Oberthaler, "Squeezing and entanglement in a bose–einstein condensate", Nature **455**, 1216 (2008).

[166] C. Gross, T. Zibold, E. Nicklas, J. Esteve, and M. K. Oberthaler, "Nonlinear atom interferometer surpasses classical precision limit", Nature **464**, 1165 (2010).

[167] T. Takano, M. Fuyama, R Namiki, and Y. Takahashi, “Spin squeezing of a cold atomic ensemble with the nuclear spin of one-half”, Physical review letters **102**, 033601 (2009) `10.1103/PhysRevLett.102.033601`.

[168] I. Buluta, S. Ashhab, and F. Nori, “Natural and artificial atoms for quantum computation”, Reports on Progress in Physics **74**, 104401 (2011) `10.1088/0034-4885/74/10/104401`.

[169] J. Q. You and F. Nori, “Superconducting circuits and quantum information”, Physics Today **58**, 42–47 (2005) `10.1063/1.2155757`.

[170] I. Georgescu and F. Nori, “Quantum simulators”, Science (New York, N.Y.) **326**, 108 (2009) `10.1126/science.1177838`.

[171] J. J. Bollinger, W. M. Itano, D. J. Wineland, and D. J. Heinzen, “Optimal frequency measurements with maximally correlated states”, Phys. Rev. A **54**, R4649 (1996) `10.1103/PhysRevA.54.R4649`.

[172] K. Qu and G. Agarwal, “Ramsey spectroscopy with squeezed light”, Optics letters **38** (2013) `10.1364/OL.38.002563`.

[173] D. Walls and P Zoller, “Enhanced sensitivity of a gravitational wave detector”, Physics Letters A **85**, 118 (1981).

[174] G. Grynberg, A. Aspect, and C. Fabre, *Introduction to quantum optics* (Cambridge University Press, 2010).

[175] P. Meystre and M. Sargent III, *Elements of quantum optics* (Springer, 2007).

[176] M. Hayn, C. Emary, and T. Brandes, “Superradiant phase transition in a model of three-level lambda-systems interacting with two bosonic modes”, Physical Review A **86** (2012) `10.1103/physreva.86.063822`.

[177] M. Hayn and T. Brandes, “Thermodynamics and superradiant phase transitions in a three-level dicke model”, Physical Review E **95** (2017) `10.1103/physreve.95.012153`.

[178] J. Léonard, A. Morales, P. Zupancic, T. Esslinger, and T. Donner, “Supersolid formation in a quantum gas breaking a continuous translational symmetry”, Nature **543**, 87–90 (2017) `10.1038/nature21067`.

[179] M. Hayn, C. Emary, and T. Brandes, “Phase transitions and dark-state physics in two-color superradiance”, Physical Review A **84** (2011) `10.1103/physreva.84.053856`.

[180] A. Lerose, B. Zunkovic, A. Silva, and A. Gambassi, “Chaotic dynamical ferromagnetic phase induced by non equilibrium quantum fluctuations”, Phys. Rev. Lett. **120**, 130603 (2017).

Post Scriptum

C'è qualcosa che vuole essere scritto, qualcosa che deve essere scritto, ma non è questo il modo. La Signora Giulia strappò l'ennesimo foglio con l'ennesimo tentativo fallito di trovare una conclusione degna.

Sette piani. A fidarsi di Buzzati non un presagio di buona ventura. La Signora Giulia fissò l'ingresso dell'ex sanatorio e si lasciò pervadere dalla malinconia.

Leggeva e rileggeva l'incipit, l'unica cosa che forse davvero funzionava, abbastanza ironico, leggero, lineare. Ma come andare avanti? Ogni tentativo diventava un ammasso di parole scontate e retoriche, di una banalità degna di un romanzetto da quattro soldi. Quindi, secondo la critica, esattamente come tutto il resto della sua produzione, pff... stereotipi di genere. La verità è che ogni conclusione sarebbe stata riduttiva ed esclusiva, non è possibile tirare fuori un racconto che soddisfi le esigenze di tutti. Eppure la Signora Giulia non poteva accettare di darsi per vinta: c'era bisogno di una conclusione. Fosse stata una favola sarebbero vissuti felici e contenti, ma questa non era una favola, era l'Accademia, quindi probabilmente sarebbero vissuti stressati e alienati fino al raggiungimento di un rtd-qualcosa intorno ai quarant'anni, proprio quando tutto sembrava perduto. Una storia agghiacciante, quasi peggiore dei documentari naturalistici della BBC.
La soluzione doveva stare altrove, non nel futuro lavorativo. Fosse stata un po' più arguta, probabilmente lo avrebbe potuto intuire dalla divergenza del rapporto ore passate al bar-ore passate in ufficio. Ma certo! La soluzione stava nella dimensione umana di quel posto che l'aveva ospitata negli ultimi quattro brevemente infiniti anni della sua vita. In quel posto di passaggio, in quel posto in cui ogni fine era sancita dal suo stesso inizio, ogni nuovo inizio una nuova fine, affezionarsi, crescere, continuare e poi salutarsi. Non è un addio, ci rivedremo sicuramente!, un palliativo per brindare all'effimerità.
Ecco, era proprio questo il punto. La Signora Giulia aveva ancora un dubbio che la attanagliava, ovvero se continuare a torturare le persone con questo vacuo magniloquio da biscotto cinese della fortuna, o magari provare a essere più caritatevole limitandosi a qualcosa di più personale della faccenda che coinvolgesse soltanto i "congiunti". Ripercorse con la mente quei corridoi, dall'ala est all'ala ovest. Ancora nessuna stampante funzionante. Ma andando da una scala all'altra, su per ogni piano, si accorse dell'incredibile numero di porte e persone affacciate sul corridoio e sulla sua v... (pericolo retorica!) eranda. Sulla sua veranda, già. Forse troppe per poter essere riassunte in un unico racconto. Inizialmente la Signora Giulia si lasciò tentare dall'eventualità di trascurare tutte quelle persone ormai fuori dalla sua vita,

per demeriti, meriti, o eventualità. Ma in uno slancio di inusuale saggezza realizzò che sarebbe stato scorretto non riconoscere loro la partecipazione, consapevole o meno, alla creazione del personaggio della Signora Giulia. Stette lì a pensare, dunddedun... Come procedere, anche perché il tutto sarebbe dovuto essere pronto al più tardi il giorno della consegna. Ah, se solo ci fosse stato [**Giorgino**] ad aiutarla, lui sì che avrebbe saputo cosa fare. Si versò un bicchiere di vino e rimase ad ascoltare il fischio del vento, di lì a poco sarebbe arrivato un temporale.

Effettivamente questo avrebbe potuto accorciare di molto il processo di menzione, un bicchiere di vino sotto la pioggia è una situazione tale da abbracciare un ampissimo spettro di persone che arrivate a questo punto avrebbero potuto dire, soffocando un risolino imbarazzato: “parla di me!”. Lasciando il meteo variabile e generalizzando l’alcolico è presto fatto. Un bicchiere sincero e alpino, inusuale e filosofico, pettegolo e leggero, femminile con Filippo, analcolico e ambiguo, minorenne (18 a dicembre!) e presente, “tinto” e impegnativo, deludente e amaro, intimo e giocoso, salato e confortante, duraturo e stabile, paziente e litigarello, adulto e infantile, sportivo e collegiale, esagerato e galvanizzante. E molti di questi bicchieri andrebbero sommati a diventare bottiglie da riempirci una cantina intera a cui attingere dopo un gol di testa, dopo un pranzo in silenzio, dopo una serata al mare, dopo un pianto ininterrotto quando l’unica cosa che ti serve è un abbraccio, durante i post-prandiali su un letto a svuotarsi delle ansie o durante le nottate che, confuse sul loro ruolo, invece di portare consiglio, le portavano le ansie. E, continuando con l’analogia, molte di quelle bottiglie si potevano riversare a loro volta in botti più grandi, così pesanti da non poter essere spostate facilmente, ci sono sempre, qui e ora. Una prospettiva piuttosto rassicurante.

La Signora Giulia si fermò un attimo a rileggere le ultime frasi. La conclusione della conclusione era decisamente più difficile della conclusione in sé, un climax ascendente di cliché (probabilmente anche questo continuo riferimento alla sua banalità stava diventando un cliché, molto meta, punto interessante da poter approfondire). Si vergognò per il sentimentalismo e decise che l’unico modo possibile per salvare la faccia sarebbe stato risparmiare le parole per un qualche scopo più nobile (ringraziare le bariste, trovarsi un lavoro, inneggiare alla morte del capitale...). Un ultimo sguardo alle conclusioni (e alle conclusioni delle conclusioni, seppure ancora in fieri). Non che fosse molto soddisfatta del suo operato, il risultato finale si allontanava parecchio dal testo palindromo in versi che aveva sperato di produrre, ma a volte è necessario saper riconoscere i propri limiti, poteva bastare così.

Ringraziando cortesemente tutti, fece un inchino e si dissolse.